



University of Kentucky  
UKnowledge

---

Theses and Dissertations--Mechanical  
Engineering

Mechanical Engineering

---


2018

## Verification and Validation Studies for the KATS Aerothermodynamics and Material Response Solver

Olivia Schroeder

University of Kentucky, omsc222@uky.edu

Author ORCID Identifier:

 <https://orcid.org/0000-0003-0487-2992>

Digital Object Identifier: <https://doi.org/10.13023/etd.2018.355>

[Right click to open a feedback form in a new tab to let us know how this document benefits you.](#)

---

### Recommended Citation

Schroeder, Olivia, "Verification and Validation Studies for the KATS Aerothermodynamics and Material Response Solver" (2018). *Theses and Dissertations--Mechanical Engineering*. 122.

[https://uknowledge.uky.edu/me\\_etds/122](https://uknowledge.uky.edu/me_etds/122)

This Master's Thesis is brought to you for free and open access by the Mechanical Engineering at UKnowledge. It has been accepted for inclusion in Theses and Dissertations--Mechanical Engineering by an authorized administrator of UKnowledge. For more information, please contact [UKnowledge@lsv.uky.edu](mailto:UKnowledge@lsv.uky.edu).

## **STUDENT AGREEMENT:**

I represent that my thesis or dissertation and abstract are my original work. Proper attribution has been given to all outside sources. I understand that I am solely responsible for obtaining any needed copyright permissions. I have obtained needed written permission statement(s) from the owner(s) of each third-party copyrighted matter to be included in my work, allowing electronic distribution (if such use is not permitted by the fair use doctrine) which will be submitted to UKnowledge as Additional File.

I hereby grant to The University of Kentucky and its agents the irrevocable, non-exclusive, and royalty-free license to archive and make accessible my work in whole or in part in all forms of media, now or hereafter known. I agree that the document mentioned above may be made available immediately for worldwide access unless an embargo applies.

I retain all other ownership rights to the copyright of my work. I also retain the right to use in future works (such as articles or books) all or part of my work. I understand that I am free to register the copyright to my work.

## **REVIEW, APPROVAL AND ACCEPTANCE**

The document mentioned above has been reviewed and accepted by the student's advisor, on behalf of the advisory committee, and by the Director of Graduate Studies (DGS), on behalf of the program; we verify that this is the final, approved version of the student's thesis including all changes required by the advisory committee. The undersigned agree to abide by the statements above.

Olivia Schroeder, Student

Dr. Alexandre Martin, Major Professor

Dr. Alexandre Martin, Director of Graduate Studies

Verification and Validation Studies for the KATS Aerothermodynamics and  
Material Response Solver

---

THESIS

---

A thesis submitted in partial  
fulfillment of the requirements for  
the degree of Master of Science in  
Mechanical Engineering in the  
College of Engineering at the  
University of Kentucky

By  
Olivia Schroeder  
Lexington, Kentucky

Director: Dr. Alexandre Martin, Professor of Mechanical Engineering

Lexington, Kentucky 2018

Copyright© Olivia Schroeder 2018

## ABSTRACT OF THESIS

### Verification and Validation Studies for the KATS Aerothermodynamics and Material Response Solver

Modeling the atmospheric entry of spacecraft is challenging because of the large number of physical phenomena that occur during the process. In order to study thermal protection systems, engineers rely on high fidelity solvers to provide accurate predictions of both the thermochemical environment surrounding the heat shield, and its material response. Therefore, it is necessary to guarantee that the numerical models are correctly implemented and thoroughly validated. In recent years, a high-fidelity modeling tool has been developed at the University of Kentucky for the purpose of studying atmospheric entry. The objective of this work is to verify and validate this code. The verification consists of the development of an automated regression testing utility. It is intended to both aid code developers in the debugging process, as well as verify the correct implementation of the numerical models as these are developed. The validation process will be performed through comparison to relevant ablation experiments, namely arc-jet tests. Two modules of the code are used: fluid dynamics, and material response. First the fluid dynamics module is verified against both computational and experimental data on two distinct arc-jet tests. The material response module is then validated against arc-jet test data using PICA.

KEYWORDS: atmospheric entry, thermal protection systems, material response, ablation, arc-jet

Author's signature: Olivia Schroeder

Date: August 28, 2018

Verification and Validation Studies for the KATS Aerothermodynamics and  
Material Response Solver

By  
Olivia Schroeder

Director of Thesis: Alexandre Martin

Director of Graduate Studies: Alexandre Martin

Date: August 28, 2018

Dedicated to Ruth Schroeder and Terry Meek.

## ACKNOWLEDGMENTS

First and foremost, I'd like to thank my advisor, Dr. Alexandre Martin. When I first attended his Fluid Mechanics class (ME330), coincidentally my favorite class ever, I did not know what I wanted to do or how I could engage in an engineering community I felt was simultaneously interesting and meaningful. When he first introduced the class to his research field, atmospheric entry, I immediately wanted to do be a part of his research group. Over the time I have been his student, I have never stopped learning and growing as a researcher, a colleague, and a student. I have been given opportunities I never would have imagined I could partake in, and I have succeeded in achieving my goals. Dr. Martin and his research group have also inspired me to further my academic studies and learn more about the field of entry, descent and landing. I would also like to acknowledge the wonderful faculty in the Department of Mechanical Engineering. I am grateful to have had the opportunity to take such interesting classes with dynamic professors that are always willing to spend their time teaching confused students. Dr. Sean Bailey in particular, suffered extensively from long office hour meetings. Dr. José Graña-Otero taught one of my favorite classes in graduate school and his passion and fundamental knowledge greatly inspire me. I would also like to acknowledge my committee members, Dr. Christoph Brehm and Dr. Kozo Saito, who gladly were willing to provide helpful insight and guidance during stressful times. Finally, I would like to thank the staff members in our department. Will Aaron, Brenda Heeter and Callie Viens are life savers to us all and they keep this lovely department running smoothly. I would like to also acknowledge the code development team I had the privilege to intern with at NASA Ames. Working with Eric Stern, Joseph Schulz, Grant Palmer and Suman Muppidi, under David Hash's intern program, was a once in a lifetime opportunity. I not only

learned a lot but also became even more inspired by our field and understanding how the research we conduct in academia is used in real-world problems. Even with the most the help of the most inspiring group of people, none of the time I spent learning and contributing to this field would have been possible without the generous undergraduate and graduate grants I was awarded by NASA Kentucky under the EPSCoR program. This programs is truly life-changing as it provides the necessary means to strive in our field without having to chose between higher education or living debt-free. From the Gas Surface Interactions Lab, I believe every member has in some way or another contributed to my knowledge and understanding of our field. However, being able to also become good friends with one's colleagues is a privilege. It has been a true pleasure to work and interact with Chris Barrow, Justin Cooper, Adnan Darwish, Huaibao Zhang, Raghava Davuluri, Umran Duzel, Luke Fortner, Rui Fu, Nick Khouri, Zhiyong Li, Ali Omidy, James Rogers, Christen Setters, Devin Sparks, TingTing Tang, Rachel Walker, Haoyue Weng, and Evan Whitmer. I will cherish the memories of our BBQ's, movies, and World Cup games for a long time. I'd also like to thank my undergraduate study group for their help. Studying with Ausencio Fuentes, Nikki Marcum, Chris Meek, and Robert Retallick helped me make the most of my classes and understand the concepts, this has been invaluable to my work and development as an engineer. I would like to most gratefully thank my dearest families: Ken, Linda, Milu and Alberto, and my most recently added family, Cheryl, Dale, James, and Donna. They have been the best at cheering me on and supporting me through all sorts of times. I believe that much of the joy I bring to my work comes from what they have given me. Last but not least, I would like to thank Chris Meek, for being the best partner, friend, and engineer I could ever hope to marry.



## TABLE OF CONTENTS

Acknowledgments . . . . .	iii
Table of Contents . . . . .	v
List of Figures . . . . .	viii
List of Tables . . . . .	x
Chapter 1 Introduction . . . . .	1
1.1 Background . . . . .	1
1.2 Motivation . . . . .	4
Chapter 2 Literature Review . . . . .	6
2.1 Historical perspective . . . . .	6
2.2 Ablation phenomena . . . . .	9
2.3 Computational state-of-the-art . . . . .	11
2.4 KATS numerical framework . . . . .	13
2.4.1 Fluid dynamics governing equations . . . . .	14
2.4.2 Governing equations for material response . . . . .	16
Chapter 3 Verification . . . . .	18
3.1 Development of an automated testing toolbox (ATT) . . . . .	18
3.2 Grid-function convergence testing . . . . .	20
3.3 Test suite of analytical solutions . . . . .	21
3.3.1 Transient conduction with fixed temperature boundary condition	21
Problem description . . . . .	21
Test parameters . . . . .	22
Results . . . . .	22
3.3.2 Transient conduction with a fixed heat flux boundary condition	23
Problem description . . . . .	23
Test parameters . . . . .	24
Results . . . . .	24
3.3.3 Transient conduction with a time-varying heat flux boundary	24
condition . . . . .	24
Problem description . . . . .	24
Test parameters . . . . .	26
Results . . . . .	26
3.3.4 Fixed heat flux boundary condition with temperature depen-	27
dent thermal properties . . . . .	27
Problem description . . . . .	27

	Test parameters . . . . .	28
	Results . . . . .	28
3.3.5	Aeroheating convection boundary condition . . . . .	29
	Problem description . . . . .	29
	Test parameters . . . . .	30
	Results . . . . .	31
3.3.6	Steady-state re-radiation boundary condition . . . . .	31
	Problem description . . . . .	31
	Test parameters . . . . .	32
	Results . . . . .	32
3.3.7	Steady-state porous flow . . . . .	32
	Problem description . . . . .	32
	Test parameters . . . . .	35
	Results . . . . .	35
3.4	Mesh motion verification . . . . .	36
3.4.1	Compressed gas . . . . .	36
3.4.2	Solid mass removal . . . . .	37
3.4.3	Expanding channel . . . . .	38
3.4.4	Constant temperature ablator . . . . .	39
Chapter 4	Flow Field Studies . . . . .	42
4.1	Numerical methods and models . . . . .	43
4.2	TP3 7.5-inch nozzle . . . . .	44
4.2.1	Computational geometry . . . . .	44
4.2.2	Inlet conditions . . . . .	46
4.2.3	Results . . . . .	46
4.3	HYMETS Mach 5 nozzle . . . . .	50
4.3.1	Geometry . . . . .	50
4.3.2	Test conditions . . . . .	51
4.3.3	Results . . . . .	53
Chapter 5	Material Response Validation . . . . .	59
5.1	PICA material model . . . . .	59
5.2	Arc-jet environments . . . . .	59
5.2.1	Boundary conditions . . . . .	60
5.2.2	Blowing reduction . . . . .	61
5.3	Test parameters . . . . .	61
5.3.1	Results . . . . .	63
Chapter 6	Gas Transport in Porous Media . . . . .	68
6.1	Motivation . . . . .	68
6.2	Implementation . . . . .	69
6.2.1	Governing equations . . . . .	69
6.2.2	Time-step stability . . . . .	71

6.2.3	First-Order Upwind Scheme . . . . .	71
6.3	Preliminary results . . . . .	72
Chapter 7	Conclusion . . . . .	76
7.1	Summary . . . . .	76
7.2	Original contributions . . . . .	78
Appendix 1	. . . . .	82
Appendix 2	. . . . .	83
Bibliography	. . . . .	85
Vita	. . . . .	93

## LIST OF FIGURES

1.1 Artistic rendition of the Orion spacecraft re-entering the earth’s atmosphere from Ref. [1]. . . . .	2
2.1 Entry vehicle body shapes from Ref. [2], Photo ID: GPN-2000-001938 . . . . .	6
2.2 Vostok 1’s reentry capsule after landing from Ref. [3], Photo ID: 228667. . . . .	7
2.3 Friendship 7 spacecraft from Ref. [4]. . . . .	8
2.4 Stardust re-entering the earth’s atmosphere from Ref. [5]. . . . .	9
2.5 Carbon Phenolic through the stages of decomposition from Ref. [6]. . . . .	10
2.6 DSMC modeling of flow through carbon fiber matrix from Ref. [7]. . . . .	12
2.7 Thermomechanical stress on a carbon fiber simulated with KATS-thermoelastic solver. . . . .	13
3.1 Functional diagram of automated testing tool. . . . .	19
3.2 Meshes used in grid convergence test. . . . .	20
3.3 Fixed temperature wall boundary condition verification. . . . .	23
3.4 Fixed heat flux boundary condition . . . . .	25
3.5 Exact solution vs. KATS . . . . .	26
3.6 Linearly temperature dependent thermal properties conduction verification problem. . . . .	29
3.7 Convective aeroheating boundary condition verification. . . . .	31
3.8 Steady-state radiation verification. . . . .	33
3.9 Steady porous flow verification . . . . .	35
3.10 Compressed gas problem . . . . .	36
3.11 Computed ideal gas law using KATS gas mass equation . . . . .	37
3.12 Mass flux problem . . . . .	38
3.13 Surface mass flux vs. volumetric loss . . . . .	38
3.14 Expanding channel problem . . . . .	39
3.15 Surface energy flux vs. volumetric loss . . . . .	41
4.1 Computational grid for TP3 7.5 in nozzle and chamber. . . . .	45
4.3 Mach number contour comparison between KATS and DPLR. . . . .	47
4.4 Nozzle centerline species mass fraction comparison between KATS and DPLR. . . . .	48
4.5 Nozzle centerline temperature comparison between KATS and DPLR. . . . .	48
4.6 Post-shock region species mass fraction simulated with KATS. . . . .	49
4.7 Post-shock region temperature comparison between KATS and DPLR. . . . .	50
4.9 PLIF experimental set-up in HYMETs, from Ref. [8]. . . . .	52
4.10 Axial Velocity Profiles from Inman et al. [8] using PLIF . . . . .	52
4.11 Mach number contour simulated with KATS. . . . .	54
4.12 Axial velocity contour simulated with KATS. . . . .	55
4.13 Axial velocity comparison between KATS and PLIF, at $x = 0.57$ cm downstream of the nozzle. . . . .	56

4.14	Axial velocity comparison between KATS and PLIF, at $x = 1.97$ cm downstream of the nozzle. . . . .	56
4.15	Axial velocity comparison between KATS and PLIF, at $x = 2.97$ cm downstream of the nozzle. . . . .	57
4.17	Sample surface properties as predicted with KATS. . . . .	58
5.1	Heat flux and pressure of the seven test cases. . . . .	62
5.2	Sample thermocouple placement. . . . .	63
5.3	Recession in low heat flux and pressure test cases. . . . .	63
5.4	Recession at intermediate heat flux and pressure test cases. . . . .	64
5.5	Recession at high heat flux and pressure test cases. . . . .	64
5.6	Case 7 - Heat Flux = $1102 \text{ W/cm}^2$ , Pressure = $31000 \text{ Pa}$ . . . . .	64
5.7	Surface temperature in low heat flux and pressure test cases. . . . .	65
5.8	Surface temperature at intermediate heat flux and pressure test cases. . . . .	65
5.9	Surface temperature at high heat flux and pressure test cases. . . . .	65
5.10	Case 7 - Heat Flux = $1102 \text{ W/cm}^2$ , Pressure = $31000 \text{ Pa}$ . . . . .	66
6.1	Face estimation values with finite-differencing schemes. . . . .	72
6.2	Gas flow properties comparison with two porous models. . . . .	73
6.3	Thermal behavior comparison with two porous models. . . . .	73
6.4	Pressure and pressure gradient comparison with two porous models. . . . .	74

## LIST OF TABLES

1.1	Means of studying TPS. . . . .	3
3.1	Fixed temperature boundary condition verification problem parameters. .	22
3.2	Applied heat flux boundary condition verification problem parameters. .	24
3.3	Time-varying applied heat flux boundary condition verification problem parameters. . . . .	26
3.4	Material properties for temperature dependent properties verification prob- lem. . . . .	28
3.5	Simulation parameters for temperature-dependent thermal properties con- duction verification problem parameters. . . . .	28
3.6	Aeroheating convection verification problem parameters. . . . .	30
3.7	Surface thermochemistry . . . . .	30
3.8	Steady-state radiation verification problem parameters. . . . .	32
3.9	Steady porous flow problem parameters. . . . .	35
3.10	Expanding channel parameters . . . . .	39
3.11	Expanding channel results. . . . .	40
4.1	Simulation Parameters for TP3 7.5 inch Nozzle . . . . .	46
4.2	Simulation Parameters for Test Case 1 . . . . .	51
4.3	Simulation Parameters for Mach 5 Nozzle Flow . . . . .	53
5.1	Simulation parameters for array of test cases . . . . .	62

# Chapter 1: Introduction

## 1.1 Background

Planetary entry is a highly complex process that ranges over numerous time and length scales encompassing a variety physical phenomena. Entry vehicles traveling at hypersonic speeds are required to decelerate rapidly in order to insure the terminal descent system has enough time to deploy and that the vehicle can subsequently land softly and precisely [9]. The use of blunt forebody geometry induces a strong bow shock wave at the front of the vehicle, see Fig. 1.1. The shock wave increases the temperature in the shock layer setting off a strain of chemical reactions among the gases as well as gas-surface interactions. It also increases the pressure, which in turn increases the drag on the vehicle assisting in the deceleration [10]. During this process the kinetic energy of the gas is transformed into thermal energy and gets transferred to the surface of the vehicle through convection and radiation. In order to attenuate the heat conduction to the vehicle, thermal protection systems (TPS) are used. There are three kinds of thermal protection systems: passive, active, and ablative. Passive systems rely on their low thermal conductivity to limit heat penetration and often use coatings to increase emissivity and, therefore, re-radiated heat. These systems were used during the shuttle era in the form of ceramic tiles, and are currently employed for missile design. They are re-usable but limited by the temperature of re-usability. They are not suitable for high heat flux and heat load because of this. Active thermal protection systems utilize cooling systems which require plumbing and transpiration devices. These are highly complex and seldomly used. Finally, ablative materials are the most commonly used type of thermal protection system for planetary entry missions. These are low density materials - typically porous - that are infused with



Figure 1.1: Artistic rendition of the Orion spacecraft re-entering the earth's atmosphere from Ref. [1].

resins and sacrificed for heat attenuation. Heat rejection is done by pyrolysis of gas from infused resins, ablation (mass removal), and re-radiation[11].

It is not trivial to size the heat shield for an entry vehicle. The design engineer must minimize the amount of mass that is used, while insuring that the recession (mass that is lost at the surface of the heat shield) stays within a specified tolerance, and that the temperature at the bondline (wall of the spacecraft) is below the limit established by the bonding agent, electronics, or payload. Furthermore, all of these parameters are then used for reliability and risk calculation, which requires the uncertainty associated with each failure mode to be extremely low, especially if the mission involves humans. This process of analysis requires a firm understanding and subsequent quantification of the underlying mechanisms that participate in the entry process.

There are three methods which can be used for studying and designing heat shields: flight testing, ground testing, and computer-aided simulations [12]. Flight testing is rare, expensive and not easily instrumented, therefore it is not sufficient for testing TPS materials. For this, high enthalpy facilities are used as a means to test vari-



Table 1.1: Means of studying TPS.

<b>Types</b>	<b>Advantages</b>	<b>Disadvantages</b>
Flight Testing	Highest fidelity Data for validation Reveals new phenomena	Prohibitively expensive Not statistically viable High risk
Ground Testing	Cheaper than flight testing Wide range conditions Easily instrumented Controllable conditions	High cost Not statistically viable Large degree of uncertainty Ground-to-flight traceability
Numerical Modeling	Inexpensive Repeatable Parametrizable Multi-fidelity capability Optimization	Verification and validation Require physical models Involve assumptions

ous materials, under characterized conditions. Although high enthalpy flow facilities provide repeatable testing conditions, these cannot always be extrapolated to flight scenarios. This is known as the ground-to-flight traceability problem. This can be either because of unknown phenomena (e.g. radiative heating in Martian atmospheric environment), or simply because the conditions encountered during entry cannot be reproduced in ground facilities [13]. For example, these facilities cannot match bulk gas enthalpy and gas velocity simultaneously. Here, computational tools can be useful. Numerical simulations are relatively inexpensive and efficient when compared with ground testing. Because these allow for multiple levels of fidelity, they are useful for both design and research applications. The low-fidelity simulations are fast, robust, and useful for optimization and production. Mid-fidelity simulations can incorporate simple models with known assumptions to maintain efficiency while still being applied to relatively complex scenarios, therefore being a more efficient alternative to high-fidelity. Finally, high-fidelity tools are mostly used for research applications as they

can be inefficient for production simulations. They can help improve the understanding of underlying mechanisms involved in the re-entry process that would otherwise be difficult to study or measure experimentally. These can also provide uncertainty quantification for simple models thereby informing designers what relevant physics to incorporate in their simulations. One of the problems with computational tools for modeling reentry is that they require extensive validation through ground and flight testing. This interaction and dependency between methods is proverbially referred to the aerothermal three-legged-stool.

## 1.2 Motivation

As alluded to in the previous section, each method to study TPS carries its advantages and disadvantages. This work will focus on the specific interaction between ground testing and numerical modeling.

From a computational modeling stand-point, there is a need to understand the discrepancies between computational predictions and experimental data. Being able to understand what parameters are most important for making an accurate computational prediction is of great value. Furthermore, as computational tools increase in fidelity and are able to incorporate more complex models, it is useful to be able to understand the relative importance of the latter when predicting measurable parameters such as mass loss and temperature distribution. However, one of the most important aspects in computational fields is validation. Validation is the assurance that the computational tool accurately (or within a known tolerance) replicates reality and that the models implemented contain the correct governing physics for solving the problem at hand. In the field of computational research for entry vehicles, data for validation is scarce and mostly originates from ground testing facilities. Therefore, it is of the utmost importance to validate computational tools against this data. There

are also benefits of these kinds of studies to experimentalists. If a tool is successfully validated, it can also provide insight into unmeasured parameters involved in ground testing; therefore aiding in parametric studies, future facility design, and uncertainty quantification.

Finally, when using numerical tools, it is not only important that the physical models represent reality, but that the governing equations be correctly implemented i.e. there are no “bugs”. This process is termed “verification”; it generally takes a modular approach and frequently relies on simple problems with mathematically known solutions.

The objective of this work is to demonstrate the efforts in verifying and validating the Kentucky Aerothermodynamics and Thermal-response System (KATS) solver, an in-house family of codes developed for the purpose of performing high-fidelity research in hypersonics and material response of TPS for atmospheric entry vehicles.

## Chapter 2: Literature Review

### 2.1 Historical perspective

Charring ablators have been used for re-entry applications dating back to the 1950s [14], particularly in Inter Continental Ballistic Missile (ICBM) design. Up until 1952, missiles were thought to have the best geometry for atmospheric penetration if they were sleek and sharp pointed. It was shown that year, by Julian Allen [15], that blunt-nosed geometries were actually better due to the generation of a strong bow-shock, which alleviated heating at the stagnation point, see Fig. 2.1. This marked a major shift in paradigms for re-entry and allowed for many future manned missions to become possible [16]. Although it was shown analytically that a blunt nosed object better attenuated heating during re-entry, it was still necessary to develop heat-shields that were capable of sustaining this heat and have low enough density to meet the weight requirements. The year 1955 marked the beginning of the space race, when the Soviet Union declared they had launched the first satellite into earth's orbit, Sputnik. Six years later, the Soviet Union positioned the first human in space, Yuri Gagarin. His capsule, the Vostok 3KA, contained a 2.3 m diameter

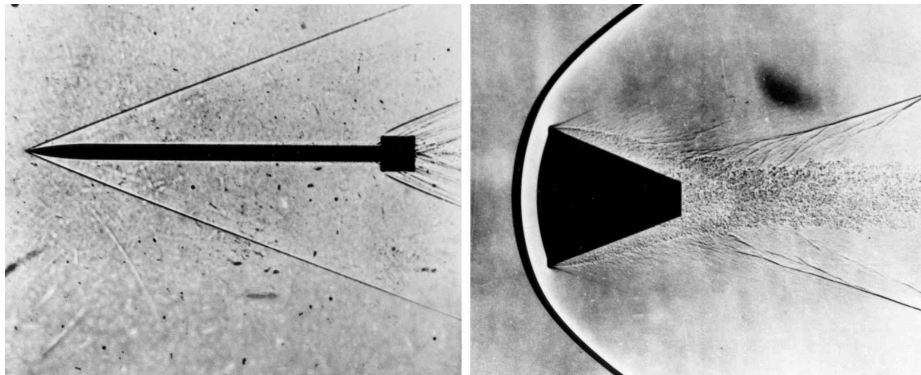


Figure 2.1: Entry vehicle body shapes from Ref. [2], Photo ID: GPN-2000-001938



Figure 2.2: Vostok 1's reentry capsule after landing from Ref. [3], Photo ID: 228667.

spherical re-entry module, Sharik in Fig. 2.2. In 1958, NASA was created by the act signed by then President D. Eisenhower, and the manned space mission developed by the Air Force was transferred to NASA and named Project Mercury. One year after the Soviet Union sent Yuri Gagarin to into orbit, astronaut John Glenn became the first American to orbit Earth, aboard the Friendship 7, Fig. 2.3, demonstrating to the Soviet Union that the United States could compete in the Space Race. The heat shield on the Friendship 7 was made from Fiberglass, bonded with phenolic resin, a pyrolyzing ablator [17]. While Project Mercury demonstrated humanity's capability to achieve spaceflight, a vast amount of atmospheric data and progress in the field of high-performance vehicle design resulted from the hypersonic research airplane, the X-15 [16]. It was during the Gemini program, among many other aspects, that the blunt-body lifting reentry vehicles were developed; verifying the concepts for the Apollo program. During the Apollo program there was a need for a more sophisticated ablative material, since the heat loads were expected to be much higher than ever experienced before. It was during that period that Avco (now Textron) developed Avcoat [18]. This consisted of a honeycomb steel structure, made of 400,000 cells, filled with a mixture of silica micro-balloons using a caulking gun.

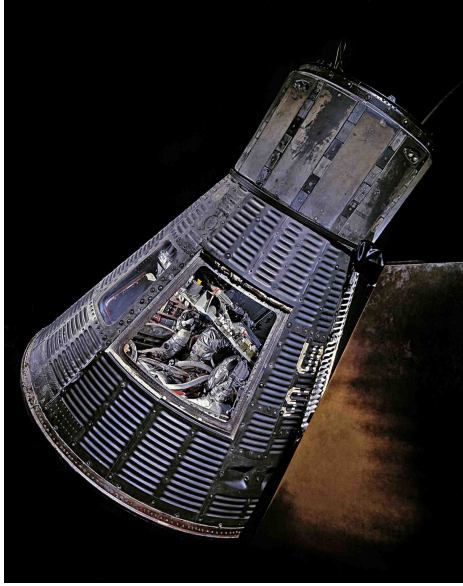


Figure 2.3: Friendship 7 spacecraft from Ref. [4].

Avcoat became a heritage material for future NASA missions, and a modified version is currently being used for NASA's Orion project [19]. It is worth noting that this material does not "recede" but actually melts. Because engineers did not have adequate testing facilities for replicating entry environments nor were there sophisticated computational tools available, it is estimated that the heat shield for the Apollo program was designed 50% over the safety margin [16].

During the shuttle era, NASA ceased much of the research and development on ablative materials in order to pursue re-usable TPS technology. It was not until the 1980s and 1990s with the Pioneer Venus and Galileo missions that NASA began reinvesting time in ablative TPS technology. Unfortunately, much of the knowledge about ablative TPS was lost during that time and designing a heat shield for environments as severe as those endured by the Galileo probe was taxing. The most sophisticated material available for these probes at the time was a dense carbon-phenolic. It was at this time that NASA began investing in the development of low-density ablators for future probe missions. Phenolic Impregnated Carbon Ablator (PICA) was developed in response to this need. PICA has low-density and is composed of a carbon fiber matrix impregnated with a phenolic resin. In 1999, NASA launched Stardust, a spacecraft that performed a close flyby of the Wild-2 comet and collected interstellar dust for sample-return. In 2006, Stardust re-entered the earth's atmosphere traveling at 12.9 km/s, the fastest ever man-made object to enter the earth's atmosphere, and sustaining heat fluxes as

high as  $1200 \text{ W/cm}^2$  [20].

## 2.2 Ablation phenomena

As previously discussed, when spacecraft travel through the atmosphere at hypersonic speeds, high heat loads and heat transfer rates ensue. While some heat is re-radiated from the surface of the TPS, another portion is conducted through the material. This leads to a gradual increase in the temperature of the TPS layer. Pyrolyzing ablators, such as PICA, in their virgin state contain a fibrous carbon preform surrounded by “clouds” of phenolic resin as shown in Fig. ???. During the heating process, the phenolic resin decomposes into pyrolysis gas serving the functions:



Figure 2.4: Stardust re-entering the earth’s atmosphere from Ref. [5].

- Mitigate heating by absorbing energy and undergoing endothermic reactions, thus cooling the char;
- Transpiration cooling;
- Attenuate the heat flux before it reaches the surface by thickening the boundary layer through gas blowing.

Research has been conducted to understand the chemical composition of the phenolic resin and how it decomposes [21], to obtain more accurate decomposition rates and a better understanding of the gas composition inside the material and in the boundary layer. This is important because different gases have different thermal properties which may or may not favor the heating of the surrounding material as well as promote

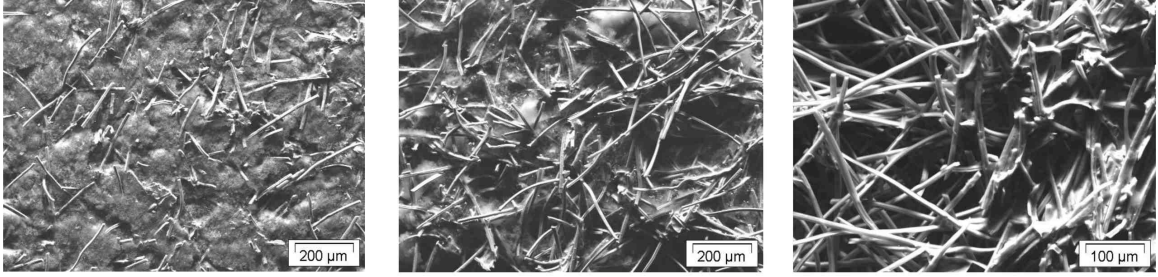


Figure 2.5: Carbon Phenolic through the stages of decomposition from Ref. [6].

its oxidation.

The region where the phenolic resin has decomposed and only low density char remains is termed the char layer. Once oxygen reaches the carbon matrix of the char layer, mass removal processes begin to occur i.e. oxidation, nitration, sublimation, mechanical erosion, and spallation. How long it takes for oxygen to penetrate the carbon matrix [22, 23, 24], and how much of it reaches this zone is also important for the study of volumetric ablation, where mass loss due to oxidation of the carbon fibers occurs in-depth [25]. While these phenomena are relatively well understood, there is a wide range of competing mechanisms occurring at a wide range of time and length scales that are still studied today. The specific mechanisms for mass removal, for instance, is studied because at scales of  $\mathcal{O}(10^{-9})$ , the prominent mechanism for carbon depletion may appear to be pitting [26]. On the other hand, at scales of  $\mathcal{O}(10^{-6})$  it may seem as if the predominant mechanism for mass loss is breaking or shearing of carbon fibers [27]. There is also the phenomena of entire fibers, or groups of fibers being ejected from the matrix, termed spallation [28, 29]. The high level of complexity of the behavior of TPS materials makes it a highly evolving, multidisciplinary field.



### 2.3 Computational state-of-the-art

One of the first computational tools developed for analyzing the behavior of charring ablators was the Charring Material Ablation program (CMA) [30, 31]. It was developed by Aerotherm, and a detailed report explaining the material response of ablative materials was published in 1968, becoming one of the most cited bodies of work in the field since. CMA is a 1-dimensional (1D), finite-difference, code written in Fortran, which solves the energy conservation, solid mass conservation equation, and a steady gas conservation equation. It utilizes phenomenological models for the decomposition of solid material and does not resolve the pyrolysis gas transport equations. The gas is therefore instantaneously transported to the surface to contribute to the surface mass and energy balance. At NASA Ames Research Center, the Fully Implicit Ablation and Thermal response code (FIAT) [32] was developed in 1991. FIAT is also a 1D program which utilizes the same material model as CMA, but takes advantage of a fully implicit numerical scheme for better stability. The development of FIAT allowed for the resolution of more complex problems and was used for sizing TPS for a wide range of missions, including Stardust, Mars Science Laboratory and Orion. Because of its efficiency, it is also commonly used for optimization problems. FIAT is one of the most extensively validated codes to date. However, it is known to be conservative in its estimates. With the increasingly stringent mass constraints for larger payload missions, having more accurate predictions of the material behavior has become a priority for NASA researchers, as conservative models can no longer provide enough accuracy for reliability estimation. Furthermore, as more complex materials are developed such as woven TPS, which can take on complex geometries, highly robust, multi-dimensional tools become essential. This led to the development of multi-dimensional tools with more complex modeling abilities.

At NASA Johnson Space Center, CHarring Ablator Response (CHAR) was developed [33, 34]. It is a 3-dimensional, Galerkin Finite Element Method, first and second

order fully implicit code which can solve charring ablation, Darcian porous flow, and general heat conduction problems. It is unstructured, fully parallelized for efficiency, and contains numerous utilities for solving tailored problems. This code is used both for research and design applications.

In recent years, a new material response tool has also been in development at NASA Ames Research Center, Icarus [35]. This is a finite-volume, unstructured code, with the same material model as the previously mentioned codes but with the intent of being a hybrid research and design code, developed with modern programming techniques making it highly versatile and user friendly.

Most of these codes are in their essence design codes, although they can be used for research applications, they are not developed for this purpose. In academia, material response tools are developed for testing physical models and furthering the understanding of the underlying physics in ablation problems. The Kentucky Aerothermodynamics and Thermal-response System (KATS) is a family of codes which aims to study various aspects of re-entry problems. It contains a stand alone aerothermodynamics [36], material response [37], thermoelastic [38], see Fig. 2.7, radiation [39], and spallation codes [40]. These codes have also been coupled in various manners to promote maximum flexibility for fidelity.

One other noteworthy high-fidelity effort was led by Lachaud et al. [25]. His work contributed to the community not only in the development of a new code Porous-material Analysis Toolbox based on OpenFOAM (PATO) [41], but also in the development of multiscale models based on experimental measurements using scanning electron mi-

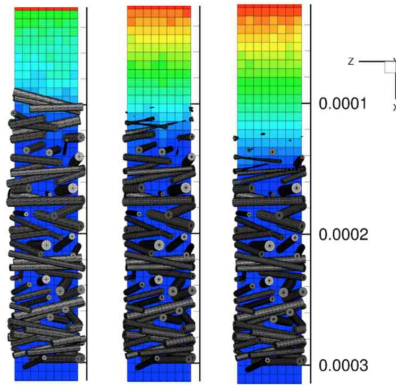


Figure 2.6: DSMC modeling of flow through carbon fiber matrix from Ref. [7].

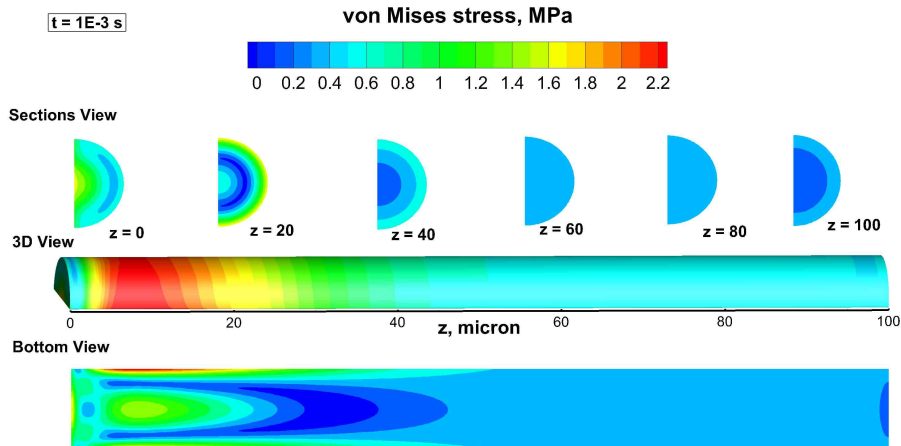


Figure 2.7: Thermomechanical stress on a carbon fiber simulated with KATS-thermoelastic solver.

croscope (SEM) [25, 42]. These models helped understand the oxidation of the porous carbon fibrous materials, and the volumetric ablation process through the layers of the TPS.

Finally, a new method for studying ablation is being achieved using Direct Simulation Monte Carlo [43], Fig. 2.6. These can studies provide insight into micro-scale behavior as well as more accurate material properties which can then be incorporated into a volume-averaged material response solver.

## 2.4 KATS numerical framework

The KATS solver is a multi-component code which contains there main solvers: fluid dynamics (FD), material response (MR), and thermoelastic. The latter can be used as strongly two-way coupled systems or independently. In development is also a Universal Solver [44] which strongly couples the flowfield and the solid domain with one set of equations. The current work pertains to the KATS-FD and KATS-MR solvers but could be applied to other codes as well. KATS utilizes a Finite-Volume-Method (FVM) with Backward-Euler time integration scheme for solving the 3-dimensional

conservation equations. The conservative form of the KATS equations is

$$\underbrace{\frac{\partial \mathbf{Q}}{\partial t}}_{\text{storage}} + \nabla \cdot \left( \underbrace{\mathcal{F}_a}_{\text{advection}} - \underbrace{\mathcal{F}_d}_{\text{diffusion}} - \underbrace{\mathcal{F}_g}_{\text{grid flux}} \right) = \underbrace{\mathbf{S}}_{\text{source}} \quad (2.1)$$

where  $\mathbf{Q}$  is a vector of conservative variables,  $\mathcal{F}_a$  and  $\mathcal{F}_d$  are the advective and diffusive flux matrices,  $\mathcal{F}_g$  is the grid advection flux matrix, and  $\mathbf{S}$  the source term vector. The vector of conserved variables is changed to primitive with the introduction of the Jacobian matrix  $\mathcal{J} = \frac{\partial \mathbf{Q}}{\partial \mathbf{P}}$ , modifying the system to be

$$\underbrace{\frac{\partial \mathbf{Q}}{\partial \mathbf{P}} \frac{\partial \mathbf{P}}{\partial t}}_{\text{storage}} + \nabla \cdot \left( \underbrace{\mathcal{F}_a}_{\text{advection}} - \underbrace{\mathcal{F}_d}_{\text{diffusion}} - \underbrace{\mathcal{F}_g}_{\text{grid flux}} \right) = \underbrace{\mathbf{S}}_{\text{source}}. \quad (2.2)$$

After the spacial integration is applied, and letting  $RHS = -\sum(\mathcal{F}_a - \mathcal{F}_d - \mathcal{F}_g) \cdot \mathbf{n}A + \mathbf{S}V$ , the system that is solved for each computational cell, at every time step is

$$\left[ \frac{V}{\Delta t} \frac{\partial \mathbf{Q}}{\partial \mathbf{P}} - \frac{\partial RHS}{\partial \mathbf{P}} \right] \Delta \mathbf{P} = \mathbf{RHS} \quad (2.3)$$

Here,  $\mathcal{J} = \frac{\partial \mathbf{Q}}{\partial \mathbf{P}}$  is computed analytically and  $\mathcal{J} = \frac{\partial RHS}{\partial \mathbf{P}}$  is computed numerically via forward differencing. This linear system is then solved using PETSc with the GMRES method.

### 2.4.1 Fluid dynamics governing equations

KATS-FD aims to solve the conservation of mass for multispecies gas, the compressible Navier-Stokes equations, and conservation of energy of the gas mixtures in chemical non-equilibrium, for the translation-rotational and vibrational-electronic states. A detailed description of the models and their implementation in this solver

can be found in Ref. [36]. The advective and diffusive flux vector, respectively, are

$$\mathcal{F}_a = \begin{pmatrix} \rho_1 u & \rho_1 v & \rho_1 w \\ \dots & \dots & \dots \\ \rho_{ngs} u & \rho_{ngs} v & \rho_{ngs} w \\ \rho u^2 + p & \rho v^2 & \rho w^2 \\ \rho u^2 & \rho v^2 + p & \rho w^2 \\ \rho u^2 & \rho v^2 & \rho w^2 + p \\ (E + p) u & (E + p) v & (E + p) w \\ E_{ve} u & E_{ve} v & E_{ve} w \end{pmatrix} \quad (2.4)$$

$$\mathcal{F}_d = \begin{pmatrix} -J_{x,1} & -J_{y,1} & -J_{z,1} \\ \dots & \dots & \dots \\ -J_{x,ns} & -J_{y,ns} & -J_{z,ns} \\ \tau_{xx} & \tau_{yx} & \tau_{zx} \\ \tau_{xy} & \tau_{yy} & \tau_{zy} \\ \tau_{xz} & \tau_{yz} & \tau_{zz} \\ \tau \mathbf{u} - (\mathbf{q}_{tr} + \mathbf{q}_{ve}) - \sum_{i=1}^{ns} (\mathbf{J}_i h_i) \\ -q_{ve,x} - \sum_{i=1}^{ns} (J_{x,s} e_{ve,s}) & -q_{ve,y} - \sum_{i=1}^{ns} (J_{y,s} e_{ve,s}) & -q_{ve,z} - \sum_{i=1}^{ns} (J_{z,s} e_{ve,s}) \end{pmatrix} \quad (2.5)$$

and the vectors of conservative variables, primitive variables, and source terms are

$$\mathbf{Q} = \begin{pmatrix} \rho_1 \\ \dots \\ \rho_{ns} \\ \rho u \\ \rho v \\ \rho w \\ E \\ E_{ve} \end{pmatrix} \quad \mathbf{P} = \begin{pmatrix} \rho_1 \\ \dots \\ \rho_{ns} \\ u \\ v \\ w \\ T_{tr} \\ T_{ve} \end{pmatrix} \quad \mathbf{S} = \begin{pmatrix} \dot{\omega}_1 \\ \dots \\ \omega_{ns} \\ 0 \\ 0 \\ 0 \\ 0 \\ \dot{\omega}_v \end{pmatrix}$$

Here,  $J$  are mass diffusion terms,  $\tau$  are the viscous shear stresses, and  $\mathbf{q}$  is heat flux.

### 2.4.2 Governing equations for material response

KATS-MR solves the mass conservation equations for decomposing solids and pyrolysis gas, the momentum balance equation with a Darcian source term for gas transport, and conservation of energy. It is equipped with an aeroheating boundary condition for solving ablation problems, and a fully-implicit mesh-motion scheme for capturing domain change due to ablation [45]. More detailed explanation of the models implemented in this code can be found in Refs. [37, 46, 47]. The advective and diffusive flux vector, respectively, are

$$\mathcal{F}_a = \begin{pmatrix} \phi\rho_g u & \phi\rho_g v & \phi\rho_g w \\ \mathbf{0} \\ \phi\rho_g u^2 + p & \phi\rho_g uv & \phi\rho_g uw \\ \phi\rho_g vu & \phi\rho_g v^2 + p & \phi\rho_g vw \\ \phi\rho_g wu & \phi\rho_g wv & \phi\rho_g w^2 + p \\ \phi\rho_g u h_g & \phi\rho_g v h_g & \phi\rho_g w h_g \end{pmatrix} \quad (2.6)$$

$$\mathcal{F}_d = \begin{pmatrix} \mathbf{0} \\ k \frac{\partial T}{\partial x} & k \frac{\partial T}{\partial y} & k \frac{\partial T}{\partial z} \end{pmatrix} \quad (2.7)$$

$$\mathcal{F}_g = \begin{pmatrix} \phi\rho_g u_{cs} & \phi\rho_g v_{cs} & \phi\rho_g w_{cs} \\ \rho_s u_{cs} & \rho_s v_{cs} & \rho_s w_{cs} \\ \phi\rho_g u u_{cs} & \phi\rho_g u v_{cs} & \phi\rho_g u w_{cs} \\ \phi\rho_g v u_{cs} & \phi\rho_g v v_{cs} & \phi\rho_g v w_{cs} \\ \phi\rho_g w u_{cs} & \phi\rho_g w v_{cs} & \phi\rho_g w w_{cs} \\ (\phi E_g + E_s) u_{cs} & (\phi E_g + E_s) v_{cs} & (\phi E_g + E_s) w_{cs} \end{pmatrix}, \quad (2.8)$$

and the vectors of conservative variables, primitive variables, and source terms are

$$\mathbf{Q} = \begin{pmatrix} \phi \rho_g \\ \rho_{s1} \\ \dots \\ \rho_{nss} \\ \phi \rho_g u \\ \phi \rho_g v \\ \phi \rho_g w \\ \phi E_g + E_s \end{pmatrix} \quad \mathbf{P} = \begin{pmatrix} p \\ \rho_{s1} \\ \dots \\ \rho_{nss} \\ u \\ v \\ w \\ T \end{pmatrix} \quad \mathbf{S} = \begin{pmatrix} \dot{\omega}_g \\ \dot{\omega}_{s1} \\ \dots \\ \dot{\omega}_{nss} \\ -\phi \frac{\mu}{K} u \\ -\phi \frac{\mu}{K} v \\ -\phi \frac{\mu}{K} w \\ \phi \frac{\mu}{K} (u^2 + v^2 + w^2) \end{pmatrix}$$

Here,  $\dot{\omega}$ , is the rate of decomposition of the solid into gas.  $\phi$ ,  $\mu$  and  $K$  are the porosity, viscosity and permeability of the gas, respectively.

## Chapter 3: Verification

Verification is a process used to test numerical tools for their capability to correctly compute the outputs of an existing model. A tool that is verified does not necessarily reflect the real world but is insured to produce the correct solutions for the implemented equations. In order to verify a computational tool, comparisons to analytical solutions and code-to-code comparisons are commonly used. In instances where there are no known solutions, the method of manufactured solutions and grid function convergence tests are used. This section will only encompass the first method.

Although verification is of importance, it is often times a tedious process that must be repeated every time a change is made to the code in order to insure integrity is maintained. For this reason, having a program to automate this process is useful for streamlining code development.

### 3.1 Development of an automated testing toolbox (ATT)

A python-based automated testing tool is developed for the KATS-MR code. The program encompasses a series of tests with analytical solutions which are selected based on user-input. The user can further dictate whether she/he wishes to perform a spacial order of accuracy test or qualitatively compare solutions. The program then runs KATS-MR for the specified problem in a sub-directory containing the KATS inputs. Once KATS has finished running, it then reads the KATS outputs and computes the analytical solution on the cell-centroid coordinate, computes the difference between the numerical and analytical solution, and outputs the error. It repeats this process for a set of three grids of 100, 200, and 400 cell elements, shown in Fig. 3.2, and



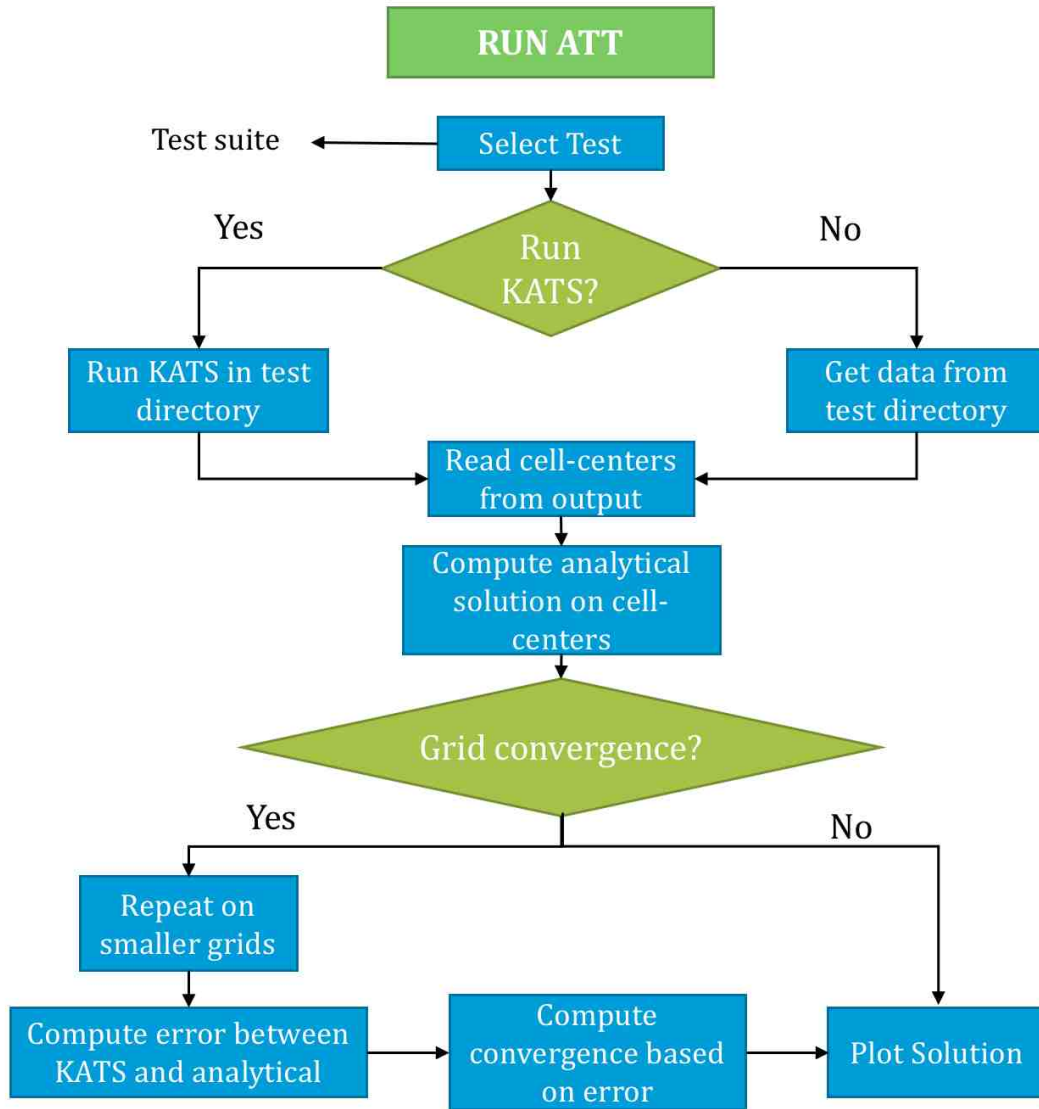


Figure 3.1: Functional diagram of automated testing tool.

computes the error convergence rate. A functional diagram of the program is shown in Fig. 3.1. Finally, the program plots either the solutions or the grid-convergence test and saves it to a specified directory.

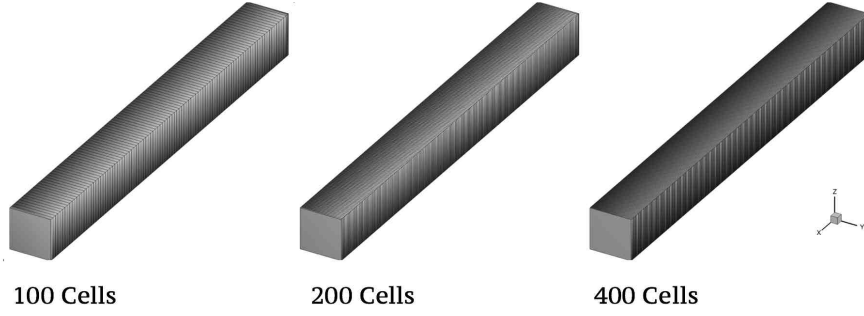


Figure 3.2: Meshes used in grid convergence test.

### 3.2 Grid-function convergence testing

If a function to be approximated is  $f_i$ , at grid spacing  $h$ , t

$$f_i^h = f(x_i) + \tau_1 h^{q_1} + \dots = f(x_i) + O(h^{q_1}). \quad (3.1)$$

the truncation error associated with that expansion is of the order of  $O(h^{q_1})$ . To determine the order of accuracy of a solution procedure, one can repeat the process on a grid of size  $h$ ,  $h/2$ ,  $h/4$ , where the expansions would be

$$\begin{aligned} f_i^h &= f(x_i) + \tau_1 h^{q_1}, \\ f_i^{h/2} &= f(x_i) + 2^{-q_1} \tau_1 h^{q_1}, \\ f_i^{h/4} &= f(x_i) + 4^{-q_1} \tau_1 h^{q_1} \end{aligned} \quad (3.2)$$

Here the  $i$  denotes the cell index at which the solution is being evaluated in common. Thus if the  $h$  grid function is subtracted by the  $h/2$ , and divide by the difference between the smaller spaced grid, Eq. 3.2 can be rearranged

$$\frac{f_i^h - f_i^{h/2}}{f_i^{h/2} - f_i^{h/4}} = 2^{q_1}. \quad (3.3)$$

Here  $q_1$  is the theoretical convergence rate, and Eq. 3.3 can be rearranged to give

$$q_1 = \frac{\log \left[ \frac{f_i^h - f_i^{h/2}}{f_i^{h/2} - f_i^{h/4}} \right]}{\log 2} \quad (3.4)$$

This value is the give the order of accuracy of a scheme and, as the name indicates, for second order schemes should be approximately 2. The root-mean-squared error can be determined at each grid spacing  $h$ . The root-mean-squared (RMS) is determined as

$$e_{RMS} = \sqrt{\frac{\sum_{i=1}^n (T_{\text{analytical}} - T_{\text{numerical}})_{i,\text{time}}^2}{n}}. \quad (3.5)$$

where  $i$  is the cell index. The convergence rate of the error can therefore be calculated as

$$q = \frac{\log \left[ \frac{e^h - e^{h/2}}{e^{h/2} - e^{h/4}} \right]}{\log 2}. \quad (3.6)$$

In the following section, the RMS is used as the error metric and grid-convergence tests are performed using this methodology.

### 3.3 Test suite of analytical solutions

There are a variety of analytical solutions to heat conduction and porous flow problems that can be used to test separate utilities and/or parts of the solver. Since the KATS solver is used for a variety of different problems, the verification cases attempt to verify modularly the various functionalities of the code, varying from boundary conditions, to models, and utilities.

#### 3.3.1 Transient conduction with fixed temperature boundary condition

##### Problem description

This problem consists of a 1-dimensional finite-slab, with an imposed temperature on one side. It is intended to verify the transient heat conduction through with a Dirichlet boundary condition. The domain is a non-ablating, non-decomposing slab with length,  $l$ . A specified temperature is imposed on the face at  $x = 0$ . The governing equation, initial and boundary conditions that describe this problem are, respectively:

$$\rho C_v \frac{\partial T}{\partial t} = k \frac{\partial^2 T}{\partial z^2} \quad \text{for } 0 \leq x \leq l \quad (3.7)$$

$$T(x, 0) = T_0 \quad (3.8)$$

$$T(x = l, t) = T_w \quad (3.9)$$

$$-k \frac{\partial T}{\partial x} \Big|_{x=0} = 0 \quad (3.10)$$

The analytical solution to this problem, from Bird et al. [48], can be expressed as

$$\frac{T_w - T}{T_w - T_0} = 2 \sum_{n=0}^{\infty} \frac{(-1)^n}{(n + \frac{1}{2})\pi} \exp \left[ - \left( n + \frac{1}{2} \right)^2 \pi^2 \alpha t / l^2 \right] \cos \left( n + \frac{1}{2} \right) \frac{\pi x}{l}. \quad (3.11)$$

### Test parameters

The parameters used in this problem are shown in Table 3.1.

Table 3.1: Fixed temperature boundary condition verification problem parameters.

Parameter	Value	Unit
$T_0$	300	K
$T_w$	500	K
$l$	0.01	m
$\rho$	8000	kg/m <sup>3</sup>
$C_v$	500	J/(kg·K)
$k$	10	W/(m·K)
$\alpha = k/(\rho C_v)$	$2.5 \times 10^{-6}$	m <sup>2</sup> /s

### Results

The comparison with analytical solution and the corresponding grid convergence study is shown in Figs. 3.3a and 3.3b.

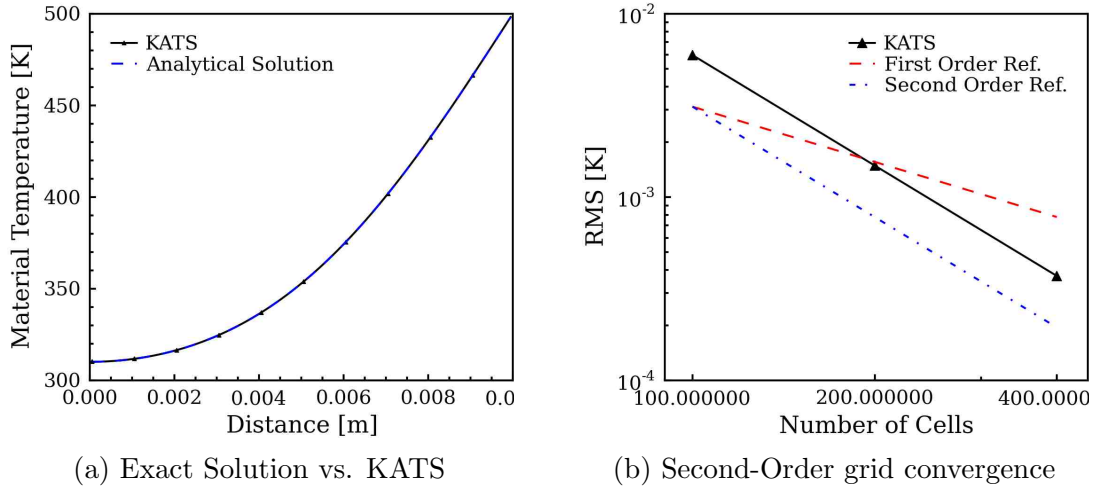


Figure 3.3: Fixed temperature wall boundary condition verification.

### 3.3.2 Transient conduction with a fixed heat flux boundary condition

#### Problem description

This problem is intended to verify the transient heat conduction through a 1-dimensional slab with a Neumann boundary condition [49, 50]. This verification case, although simple, is important because the most commonly used boundary conditions in ablation problems are of the second kind. Although there are models to increase the fidelity and account for more physics at the boundary (i.e. film coefficient model), the boundary conditions still reduce to this type. The governing equation, initial condition, and boundary conditions for this problem are

$$\rho C_v \frac{\partial T}{\partial t} = k \frac{\partial^2 T}{\partial x^2} \quad \text{for } 0 \leq x \leq l \quad (3.12)$$

$$T(x, 0) = T_0 \quad (3.13)$$

$$-k \frac{\partial T}{\partial x} \Big|_{x=0} = \dot{q}'' \quad (3.14)$$

$$-k \frac{\partial T}{\partial x} \Big|_{x=l} = 0 \quad (3.15)$$

The analytical solution is the following:

$$\frac{T - T_0}{\dot{q}'' l / k} = \frac{\alpha t}{l^2} + \frac{1}{3} - \frac{x}{l} + \frac{1}{2} \left( \frac{x}{l} \right)^2 - \frac{2}{\pi^2} \sum_{n=1}^{\infty} \frac{1}{n^2} \exp \left( -n^2 \pi^2 \frac{\alpha t}{l^2} \right) \cos \left( n \pi \frac{x}{l} \right). \quad (3.16)$$

### Test parameters

The parameters for this problem are shown in Table 3.2.

Table 3.2: Applied heat flux boundary condition verification problem parameters.

Parameter	Value	Unit
$T_0$	300	K
$\dot{q}''$	$7.5 \times 10^5$	W/m <sup>2</sup>
$l$	0.01	m
$\rho$	8000	kg/m <sup>3</sup>
$C_v$	500	J/(kg·K)
$k$	10	W/(m·K)
$\alpha = k/(\rho C_v)$	$2.5 \times 10^{-6}$	m <sup>2</sup> /s

## Results

The performance of KATS as compared with the analytical solution and the corresponding grid convergence test is shown in Figs. 3.4a and 3.4b.

### 3.3.3 Transient conduction with a time-varying heat flux boundary condition

#### Problem description

This problem is similar in nature to the previous one, except that the boundary condition itself is changing with respect to time. It is important because the nature of ablation problem is inherently transient, as the atmospheric and subsequently thermochemical properties of the boundary layer change during a flight trajectory.

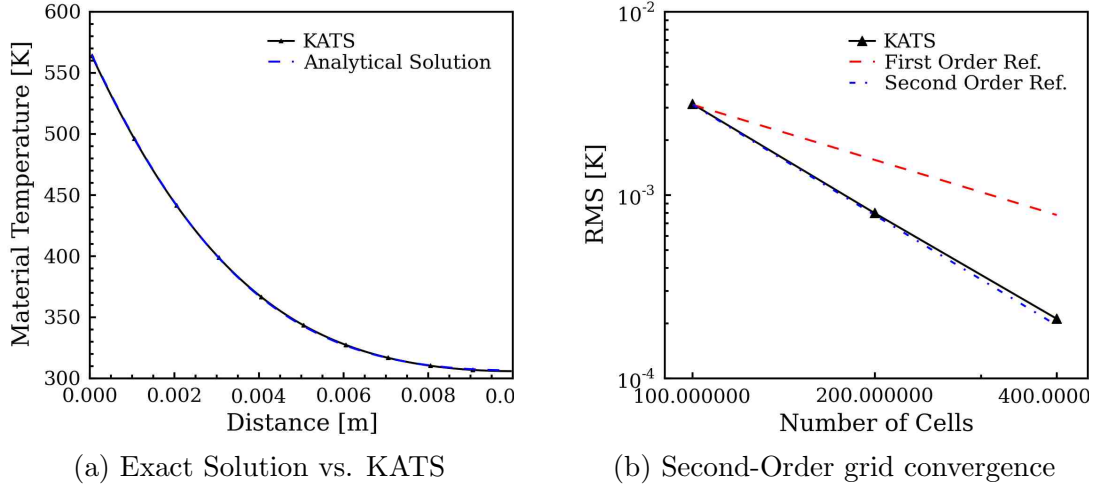


Figure 3.4: Fixed heat flux boundary condition

Therefore the code must be capable of adequately capturing these effects. A heat flux as a function of time that follows the expression:

$$\dot{q}'' = \dot{q}_0'' \cos(\omega t) \quad (3.17)$$

is applied to the face at  $x = 0$ , where  $\omega$  is the frequency of the heat pulse. The governing equation, initial, and boundary conditions to this problem are, respectively

$$\rho C_v \frac{\partial T}{\partial t} = k \frac{\partial^2 T}{\partial x^2} \quad \text{for } 0 \leq x \leq l \quad (3.18)$$

$$T(x, 0) = T_0 \quad (3.19)$$

$$-k \frac{\partial T}{\partial x} \Big|_{x=0} = \dot{q}''(t) \quad (3.20)$$

$$-k \frac{\partial T}{\partial x} \Big|_{x=l} = 0 \quad (3.21)$$

The analytical solution as described in Ref. [48], is

$$T - T_0 = \frac{q_0}{k} \sqrt{\left(\frac{\alpha}{\omega}\right)} \exp\left(-x\sqrt{\omega/2\alpha}\right) \cos\left(\omega t - \sqrt{\frac{\omega}{2\alpha}}x - \frac{\pi}{4}\right). \quad (3.22)$$

## Test parameters

The parameters used in this problem are shown in Table 3.3.

Table 3.3: Time-varying applied heat flux boundary condition verification problem parameters.

Parameter	Value	Unit
$T_0$	300	K
$\dot{q}_0$	$7.5 \times 10^5$	$\text{W}/\text{m}^2$
$\omega$	$2\pi$	1/s
$l$	0.01	m
$\rho$	8000	$\text{kg}/\text{m}^3$
$C_v$	500	$\text{J}/(\text{kg}\cdot\text{K})$
$k$	10	$\text{W}/(\text{m}\cdot\text{K})$
$\alpha = k/(\rho C_v)$	$2.5 \times 10^{-6}$	$\text{m}^2/\text{s}$

## Results

The resulting comparison between KATS and the analytical solution is shown in Fig. 3.5b. Figure 3.5a shows the time-dependent boundary condition that is applied.

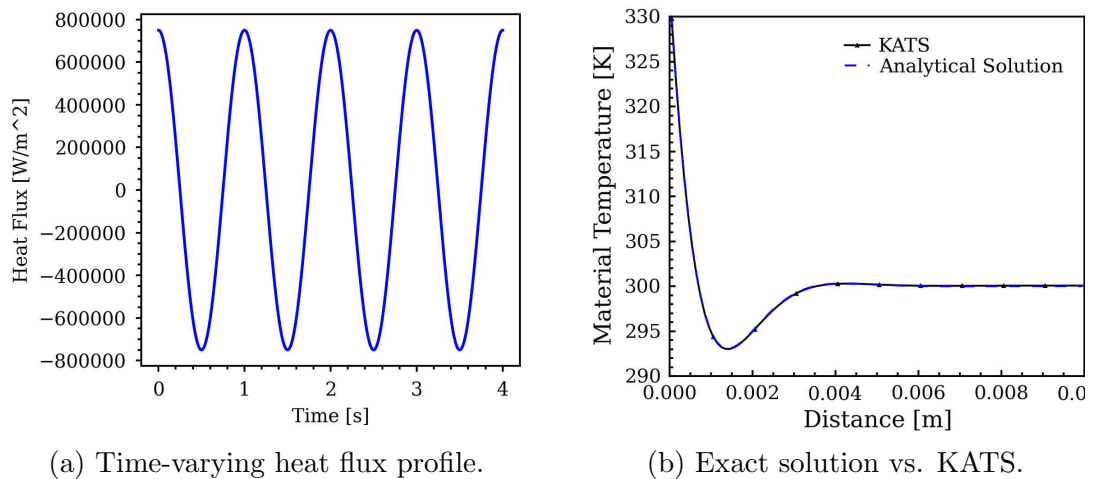


Figure 3.5: Exact solution vs. KATS



### 3.3.4 Fixed heat flux boundary condition with temperature dependent thermal properties

#### Problem description

This problem employs the same boundary condition as the fixed heat flux problem. However, in this case, the material thermal properties are defined by their linear dependence on temperature. The objective of this is to verify the temperature dependent thermal properties model in KATS. This is important because in real ablation problems the thermal properties of materials are complex. These almost always contain temperature dependency, orthotropy and non-uniformity. This problem only captures the temperature dependence. The governing equation, initial, and boundary conditions of this problem are

$$\rho C_v \frac{\partial T}{\partial t} = \frac{\partial}{\partial x} \left( k(T) \frac{\partial T}{\partial x} \right) \quad \text{for } 0 \leq x \leq l \quad (3.23)$$

$$T(x, 0) = T_0 \quad (3.24)$$

$$-k \frac{\partial T}{\partial x} \Big|_{x=0} = \dot{q}(t) \quad (3.25)$$

$$-k \frac{\partial T}{\partial x} \Big|_{x=l} = 0 \quad (3.26)$$

Let the thermal conductivity and heat capacity be defined, respectively, as

$$k(T) = k_1 + \frac{k_2 - k_1}{T_2 - T_1} (T - T_1) \quad (3.27)$$

$$C_v(T) = C_{v,1} + \frac{C_{v,2} - C_{v,1}}{T_2 - T_1} (T - T_1). \quad (3.28)$$

subsequently the thermal diffusivity, which is a function of both thermal conductivity and heat capacity, is defined as

$$\alpha = \frac{k_1}{\rho C_{p,1}} = \frac{k_2}{\rho C_{p,2}} = \frac{k(T)}{\rho C_p(T)} \quad (3.29)$$

References [49, 50] describe the derivation of the analytical solution to this problem.

Let,

$$\theta = (T - T_1) + \frac{k_2 - k_1}{T_2 - T_1} \frac{1}{2k_1} (T - T_1)^2 \quad (3.30)$$

then the analytical solution for the temperature distribution is given by

$$\frac{\theta(z, t) - \theta_0}{\dot{q}l/k_1} = \frac{\alpha t}{l^2} + \frac{1}{3} - \frac{y}{l} + \frac{1}{2} \left(\frac{y}{l}\right)^2 - \frac{2}{\pi^2} \sum_{n=1}^{\infty} \frac{1}{n^2} \exp\left(-n^2 \pi^2 \frac{\alpha t}{l^2}\right) \cos\left(n \frac{\pi y}{l}\right) \quad (3.31)$$

rearranging for the temperature,

$$T = T_1 - (T_2 - T_1) \left(\frac{k_1}{k_2 - k_2}\right) \left[-1 + \sqrt{1 + \frac{2\theta}{T_2 - T_1} \left(\frac{k_2 - k_1}{k_1}\right)}\right] \quad (3.32)$$

### Test parameters

The thermal-dependent parameters used in this problem are shown in Table 3.4, and the remaining parameters for the problem set-up are shown in Table 3.5

Table 3.4: Material properties for temperature dependent properties verification problem.

$T$ [K]	$k$ [W/m·K]	$C_v$ [J/(kg·K)]
$T_1 = 300$	10	500
$T_2 = 1300$	100	5000

Table 3.5: Simulation parameters for temperature-dependent thermal properties conduction verification problem parameters.

Parameter	Value	Unit
$T_0$	300	K
$\dot{q}''$	$7.5 \times 10^5$	W/m <sup>2</sup>
$L$	0.01	m
$\rho$	8000	kg/m <sup>3</sup>
$\alpha = k/(\rho C_v)$	$2.5 \times 10^{-6}$	m <sup>2</sup> /s

### Results

The resulting comparison between KATS and the analytical solution is found in Fig. 3.6.

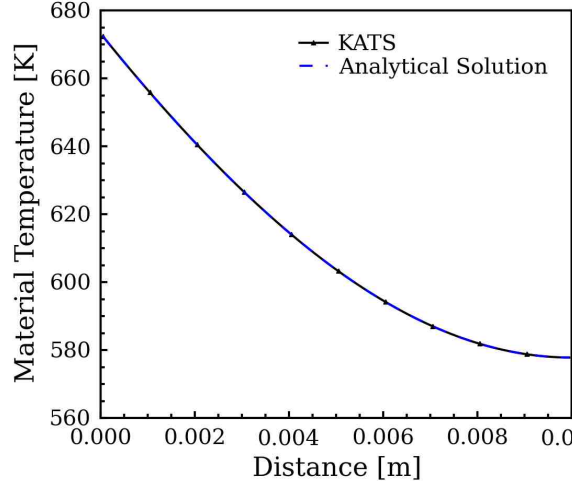


Figure 3.6: Linearly temperature dependent thermal properties conduction verification problem.

### 3.3.5 Aeroheating convection boundary condition

#### Problem description

This problem is intended to verify the aeroheating boundary condition and the use of thermochemical equilibrium  $B'$  tables. The aeroheating boundary condition is expressed as

$$q_{aero} = \rho_e u_e C_h (h_r - h_w) \quad (3.33)$$

where,  $\rho_e u_e C_h$  is the heat transfer coefficient (a function of the boundary layer edge properties),  $h_r$  is the recovery enthalpy, and  $h_w$  is the wall enthalpy. The governing equation and boundary and initial conditions are

$$\rho C_v \frac{\partial T}{\partial t} = k \frac{\partial^2 T}{\partial x^2} \quad \text{for } 0 \leq x \leq l \quad (3.34)$$

$$-k \frac{\partial T}{\partial x} \Big|_{x=0} = 0 \quad (3.35)$$

$$-k \frac{\partial T}{\partial x} \Big|_{x=L} = \rho_e u_e C_h (h_r - h_w) \quad (3.36)$$

$$T(x, 0) = T_0. \quad (3.37)$$

The analytical solution is derived in Ref. [49]. First, the eigenvalues of the relation

$$\nu_n \sin(\nu_n) = Bi \cos(\nu_n) \quad (3.38)$$

are found, where the Biot number is defined as

$$Bi = \frac{\rho_e u_e C_h C_p l}{k} \quad (3.39)$$

The analytical solution is given by

$$T = T_r + 2(T_0 - T_r) \sum_{n=1}^{\infty} \left( \frac{\sin \nu_n}{\nu_n + \sin \nu_n \cos \nu_n} \right) \exp \left( \frac{-\nu_n^2 \alpha t}{l^2} \right) \cos \left( \frac{\nu_n x}{l} \right). \quad (3.40)$$

### Test parameters

The parameters used in this problem are shown in Table 3.6. The surface chemistry

Table 3.6: Aeroheating convection verification problem parameters.

Parameter	Value	Unit
$T_0$	300	K
$h_r$	$1.3 \times 10^5$	J/kg
$L$	0.01	m
$\rho$	8000	kg/m <sup>3</sup>
$C_v$	500	J/(kg·K)
$k$	10	W/(m·K)
$\alpha = k/(\rho C_v)$	$2.5 \times 10^{-6}$	m <sup>2</sup> /s

data is provided in Table 3.7.

Table 3.7: Surface thermochemistry

$T$ [K]	$h_w$ [J/kg]
0.0	0.0
2000	$2.0 \times 10^6$

## Results

The resulting KATS solution compared with the analytical solution and the grid convergence test are shown in Figs. 3.7a and 3.7b.

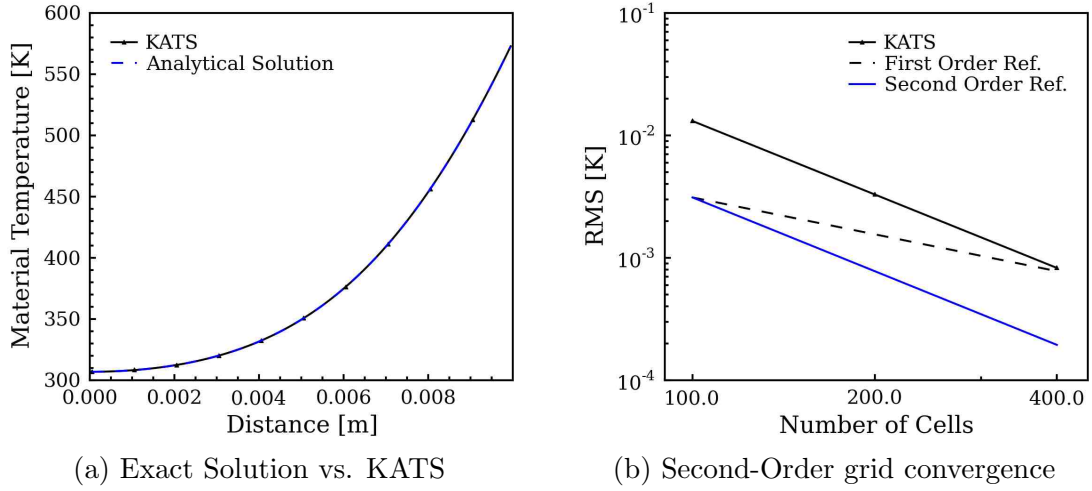


Figure 3.7: Convective aeroheating boundary condition verification.

### 3.3.6 Steady-state re-radiation boundary condition

#### Problem description

One important characteristic of commonly used ablative materials is their thermal emissivity, in other words, their ability to re-radiate much of the heat that is absorbed by the surface. Most material response codes have a re-radiative boundary condition to account for this phenomena. The governing equation, boundary conditions and initial condition used in this problem are

$$\frac{\partial^2 T}{\partial x^2} = 0 \quad \text{for } 0 \leq x \leq l \quad (3.41)$$

$$-k \frac{\partial T}{\partial x} \Big|_{x=0} = \epsilon \sigma (T_\infty^4 - T_w^4) \quad (3.42)$$

$$T(x = l, t) = T_{x=l} \quad (3.43)$$

Because this problem is a steady-state solution, the heat which is conducted into the material must be equal to what is re-radiated. Thus, the analytical solution is

$$\sigma\epsilon(T_\infty^4 - T_w^4) = \frac{k}{l}(T_w - T_{x=l}) \quad (3.44)$$

### Test parameters

The problem parameters are shown in Table 3.8

Table 3.8: Steady-state radiation verification problem parameters.

Parameter	Value	Unit
$k$	10	W/(m·K)
$\epsilon$	0.9	
$\sigma$	$5.6704 \times 10^{-8}$	W/(m <sup>2</sup> ·K <sup>4</sup> )
$T_\infty$	1300	K
$T_{x=0}$	300	K
$l$	0.01	m

### Results

A Newton method is used for solving this problem. Figure 3.8 shows the wall temperature as computed in KATS as time passes, until steady-state is reached.

#### 3.3.7 Steady-state porous flow

##### Problem description

In order to simulate in-depth ablating materials, it is necessary to accurately capture the porous flow of pyrolysis gas through the materials. The gas flow is generated from the decomposition of phenolic resin infused in the materials for attenuating heating. KATS contains two options for how to describe the gas flow: the unsteady, volume-averaged momentum equation (Darcy-Brinkman), and Darcy's Law whose

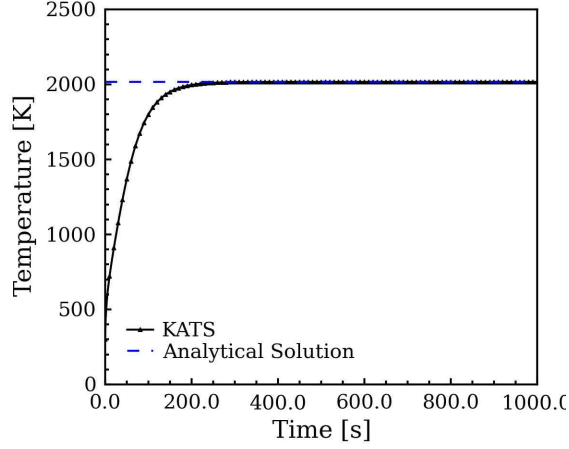


Figure 3.8: Steady-state radiation verification.

implementation is discussed in Section 6. This verification only applied to the latter, as it is a steady-state problem. The derivation to this verification problem can be found in Ref. [51]. The governing equation and boundary conditions are

$$\nabla \cdot (\phi \rho_g \mathbf{u}_g) = 0 \quad (3.45)$$

$$\rho_g(x = 0) = \rho_{g_o} \quad (3.46)$$

$$\rho_g(x = l) = \rho_{g_i} \quad (3.47)$$

The following is a derivation of the analytical solution to steady porous flow through isotropic material following Darcy's Law. We start with the statement of Darcy's Law, for a volume averaged approach

$$\mathbf{u}_g = \frac{-K}{\phi \mu} \nabla P. \quad (3.48)$$

Assuming the gas in question follows the ideal gas law,

$$\mathbf{u}_g = \frac{-K}{\phi \mu} \nabla (\rho_g RT). \quad (3.49)$$

because the material is isothermal,

$$\mathbf{u}_g = \frac{-KRT}{\phi\mu} \nabla \rho_g \quad (3.50)$$

Now, we can express the gas continuity equation, Eq. 3.45, as

$$\nabla \cdot \left( \rho_g \frac{KRT}{\mu} \nabla \rho_g \right) = 0 \quad (3.51)$$

which is itself the solution to the gas continuity equation for a steady porous flow which follows the ideal gas and Darcy's Law. For an isotropic material i.e. thermal material properties are equal in all directions, their gradient is zero, thus

$$\frac{KRT}{\mu} \nabla \cdot (\rho_g \nabla \rho_g) = 0. \quad (3.52)$$

where the one-dimensional case can be expressed as

$$\frac{d}{dx} \left( \rho_g \frac{d\rho_g}{dx} \right) = 0. \quad (3.53)$$

or

$$\rho_g \frac{d\rho_g}{dx} = C \quad (3.54)$$

where  $C$  is a constant. In order to obtain the spacial distribution of the gas density, the previous equation can be integrated where the limits of the integral are the boundary conditions, then using separation of variables,

$$\int_{\rho_{g0}}^{\rho_{gl}} \left[ \frac{d}{dx} \left( \rho_g \frac{d\rho_g}{dx} \right) \right] dx = 0. \quad (3.55)$$

which gives

$$\rho_g(x) = \left[ \frac{\rho_{gl}^2 - \rho_{g0}^2}{l} x + \rho_{g0}^2 \right]^{1/2}. \quad (3.56)$$

Now that the gas density is known, again invoking the ideal gas law, and substituting  $\rho_g = P/RT$ , the pressure field is given by

$$P(x) = \left[ \frac{P_l^2 - P_0^2}{l} x + P_0^2 \right]^{1/2}. \quad (3.57)$$



Table 3.9: Steady porous flow problem parameters.

Parameter	Value	Unit
$L$	0.01	$m$
$\rho_{g0}$	1	$\text{kg}/\text{m}^3$
$\rho_{gl}$	0.1	$\text{kg}/\text{m}^3$
$R$	300	$\text{J}/(\text{kg}\cdot\text{K})$
$T$	300	$K$
$\mu$	$1 \times 10^{-6}$	$\text{Pa}\cdot\text{s}$
$K$	$1 \times 10^{-15}$	$\text{m}^2$
$P_0$	90000	$\text{Pa}$
$P_l$	9000	$\text{Pa}$

### Test parameters

The simulation parameters for this problem are shown in Table 3.9

### Results

The comparison between the KATS gas density profile and the analytical solution derived above is shown in Fig. 3.9a as well as the grid-convergence study in Fig. 3.9b.

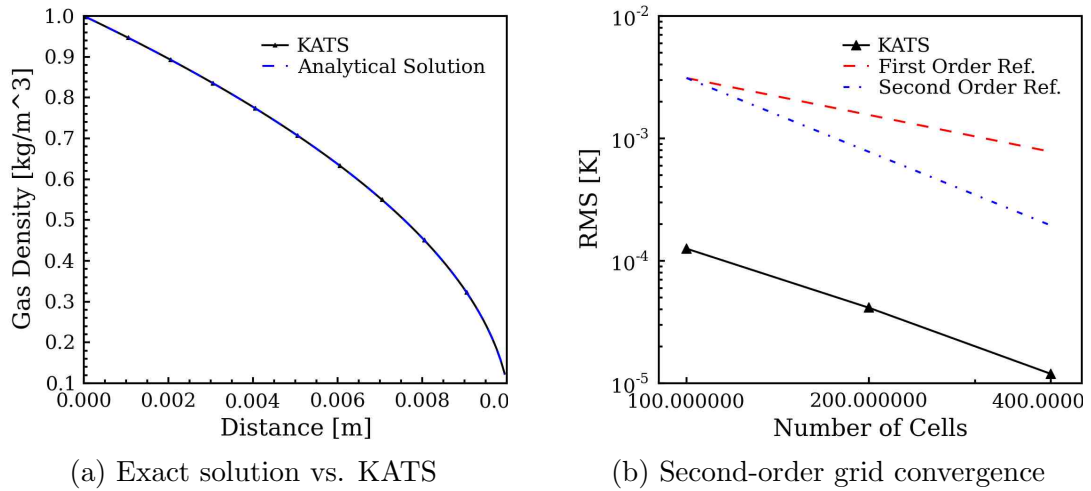


Figure 3.9: Steady porous flow verification

### 3.4 Mesh motion verification

It is important, for ablation problems, to be able to capture the physical change in domain shape and size. This requires both the implementation of a mesh motion algorithm as well as a flux and volumetric balancing scheme. A detailed description of the derivation of these schemes can be found in Ref. [45]. This section focuses on the verification of the grid advection and volumetric balancing scheme for each of the conservation equations solved in KATS-MR.

#### 3.4.1 Compressed gas

This problem acts in defiance of a real ablation problem. While in ablation solid mass removal is the physical reason for the change in domain size, this is a domain compression problem. This acts to verify the conservation of gas mass through a volume change.

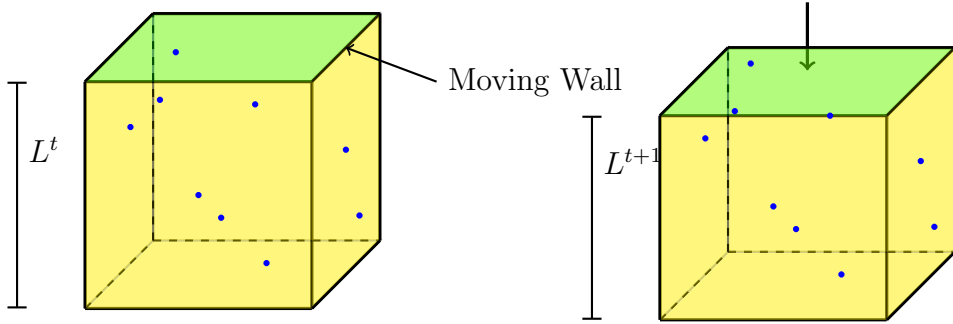


Figure 3.10: Compressed gas problem

A unit cube of gas is compressed to half of its original volume. The top wall is given a recession rate of  $\dot{s} = 0.01$  m/s, for 50 seconds. Figure 3.10 depicts the problem.

The governing equation is

$$\frac{\partial \rho_g}{\partial t} = -\frac{\Delta V}{\Delta t} \rho_g, \quad (3.58)$$

The pressure of the gas is computed in KATS and compared to the trend given by the ideal gas law for each new volume. The comparison between KATS and the ideal gas law is shown in Fig. 3.11.

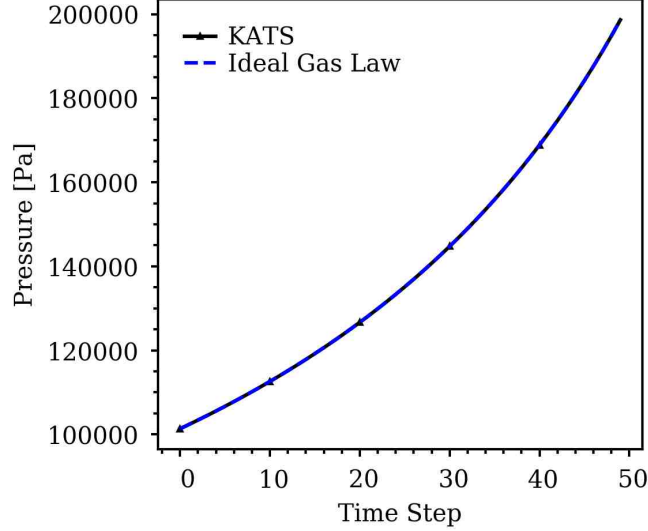


Figure 3.11: Computed ideal gas law using KATS gas mass equation

### 3.4.2 Solid mass removal

This problem depicts the removal of solid mass similar to an ablation problem. It is intended to verify the conservation of solid mass equation on a changing control volume through mass removal. A unit cube of material with uniform density is given a recession vector at the top face while the others remain fixed. The problem setup is shown in Fig. 3.12. The governing equation for this system is given by

$$\frac{\partial \rho_s}{\partial t} = - \left[ \sum_f (\rho_s \mathbf{v}_{cs}) \cdot \hat{n} A - \frac{\Delta V}{\Delta t} \rho_s \right] \quad (3.59)$$

where  $\mathbf{v}_{cs}$  is the face velocity due to mesh motion.

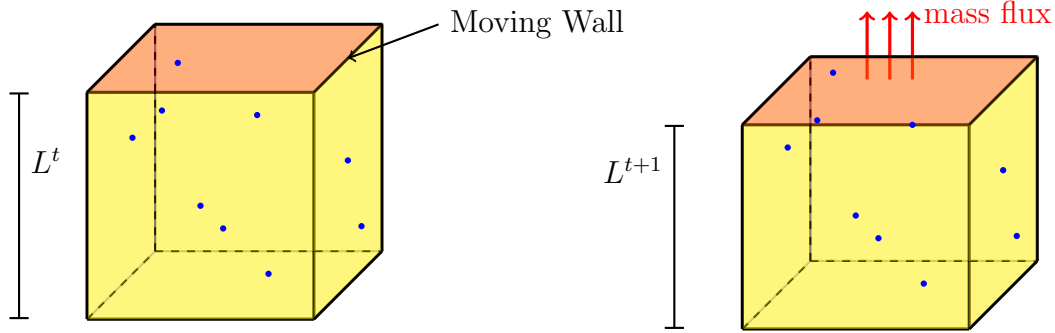


Figure 3.12: Mass flux problem

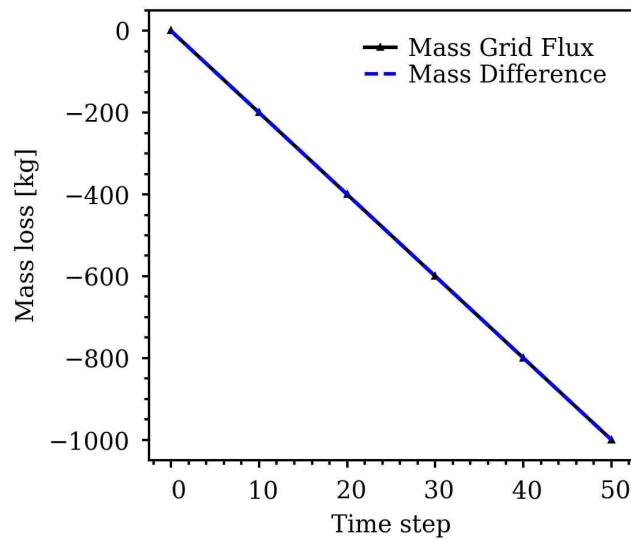


Figure 3.13: Surface mass flux vs. volumetric loss

The moving face generates a flux of mass outward and is balanced by the volumetric term, thus preserving density. As the volume decreases to half the initial volume, the mass loss reaches half the initial mass. The mass flux computed with KATS matches the volumetric loss to machine precision, as shown in Figs. 3.13.

### 3.4.3 Expanding channel

This problem is intended to verify the grid flux and volumetric balancing term implementation for the conservation of momentum equation. A unit cube where a constant

density gas is injected across one face at a constant velocity  $u_{gas}$  while the opposing wall expands at an exactly equal rate  $u_{cs}$  is considered.

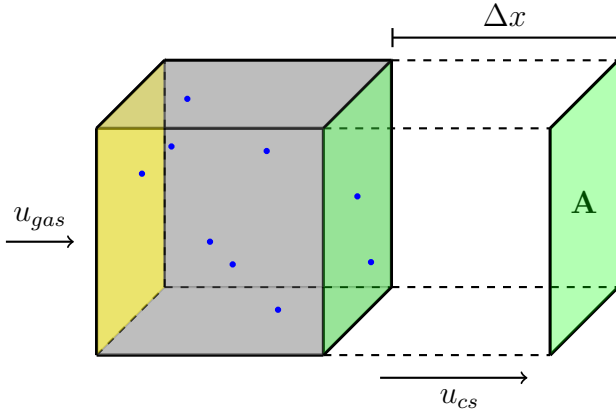


Figure 3.14: Expanding channel problem

The problem parameters are shown in Table 3.10. It is shown, to machine pre-

Table 3.10: Expanding channel parameters

$u_{gas}$ [m/s]	$u_{cs}$ [m/s]	$\rho_{gas}$ [kg/m <sup>3</sup> ]	$\Delta t$ [s]	Area [m <sup>2</sup> ]	$\Delta x$ [m]	$\Delta V$ [m <sup>3</sup> ]
0.01	0.01	2	0.01	1	1	1

cision, that the gas maintains a constant velocity despite the volume change which induces a flux due to grid advection. The flux is balanced by the volumetric balancing term and the primitive variable, in this case velocity, is conserved as shown in Table 3.11.

#### 3.4.4 Constant temperature ablator

This problem is intended to verify the energy conservation equation on a deforming control volume. A slab of homogeneous, constant thermal property, solid material

Table 3.11: Expanding channel results.

	State 1	State 2
Velocity [m/s]	0.01	0.01
Volume [m <sup>3</sup> ]	1	2

is given a constant temperature through the domain. The material is then given a recession vector. Although the temperature of the domain should remain the same everywhere, the domain loses the energy associated with the mass that was removed. This verifies the grid flux and volumetric balancing term associated with the conservation of energy equation. The amount of energy lost due to the change in volume from a specified mass loss is given by

$$\sum_k \rho_s c_p T_{sf} \mathbf{v}_{cs} A \Delta t_k = \sum_i E_i - \sum_f E_f = \sum_i \rho_s c_p T_i V_i - \sum_f \rho_s c_p T_f V_f. \quad (3.60)$$

The comparison between the flux of energy calculated in KATS, and the energy lost from a energy balance calculation is shown in Fig. 3.15. These are shown to match to machine precision.

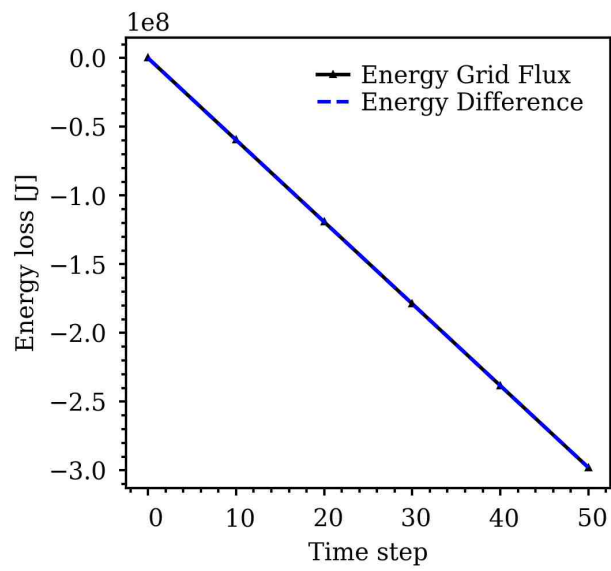


Figure 3.15: Surface energy flux vs. volumetric loss

## Chapter 4: Flow Field Studies

Ground testing facilities can replicate specific flight parameters in order to understand the response of thermal protection systems at a lower cost and higher replicability than flight testing. Arc jets are considered one of the best means to study, test, and characterize thermal protection systems. In an arc jet, a gas is heated by means of an electric arc, and then accelerated through a converging-diverging nozzle, expanding at supersonic speeds. However, there are limitations to these facilities. These limitations include the maximum heat flux is lower than some missions, not all types of gas can be operated with, and there can be contaminants in the flow from eroded articles from electrodes. One other significant disadvantage is that not all entry conditions can be simulated simultaneously (i.e. pressure, shear, enthalpy, heat flux, gas velocity cannot all be replicated at the same time) [52]. As such, it is also important for computational modelers to be able to simulate the arc-jet environments. The reasons behind this are threefold. First, the ability to accurately simulate the arc-jet environment provides a means of validation to the numerical tools. If one cannot computationally simulate arc-jet flow to some degree of certainty, there is no reason to assume that this tool is capable of simulating a true entry environment. Second, computational tools can assist in designing and characterizing ground testing facilities by providing insight into unmeasured parameters. They can also be aid in interpreting experimental results.

This chapter will focus on the efforts to both validate and asses the capabilities of KATS-FD in replicating arc jet environments across two distinct testing facilities.



## 4.1 Numerical methods and models

Although KATS-FD contains a variety of different models for various types of problems, a specific set of these are selected for their best performance in what concerns arc jet problems. The convective flux vector uses a modified Steger-Warming [53] flux-splitting scheme for adding numerical dissipation to the shock and stabilize the solution. Arc jet flow, like the flow during entry, is in chemical non-equilibrium. To account for this, Park's two-temperature model is used [54]. In this model, the dissociation reactions are determined by two temperatures, the translational-rotational temperature  $T_{tr}$ , and the vibrational-electronic temperature  $T_{ve}$ . These are associated with different modes in which the molecules are excited. The degree of non-equilibrium is determined by these two temperatures. In order to solve the vibrational-electronic energy equation, a relaxation model is needed. There are five relaxation energy source terms: energy exchange due to chemical reactions, translational-vibrational energy exchange, electronic-vibrational energy exchange, work on electrons, and energy exchange due to impact ionizations [36]. In these simulations, only the first two are considered since the temperature remains below electronic excitation temperatures. The energy exchange due to chemical reactions is calculated using the non-preferential model, where molecules are created or consumed at the average vibrational energy as opposed to a preferential vibrational energy level. The translational-vibrational energy exchange is the mode which account for the most energy total energy exchange. For temperatures below  $\approx 8000$  K the model used to account for this is the Landau-Teller [55] model, which assumes there is a molar averaged relaxation time which can be used for computing the energy exchange rate. Milikan and White [56] developed a semi-empirical relation between the relaxation time and temperature for this range. Modifications to this model are also available for temperatures higher than  $\approx 8000$  K, but are not pertinent to this work. For the transport properties, Blottner [57] curve fits are used to compute the viscosity.

The species thermal conductivities is computed based on the species viscosity using Eucken’s [55] relations. Wilkes [58] semi-empirical mixing rule is then used to approximate the bulk transport properties (i.e. viscosity and thermal conductivity) based on the previous models. This model is known to be accurate up to  $\approx 10,000$  K, above which Gupta’s [59] mixing rule and integration method for viscosity is known to be more appropriate.

## **4.2 TP3 7.5-inch nozzle**

In order to validate the capability of KATS-FD, a code-to-code comparison is performed on a 7.5 in nozzle in the Aerodynamic Heating Facility’s (AHF) TP3 arc-heater. This is a 10 MW arc-heater with the capability of generating wide ranges of pressure and mass flow rate injection conditions. The code that KATS-FD compares to is Data Parallel Line Relaxation (DPLR) [60]. This is widely used tool, developed at NASA Ames Research Center, for simulating hypersonic flows. It has been extensively verified and validated. Therefore, by comparing KATS-FD with DPLR we are verifying the models that are common to both codes, and validating KATS by extension. The DPLR simulation was leveraged from the literature, and can be found in Ref. [61].

### **4.2.1 Computational geometry**

The geometry of the nozzle is first drawn using Creo Parametric [62] and the corresponding engineering drawing is found in Appendix 1. The computational domain presented in Fig. 4.1 is assembled in Pointwise [63]. The domain is tested for grid convergence, and the shock region is aligned and sized to be one cell thick. The final computational domain contains 28,914 cells from the nozzle inlet to the nozzle exit, 49,612 cells from the nozzle exit to the shock layer, and 37,399 cells in the post shock region to the sample surface. The total cell count is 115,925. The size of this grid

was chosen following a grid convergence study.

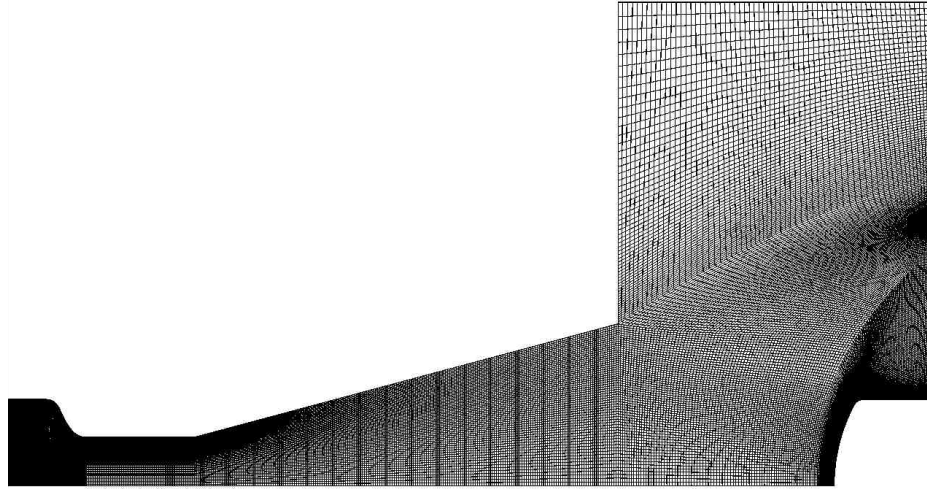
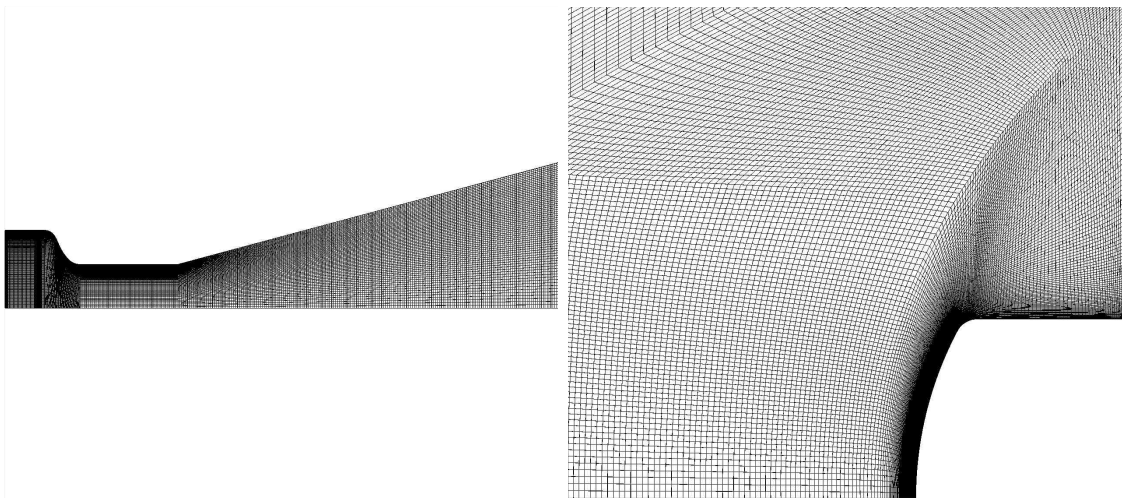


Figure 4.1: Computational grid for TP3 7.5 in nozzle and chamber.



(a) Computational grid for TP3 7.5 in nozzle.

(b) Computational grid for TP3 7.5 in shock region.

### 4.2.2 Inlet conditions

The conditions of the nozzle inlet are taken from Ref. [61]. In these simulations, the conditions at the inlet are applied as non-uniform profiles. Some studies have shown that different inlet profiles better represent the arc-jet flow for specific nozzle configurations. However, in these simulations a uniform profile is applied to all properties. It is expected that this might affect the flow velocity profiles and discharge behavior but not significantly change the sample surface properties, as the flow has had a significant distance to develop regardless of the inlet. The inlet conditions are shown in Table 4.1.

Table 4.1: Simulation Parameters for TP3 7.5 inch Nozzle

Property	Unit	Value
Temperature	[K]	6902
Gas Velocity	[m/s]	383
Chamber Pressure	[Pa]	266
Partial Density [N <sub>2</sub> ]	[%]	$2.67 \times 10^{-2}$
Partial Density [O <sub>2</sub> ]	[%]	$1.0 \times 10^{-6}$
Partial Density [NO]	[%]	$2.0 \times 10^{-4}$
Partial Density [N]	[%]	$1.55 \times 10^{-2}$
Partial Density [O]	[%]	$1.26 \times 10^{-2}$

### 4.2.3 Results

The Mach number contours are compared between KATS and DPLR, and shown in Fig. 4.3. Here, the top half of the contour is computed in KATS and the bottom is from DPLR. This comparison shows good agreement in regards to shock stand-off distance, and the post-shock region. The flow inside the nozzle is also in good agreement. However, the flow expansion varies slightly between the two simulations, as well as the area upwind of the shock. It is expected that this is correlated to the vacuum chamber pressure being unknown in the KATS simulation. Other reasons may be due to different grids, and underlying differences between the numerical schemes,

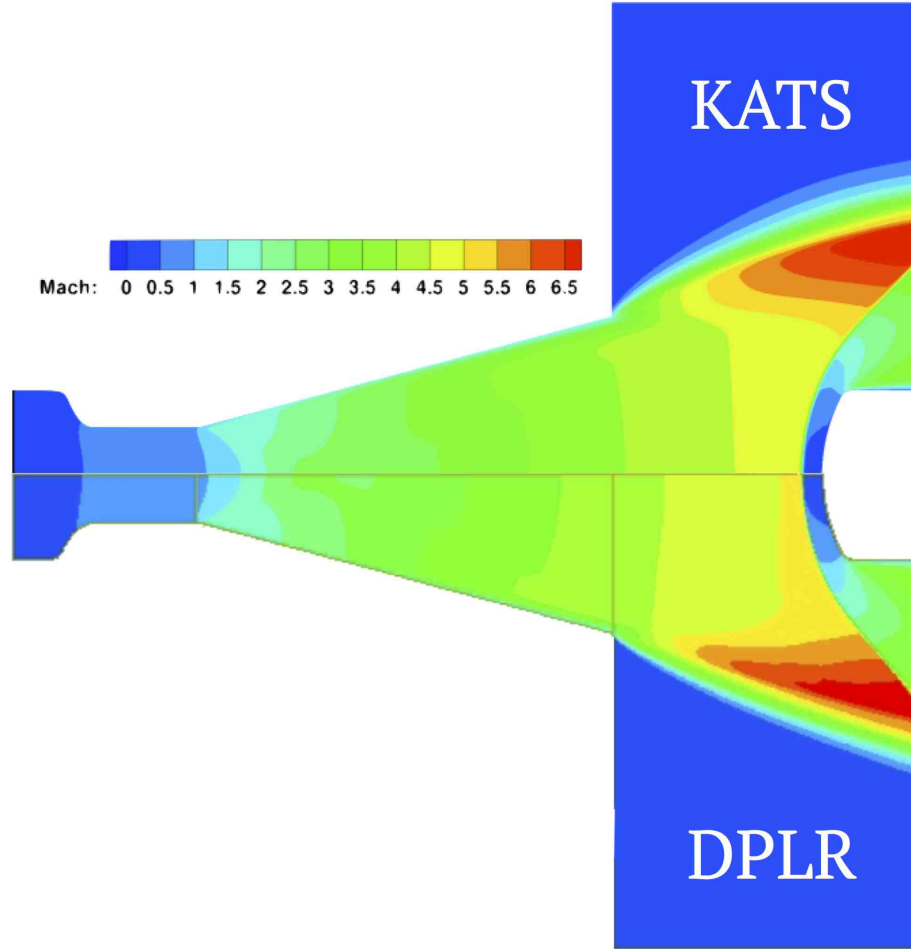
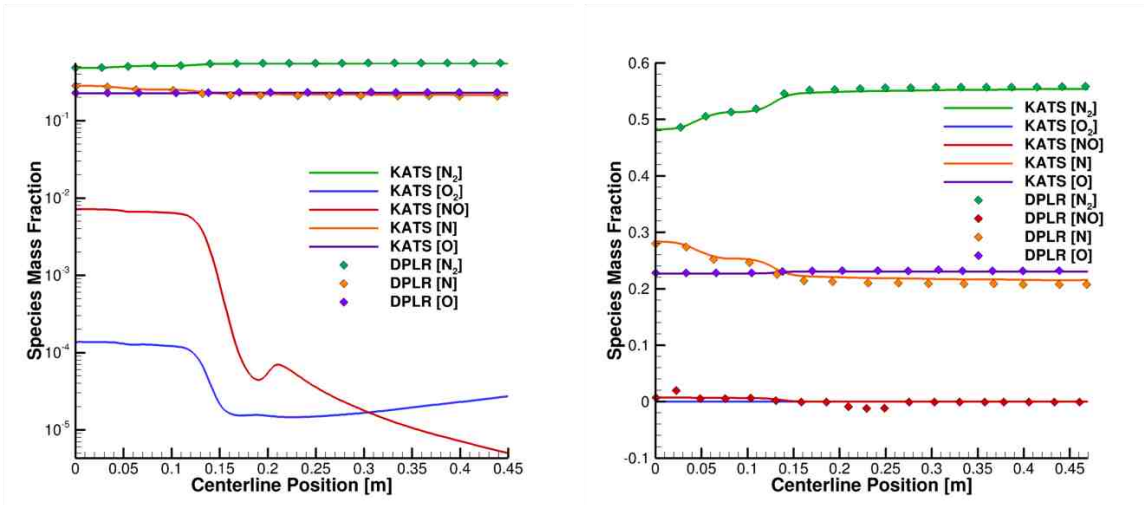


Figure 4.3: Mach number contour comparison between KATS and DPLR.

and that the inlet profile in KATS was uniform while DPLR used a parabolic shape.

Figure 4.4 shows the agreement between the predictions from each code with regards to the species mass fraction. As the predictions match well, it can be concluded that the chemical models implemented in KATS are correct and that this component of the code is verified. The species of low mass fraction ( $\text{NO}$  and  $\text{O}_2$ ) cannot be verified with this problem because the computational data was obtained from the literature and the resolution is too low to compare these on the log scale.

Figure 4.5 shows the comparison between the centerline temperature inside the nozzle. This nozzle is particular because there is a mixing zone downstream of the throat which can be observed on the plot as the bump. Both KATS and DPLR



(a) Species in logarithmic scale.

(b) Species in linear scale.

Figure 4.4: Nozzle centerline species mass fraction comparison between KATS and DPLR.

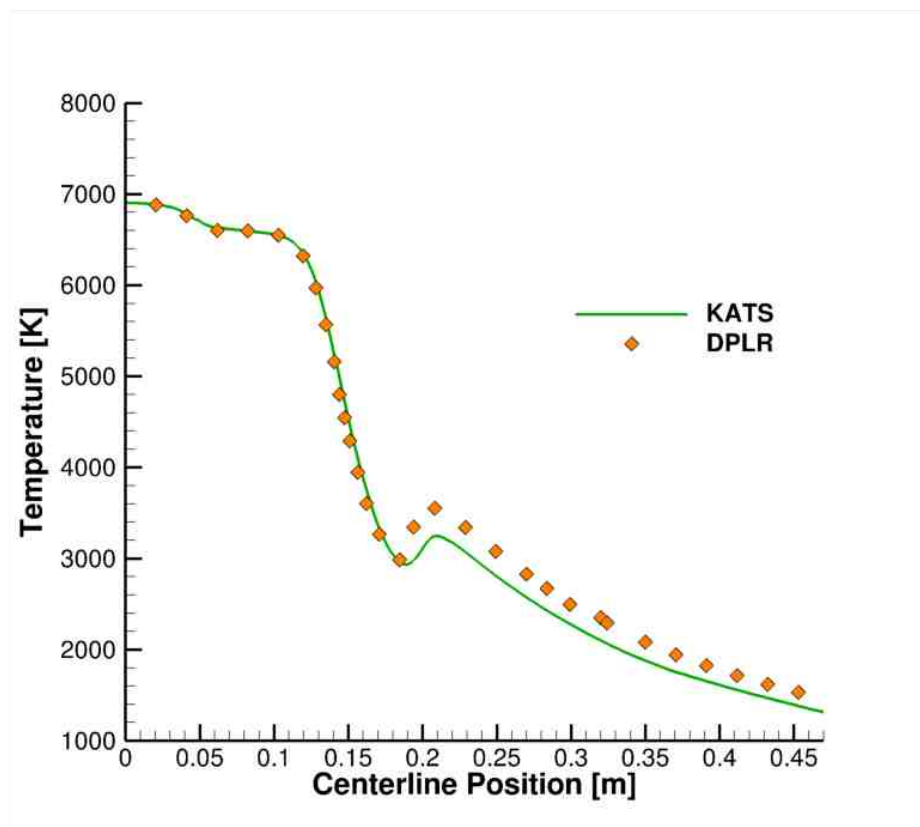
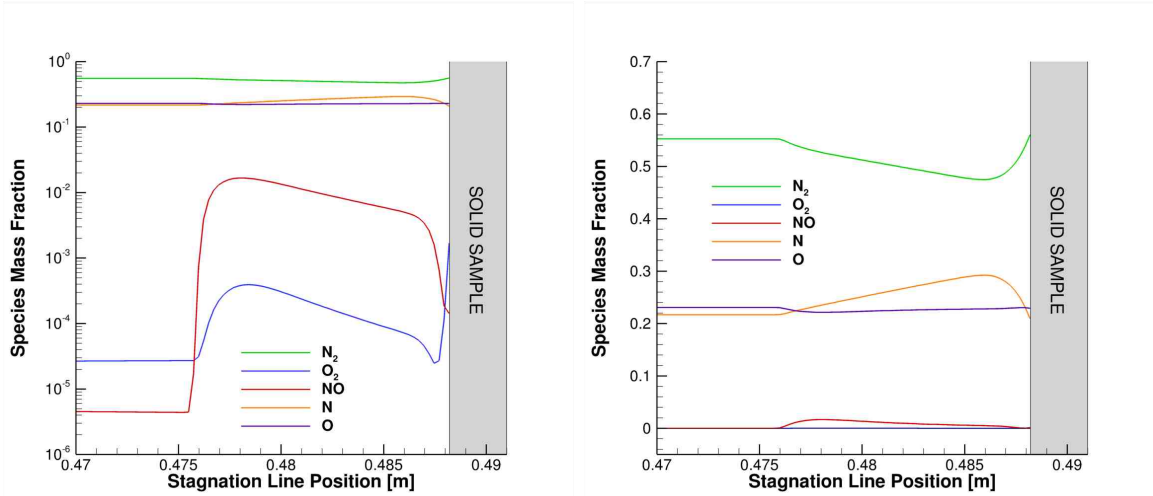


Figure 4.5: Nozzle centerline temperature comparison between KATS and DPLR.

capture this phenomenon, although KATS slightly under-predicts the temperature in this region and downstream.



(a) Post-shock region species mass fraction simulated with KATS in logarithmic scale. (b) Post-shock region species mass fraction simulated with KATS.

Figure 4.6: Post-shock region species mass fraction simulated with KATS.

The temperature in the post-shock region is shown in Fig. 4.7. It is shown that there is good agreement between the codes. The shock itself (denoted by the straight, vertical line) matches exactly between both codes. The temperature near the surface of the sample is also in good agreement. However, there is a discrepancy between the temperature profiles in the post-shock region. This may be due to a difference in the vibrational temperature. Finally, the chemical composition in the post-shock region is presented in Fig. 4.6. The DPLR results are not compared because the boundary conditions used at the sample surface are different. For this simulation, KATS uses a non-catalytic surface boundary condition. This changes the species composition significantly [64] since a super-catalytic boundary condition promotes species recombination to the degree of the inlet conditions. In this instance, DPLR used a fully-catalytic boundary condition at the sample surface therefore promoting species complete recombination. It should be noted that this boundary condition also significantly affects the resulting heat flux on the surface.

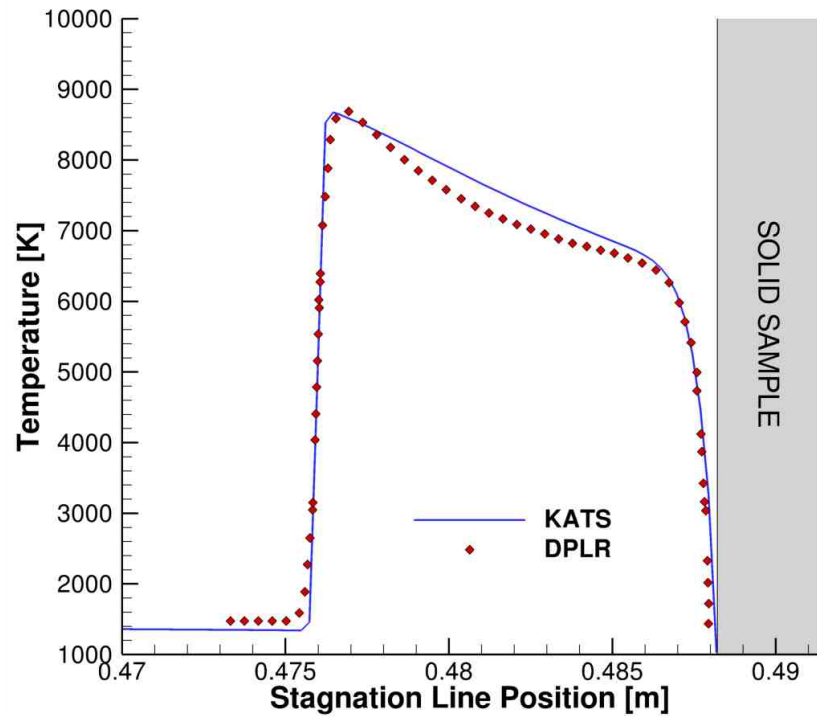


Figure 4.7: Post-shock region temperature comparison between KATS and DPLR.

### 4.3 HYMETs Mach 5 nozzle

While the previous section aimed to validate KATS-FD by comparing to a heritage code, the following section aims to assess the performance of KATS when comparing to experimental measurements taken at the HYMETs facility at NASA Langley Research Center [65]. The details of the testing campaign can be found in Inman, et al. [8].

#### 4.3.1 Geometry

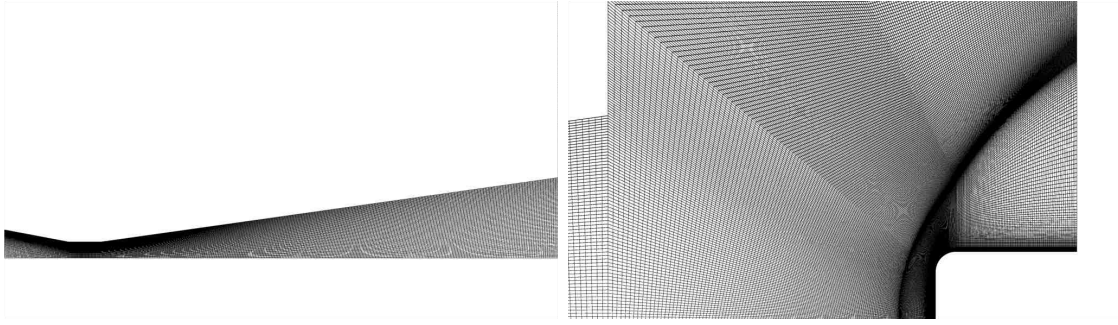
The geometry is a Mach 5 converging/diverging nozzle, with a 12.7 mm throat diameter, and a 63.5 mm exit diameter, whose detailed engineering drawing is found in Appendix 2. A silica-carbide, 25 mm diameter, flat-faced sample is placed 50.8 mm downstream of the nozzle exit. The computational domain is shown in Figs. 4.8a



Table 4.2: Simulation Parameters for Test Case 1

Gas Composition	Bulk Enthalpy [MJ/kg]	Mass Flow Rate [slpm]	Arc Pressure [kPa]
Air add Ar	6.5	400	109

and 4.8b.



(a) HYMETS Mach 5 nozzle computational domain. (b) HYMETS vacuum chamber computational domain.

### 4.3.2 Test conditions

Planar Laser Induced Fluorescence (PLIF) measurements were taken at several locations downstream of the nozzle exit for measuring flow velocity in the axial and radial directions. A schematic of the experimental set-up is shown in Fig. 4.9. The tests were run at multiple enthalpy and pressure conditions as well as earth and martian atmospheric compositions. From these, one case was selected with the flow conditions shown in Table 4.2.

The gas mixture is composed of 75% Nitrogen ( $N_2$ ), 20% Oxygen ( $O_2$ ) and 5% Argon (Ar) by volume. Molecular Tagging Velocimetry methodology was used to measure the axial velocity while the radial velocity is measured using the Doppler shift technique, and the results are shown in Fig. 4.10.

Based on the bulk enthalpy and the chemical composition, a program was written in Cantera [66] to generate the equilibrium conditions for the inlet. The script was used to calculate the temperature, total density, and mass fractions of each species in

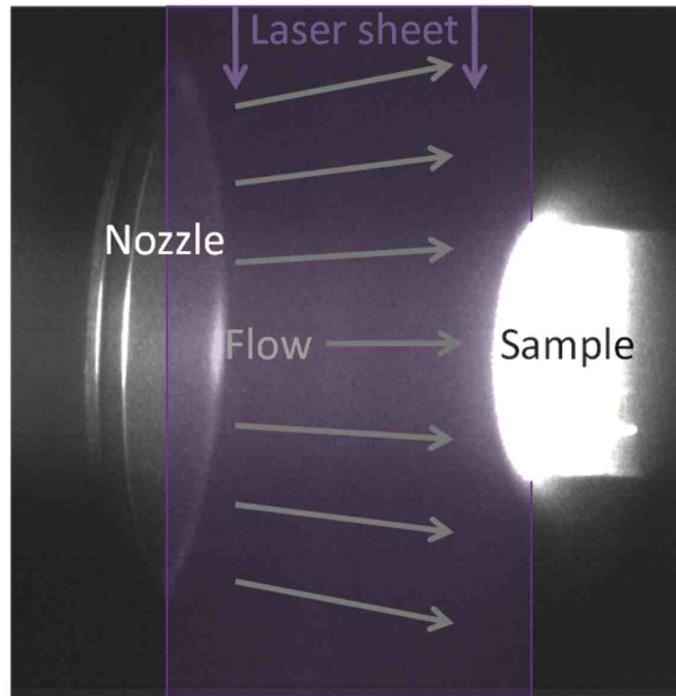


Figure 4.9: PLIF experimental set-up in HYMETs, from Ref. [8].

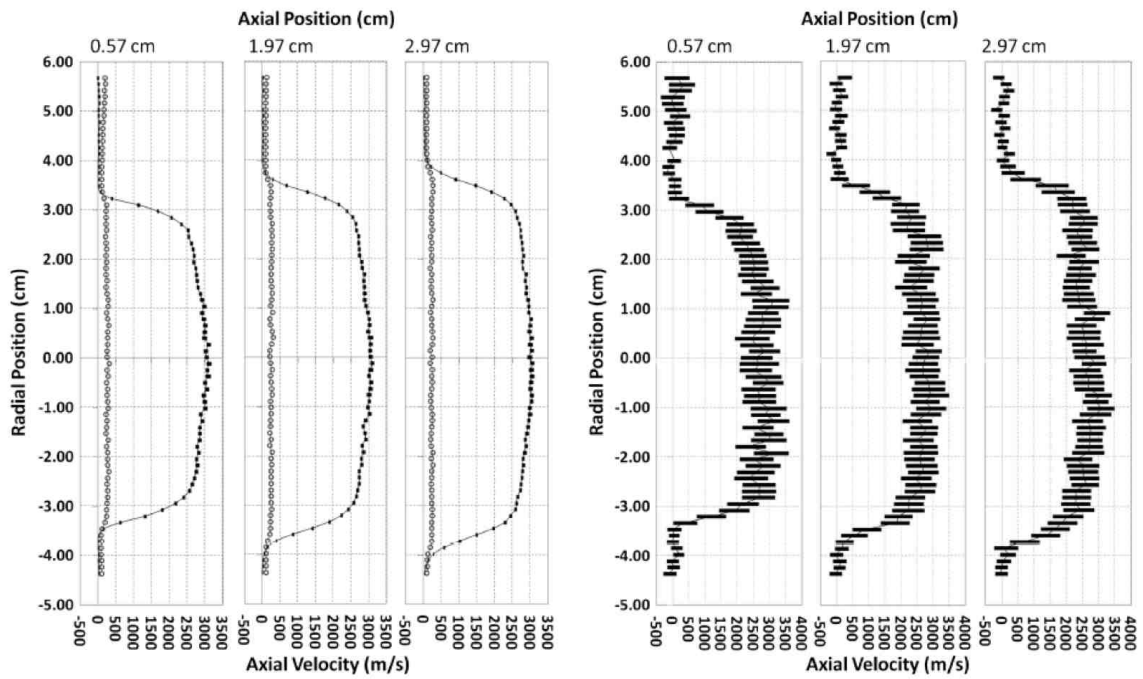


Figure 4.10: Axial Velocity Profiles from Inman et al. [8] using PLIF

Table 4.3: Simulation Parameters for Mach 5 Nozzle Flow

Property		Value
Inlet Temperature*	[K]	3669
Inlet Velocity	[m/s]	372
Chamber Pressure	[Pa]	228
Partial Density of	Ar	$4.65 \times 10^{-3}$
	N <sub>2</sub>	$6.97 \times 10^{-2}$
	O <sub>2</sub>	$1.86 \times 10^{-2}$
	NO	$1 \times 10^{-30}$
	N	$1 \times 10^{-30}$
	O	$1 \times 10^{-30}$
Cold Wall Temperature*	[K]	350

\*Translational-Rotational and Vibrational-Electronic

the mixture. Once the total density of the mixture was known, the partial density of each species was determined and used as an input parameter for the CFD simulation. The inlet velocity was computed from the mass flow rate and density of the mixture as well as the inlet area. Input parameters are as shown in Table 4.3.

### 4.3.3 Results

The Mach number and axial velocity contour for the Mach 5 nozzle is shown in Fig. 4.11 and Fig. 4.12, respectively. One important aspect to note is that the simulation does achieve Mach number  $\approx 5$ , which provides confidence in the results. One can observe in from these contours the difficulties of simulating axisymmetric geometries with a finite-volume framework from the values at the centerline. This is expected because finite-volume framework compute fluxes through faces and an axisymmetric geometry does not contain a face at the centerline. This means that the symmetry boundary conditions is not being applied on an area but one line. This is known to cause small discrepancies however, they are not expected to significantly change predictions in any location but the centerline. This is also observed in Fig. 4.17 at the stagnation point.

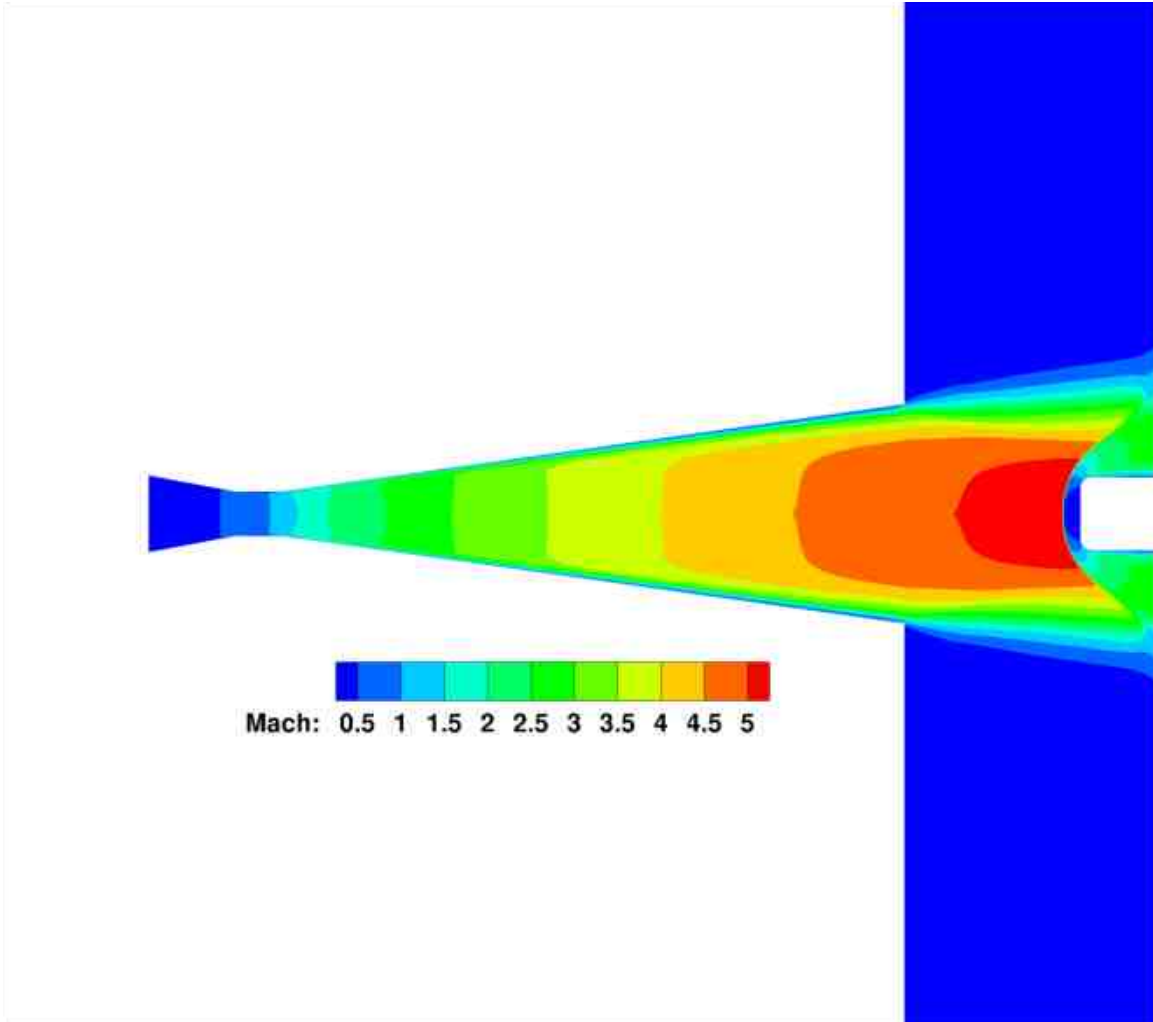


Figure 4.11: Mach number contour simulated with KATS.

It is widely known that it is difficult to assess the enthalpy in ground testing facilities. The uncertainty in this parameter is generally from 10% to 15%. It is of interest to understand what the effect of changing the enthalpy in the simulation is on the axial velocity, which is compared with the experiments. As a computational experiment, the simulations were run at  $6.5 \pm 2.5$  MJ, this is a  $\approx 38\%$  difference. The results show that this only translates to a  $\approx 8\%$  difference in the magnitude of the axial velocity. Further numerical experiments were conducted to understand the effect of the nozzle wall boundary condition and the geometry of the exit. These are described in detail in Ref. [65].

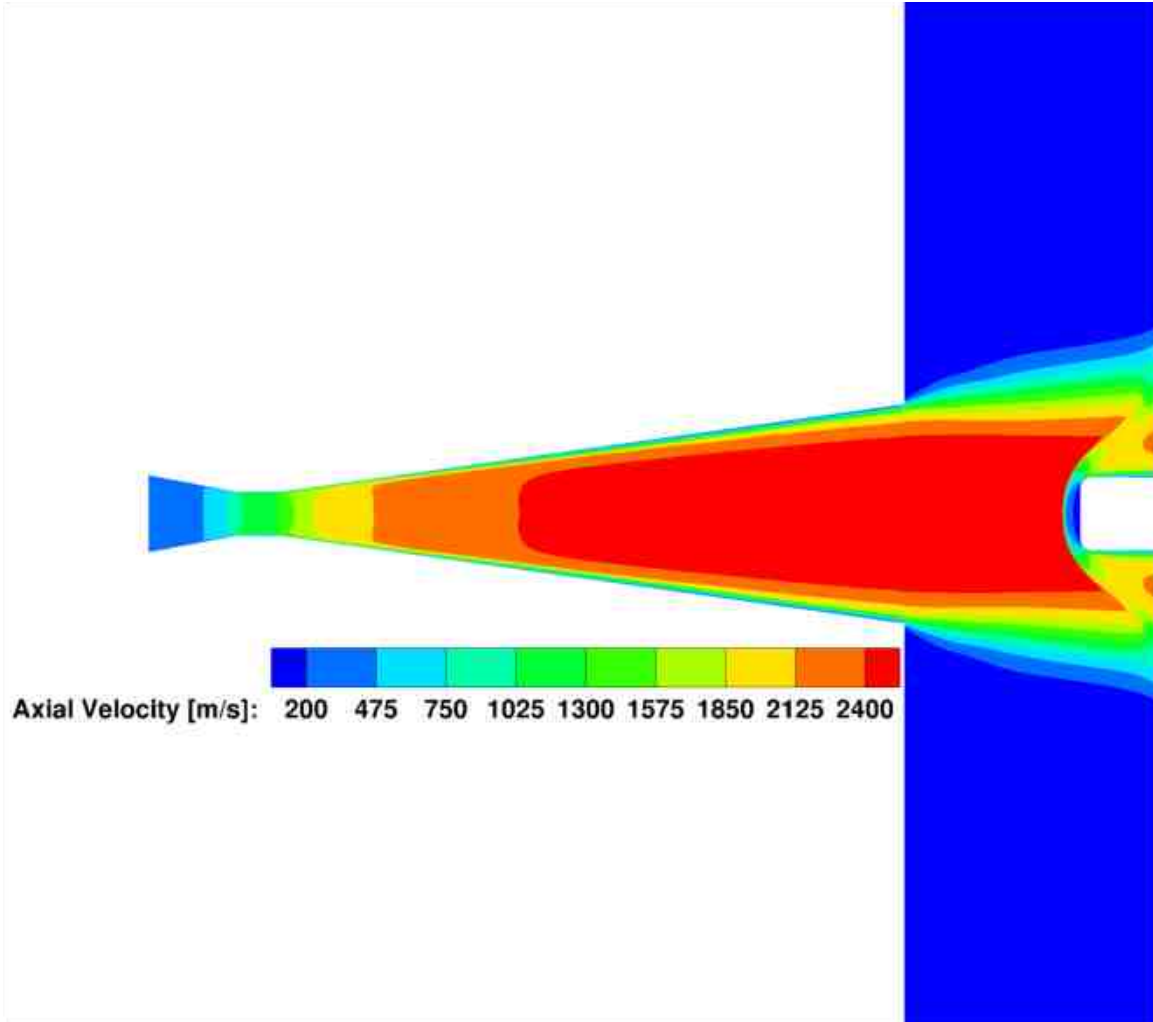


Figure 4.12: Axial velocity contour simulated with KATS.

The experimental data was derived from Fig. 4.10, where the inner and outer bounds of the measurements are used for the shaded area. The comparison between KATS simulated axial velocity and the measurements, at 0.57 cm, 1.97 cm and 2.97 cm downstream of the nozzle is shown in Figs. 4.13, 4.14 and 4.15. These results show good agreement with the experimental data because the velocity of the 6.5 MJ enthalpy case falls in the center of the experimental range. Furthermore, the computational velocity profiles take on a similar shape as the experimental ones.

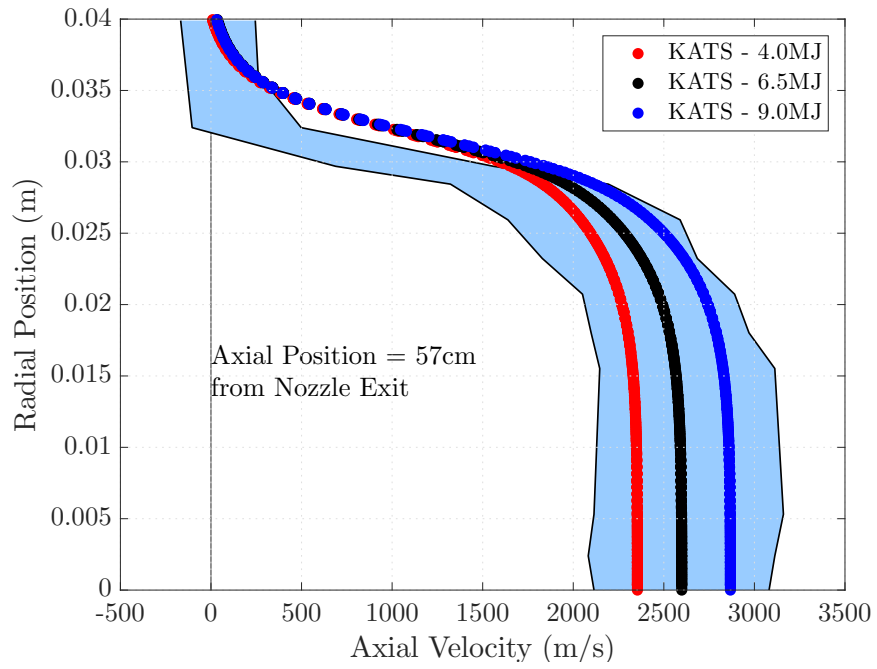


Figure 4.13: Axial velocity comparison between KATS and PLIF, at  $x = 0.57$  cm downstream of the nozzle.

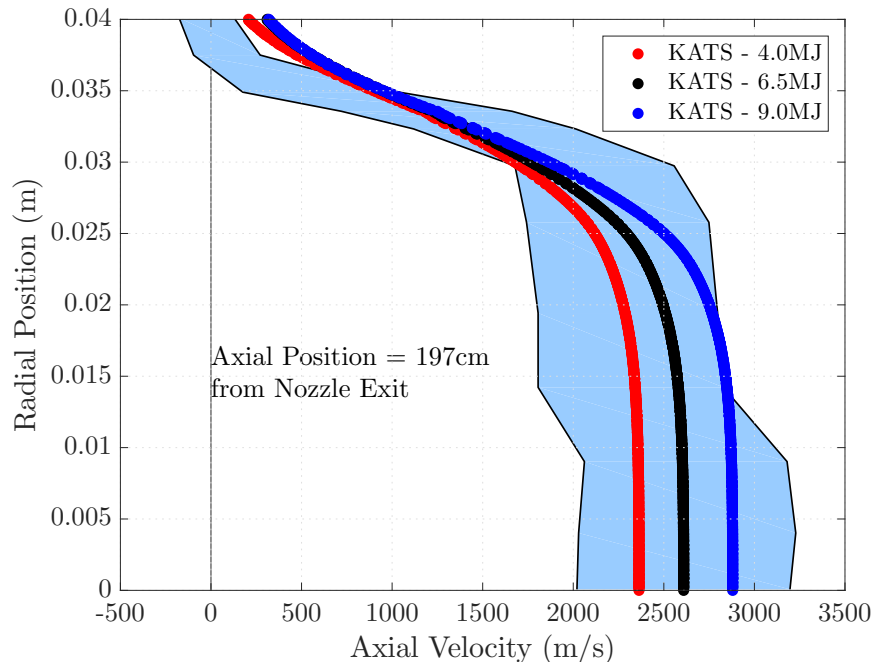


Figure 4.14: Axial velocity comparison between KATS and PLIF, at  $x = 1.97$  cm downstream of the nozzle.

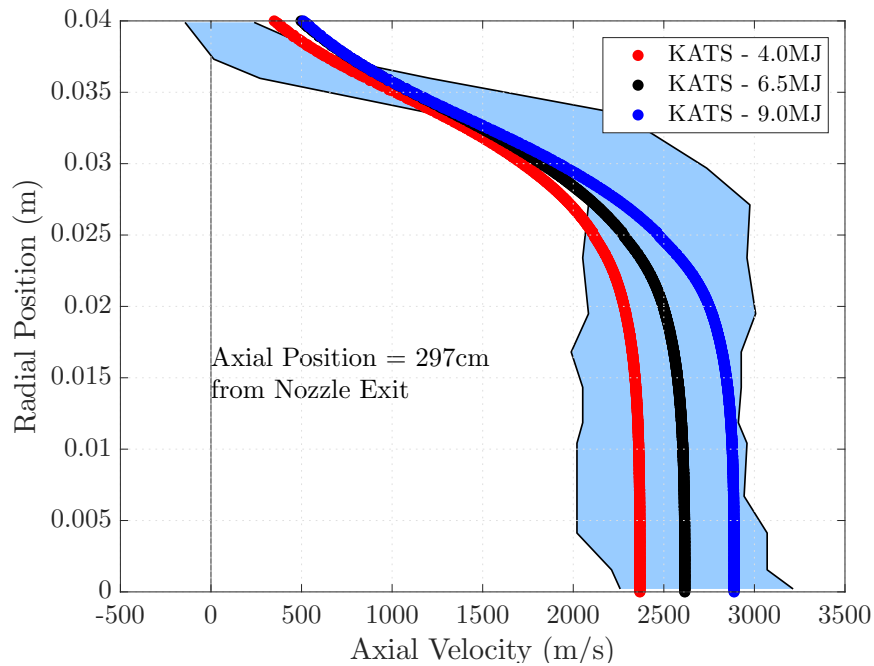
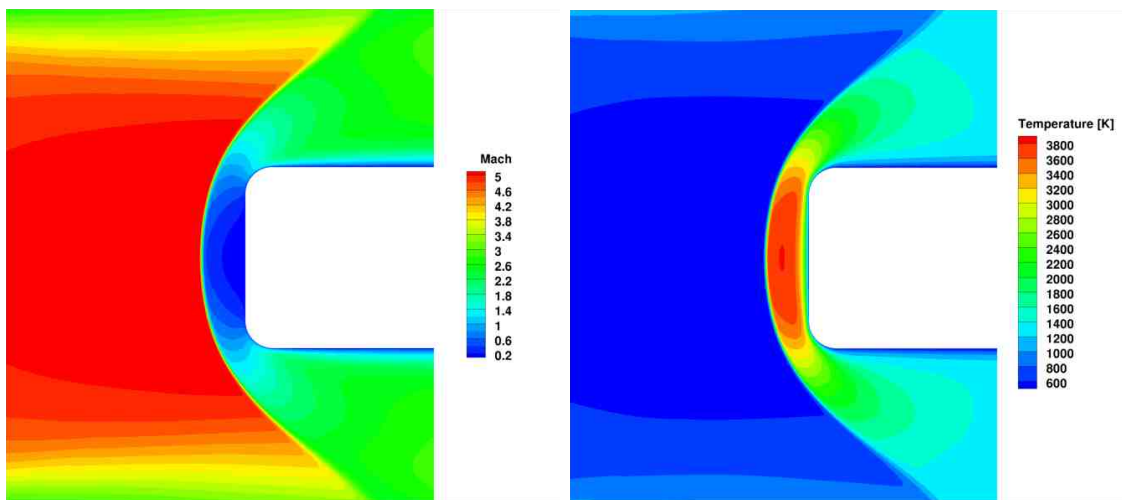


Figure 4.15: Axial velocity comparison between KATS and PLIF, at  $x = 2.97$  cm downstream of the nozzle.

The shock and boundary layer region are shown in Figs. 4.16a and 4.16b. These predictions can be used in future material response simulations for this facility. It can also be noted that the shock is well resolved; a result of multiple shock aligning exercises.



(a) Mach number of boundary layer region simulated with KATS. (b) Temperature of boundary layer region simulated with KATS.

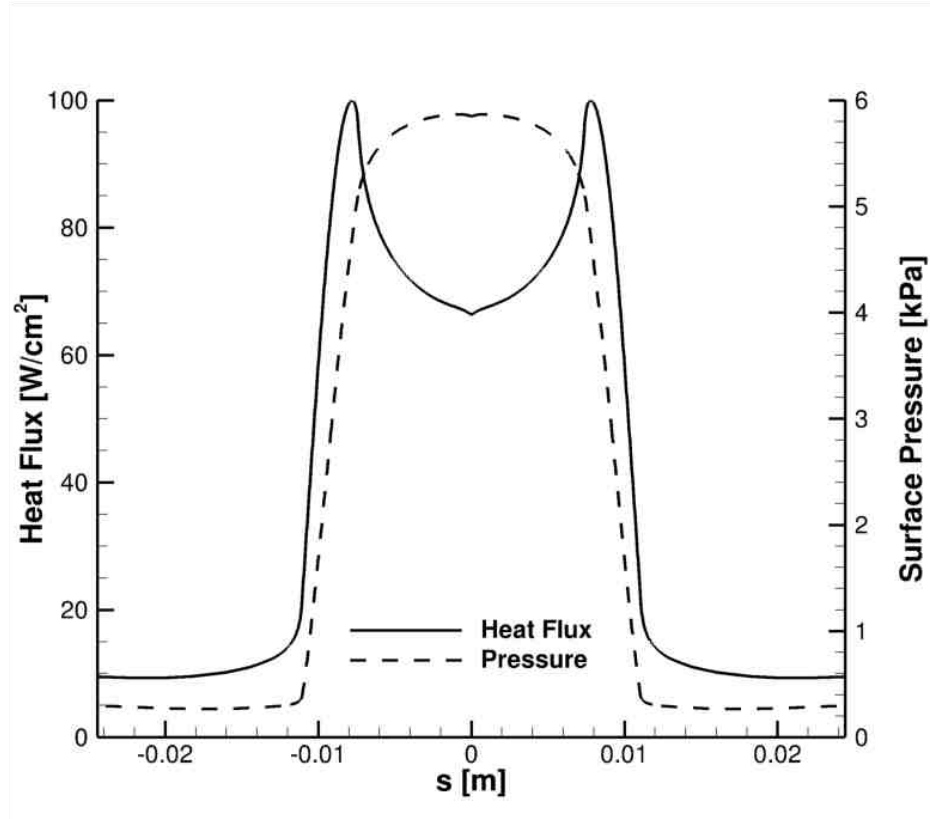


Figure 4.17: Sample surface properties as predicted with KATS.

Finally, if this computational exercise is to be used for material response simulations, it will be necessary to know the surface heat flux and pressure on the sample. These are also computed and shown in Fig. 4.17. Although there was no published data on this particular test run, these predictions appear to be reasonable values for the test parameters, particularly because the profile shape follows the known profile of a flat-faced sample. It is also worth noting that the boundary condition on the sample wall is non-catalytic, which will affect the total heat flux and chemical composition near the surface. Future work may include a comparison between these surface properties and experimental results.



# Chapter 5: Material Response Validation

## 5.1 PICA material model

Due to ITAR restrictions, the PICA material model is not described in this section, however the methodologies to generate the model are presented [67].

KATS contains two options for generating  $B'$  values: in-situ, and through tables. Both of these rely on the external library, MUTATION++ [68]. The in-situ solver requires more computational time as MUTATION++ is called at every time step to solve for the equilibrium state and then compute  $B'$  values for surface chemistry. The more species that are added to the “available” species in the mixture, the longer the computational time. Furthermore, there has been no shown change in the resulting predictions from using one method or the other. In this work, the thermochemistry data is generated into tables, read in by KATS, and interpolated when necessary. A python script is developed for generating both  $B'$  and pyrolysis gas tables for specified user inputs of pressure, temperature, and mixture composition. The script runs MUTATION++ and then post-processes the data into a KATS readable format.

One thing to note is that the  $B'$  tables vary significantly depending on which thermochemical database is used [69, 70]. Many legacy codes use tables that were generated using the JANAF database. These simulations used the CEA database.

## 5.2 Arc-jet environments

One comprehensive arc-jet study was performed by Milos and Chen at NASA Ames Research Center (ARC) [71]. The objective of the experiment was to collect material data on Phenolic Impregnated Carbon Ablator (PICA) over a wide range of aerothermal conditions. The tests were performed at three different facilities: Aerodynamic

Heating Facility (AHF), Interaction Heating Facility (IHF), and the TP2 facility at NASA Johnson Space Center (JSC).

### 5.2.1 Boundary conditions

The surface energy balance [72] equation commonly used for ablation problems is formulated as

$$\dot{q}_{cond} = \underbrace{-\rho_e u_e C_H (h_r - h_w)}_{\text{Aeroconvection}} + \underbrace{\dot{m}_w h_w}_{\text{Energy from wall mass convection}} - \underbrace{\dot{m}_c h_c}_{\text{Energy of char}} - \underbrace{\dot{m}_g h_g}_{\text{Energy of pyrolysis gas}} + \underbrace{\sigma \epsilon (T_w^4 - T_\infty^4)}_{\text{Re-radiation}}. \quad (5.1)$$

For problems where the surface recession is unknown, the environment parameters which are passed to the material response code as boundary conditions are the aeroconvection heat flux and the radiative heat flux. The energy loss due to pyrolysis gas ejection is calculated numerically where the mass convection at the wall, and energy associated with char are obtained through  $B'$  tables. The re-radiative heat flux is a function of the wall temperature and the thermal properties of the material, i.e. emissivity. This means that the parameters from the arc-jet which must be determined are the heat transfer coefficient ( $\rho_e u_e C_H$ ), the recovery enthalpy ( $h_r$ ) and the wall enthalpy ( $h_w$ ) which is determined using  $B'$  tables. The heat transfer coefficient is unknown, however, the total heat flux on the surface is measured.

This means that

$$\dot{q}_{aero} = \rho_e u_e C_H (h_r - h_w) \quad (5.2)$$

where  $\dot{q}_{aero}$  is the measured heat flux. The recovery enthalpy is a known parameter from the arc-jet, the wall enthalpy is the enthalpy of the flow at the wall, usually calculated with CFD, so the heat transfer coefficient can be determined by

$$\rho_e u_e C_H = \frac{\dot{q}_{aero}}{h_r - h_w}. \quad (5.3)$$

### 5.2.2 Blowing reduction

In order to account for the thickening of the boundary layer due to mass injection from the surface a commonly used blowing reduction parameter is applied to the heat transfer coefficient. This attenuates heating, and a detailed derivations can be found in Ref. [73]. The modified aeroheating flux is given by

$$\dot{q}_{aero} = \rho_e u_e C_{h0} \frac{C_h}{C_{h0}} (h_r - h_w) \quad (5.4)$$

where

$$\frac{C_h}{C_{h0}} = \begin{cases} 1 - \frac{\Phi}{2} + \frac{\Phi^2}{12}, & \text{for } \Phi < 10^{-7} \\ \frac{\Phi}{e^{\Phi}-1}, & \text{for } 10^{-7} \leq \Phi \leq 20 \\ \Phi e^{-\Phi}, & \text{for } 20 < \Phi \leq 100 \\ 10^{-8}, & \text{for } \Phi > 100. \end{cases} \quad (5.5)$$

The blowing correction is accommodated for whether the flow is laminar or turbulent by the blowing reduction parameter,  $\lambda$ , which is

$$\lambda = \begin{cases} 0.5, & \text{for laminar flow} \\ 0.4, & \text{for turbulent flow.} \end{cases} \quad (5.6)$$

For arc-jet environments, the flow is generally assumed to be laminar in the boundary layer, and this a value of  $\lambda = 0.5$  is used.

### 5.3 Test parameters

Seven test cases are selected for their encompassing range of heat fluxes, pressure and total Argon injection. The heat fluxes ranged from 107 W/cm<sup>2</sup> to 1100W/cm<sup>2</sup> with corresponding pressures at 2.3 kPa to 84 kPa. It is important to simulate extreme environments as well as moderate ones. In some instances, the interaction between phenomena, even if at moderate levels, can supersede the end result of more

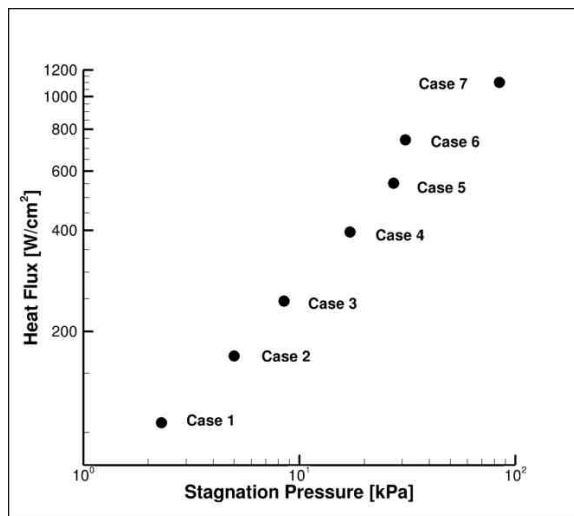


Figure 5.1: Heat flux and pressure of the seven test cases.

Table 5.1: Simulation parameters for array of test cases

Case	%Ar []	Heat Flux [W/cm <sup>2</sup> ]	Enthalpy [MJ/kg]	Pressure [kPa]	Time [s]
1	0.276	107	15.9	2.3	55
2	0.142	169	17.8	5.0	33
3	0.108	246	20.0	8.5	42
4	0.080	395	22.8	17.2	34
5	0.080	552	25.3	27.3	30
6	0.080	744	32.0	31.0	27
7	0.146	1102	28.7	84.4	10

extreme environments. A plot of the pressure and heat flux of the different test cases is shown in Fig. 5.1. The geometry of the samples is represented in Fig. 5.2, it is a standard Iso-Q shape, with thermocouples placed in the locations depicted. The table of parameters for each of the cases is shown in Table 5.1.

Measurements were taken for material recession, surface temperatures and in-depth temperatures. The stagnation pressure and heat flux were measured using a combination slug-calorimeter/pitot-pressure device. The temperature was measured with thermocouples. The two thermocouples closest to the surface were R-Type while the rest were K-Type. Furthermore, the surface temperature of the samples is measured using a pyrometer. The uncertainty associated with the pyrometer readings

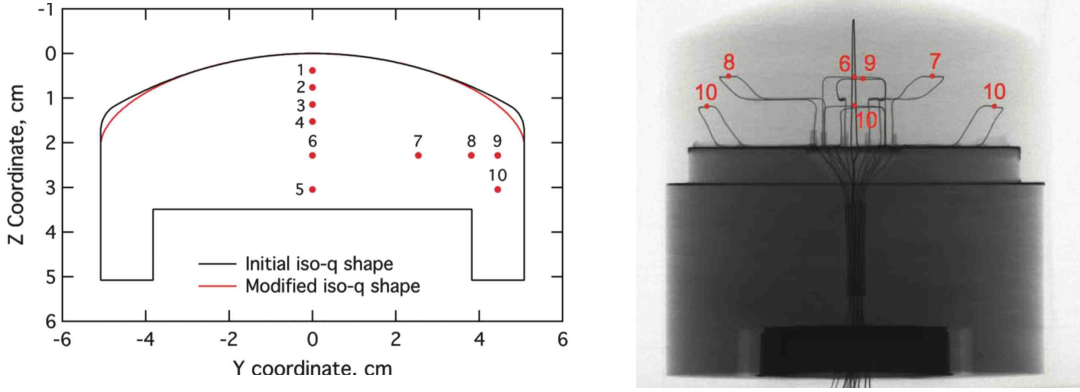
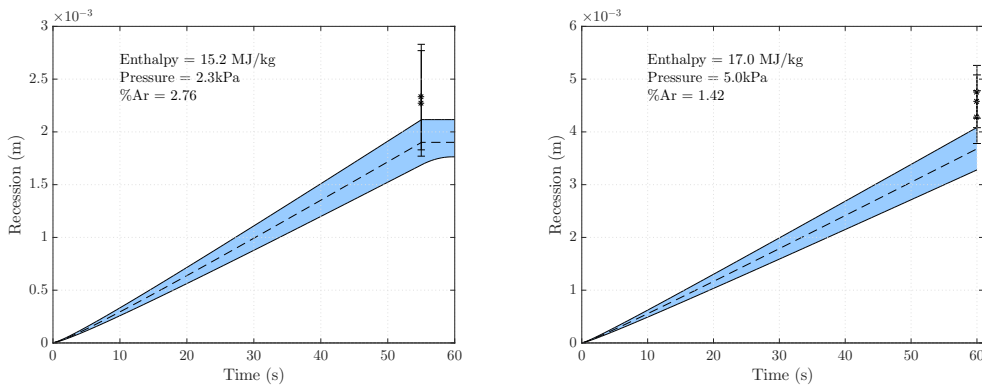


Figure 5.2: Sample thermocouple placement.



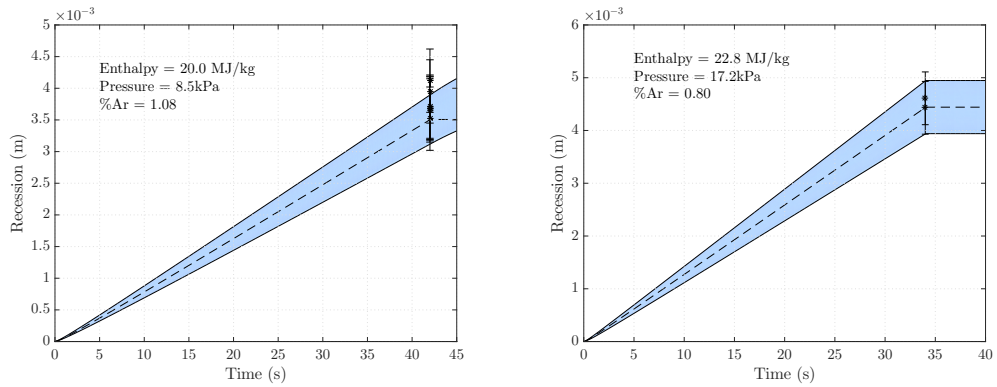
(a) Case 1 - Heat Flux = 107 W/cm<sup>2</sup>, (b) Case 2 - Heat Flux = 169 W/cm<sup>2</sup>,  
 Pressure = 2300 Pa Pressure = 5000 Pa

Figure 5.3: Recession in low heat flux and pressure test cases.

is approximately  $\pm 5\%$ . The heat flux uncertainty varies from facility to facility; in the AHF and IHF, which are relatively well-characterized facilities, this is generally 10% to 15%. To account for this, simulations are run at three different heating levels, per test case i.e. 90%, 100% (nominal), and 110%. Finally, the recession was measured with calipers, whose uncertainty was  $\pm 0.5$  mm.

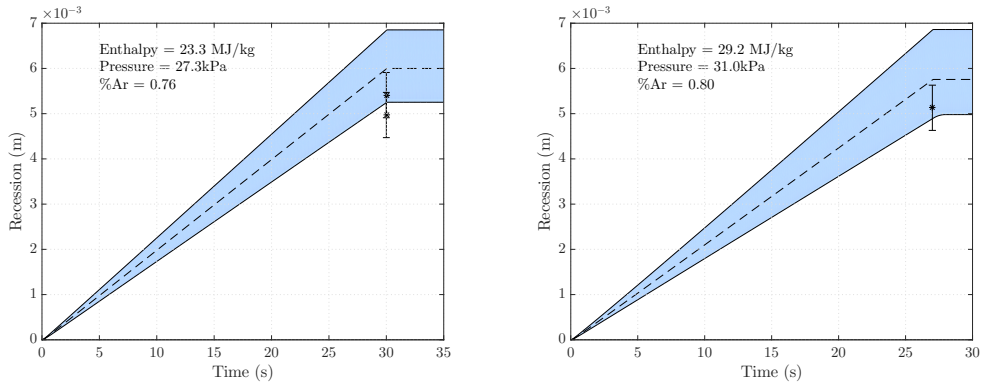
### 5.3.1 Results

It can be determined from these numerical tests that KATS-MR can accurately (within experimental uncertainty) predict the surface recession and surface temperature of the seven PICA samples exposed to arc-jet environments. However, it should



(a) Case 3 - Heat Flux =  $246 \text{ W/cm}^2$ , (b) Case 4 - Heat Flux =  $395 \text{ W/cm}^2$ ,  
 Pressure =  $8500 \text{ Pa}$  Pressure =  $17200 \text{ Pa}$

Figure 5.4: Recession at intermediate heat flux and pressure test cases.



(a) Case 5 - Heat Flux =  $552 \text{ W/cm}^2$ , (b) Case 6 - Heat Flux =  $744 \text{ W/cm}^2$ ,  
 Pressure =  $27300 \text{ Pa}$  Pressure =  $31000 \text{ Pa}$

Figure 5.5: Recession at high heat flux and pressure test cases.

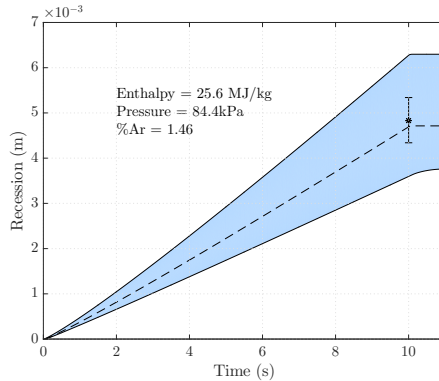
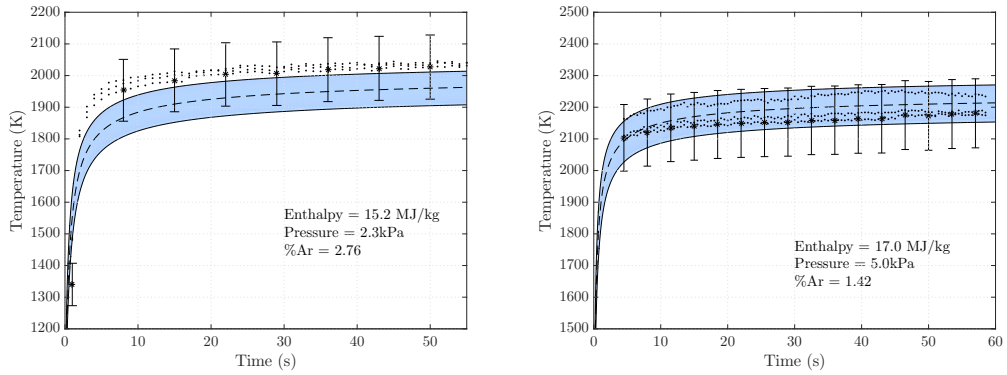
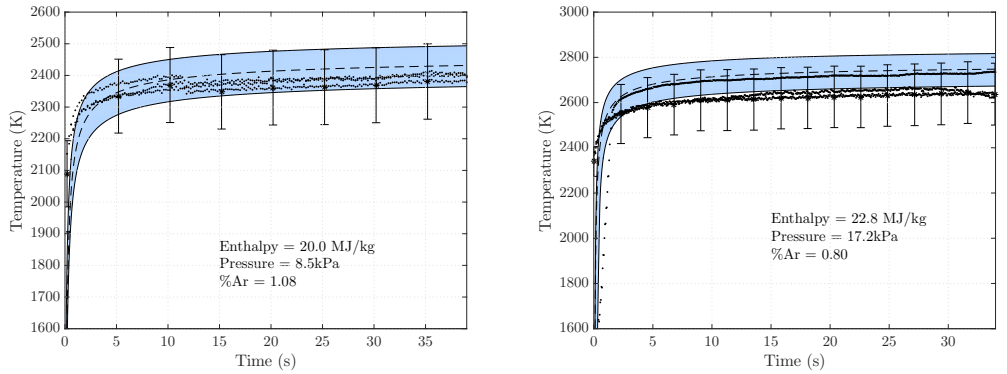


Figure 5.6: Case 7 - Heat Flux =  $1102 \text{ W/cm}^2$ , Pressure =  $31000 \text{ Pa}$



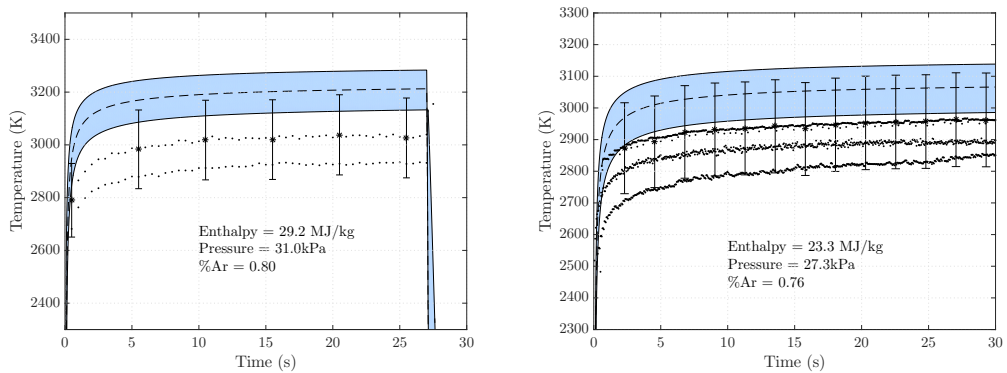
(a) Case 1 - Heat Flux =  $107 \text{ W/cm}^2$ , (b) Case 2 - Heat Flux =  $169 \text{ W/cm}^2$ ,  
Pressure = 2300 Pa Pressure = 5000 Pa

Figure 5.7: Surface temperature in low heat flux and pressure test cases.



(a) Case 3 - Heat Flux =  $246 \text{ W/cm}^2$ , (b) Case 4 - Heat Flux =  $395 \text{ W/cm}^2$ ,  
Pressure = 8500 Pa Pressure = 17200 Pa

Figure 5.8: Surface temperature at intermediate heat flux and pressure test cases.



(a) Case 5 - Heat Flux =  $552 \text{ W/cm}^2$ , (b) Case 6 - Heat Flux =  $744 \text{ W/cm}^2$ ,  
Pressure = 27300 Pa Pressure = 31000 Pa

Figure 5.9: Surface temperature at high heat flux and pressure test cases.

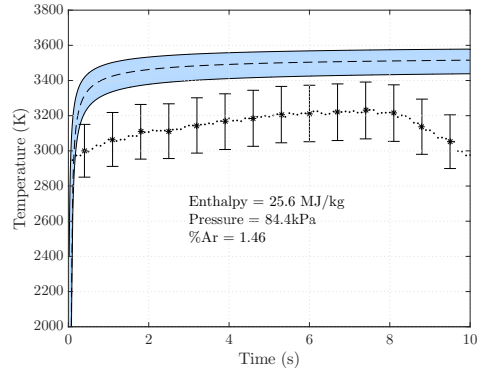


Figure 5.10: Case 7 - Heat Flux =  $1102 \text{ W/cm}^2$ , Pressure =  $31000 \text{ Pa}$

be noted that the experimental uncertainty ( $\approx 10\text{-}15\%$ ) is higher than the ultimate objective of high-fidelity modeling tools; to be within  $5\%$  of the reality. However, observing the surface temperature trends, while KATS accurately predicts the surface temperature at low enthalpy conditions, it overpredicts the latter at higher temperatures. The surface recession behaves in accordance with the overprediction of the temperature i.e. at low heat fluxes, recession is underpredicted while good agreement is achieved at high heat fluxes. This may point to a systematic error in the code, where the recession is always being underpredicted with respect to the temperature. There are several factors that should be considered regarding the simulation:

1. Uncertainties associated with the material model;
2. At more extreme conditions, multi-dimensional effects are shown to be more relevant;
3. Uncertainties with grid-advection scheme;
4. Uncertainty in chemical composition of the gas (i.e. %Ar).

The first item is the most highly influential parameter regarding the heat conduction and therefore temperature of this list. Although this material model is commonly used, there are aspects of the model that are constructed depending on the requirements of the computational framework. For instance, because of the complexities of



the momentum conservation equations solved in KATS, some pyrolysis gas parameters are required in addition to those required by most material response codes. These parameters are generated with MUTATION++ but may not agree with traditional models if empirical data is used. The second point refers to the importance of multi-dimensionality in extreme environments. This is because at higher pressure and heat flux the pyrolysis gas transport is expected to behave in more complex manners, for instance, inertial effects may no longer be negligible. With regards to the third item, although the grid advection scheme has been verified, this is the first set of problems to utilize this scheme in a real-world scenario. Whereas the verification problems were intended to verify individual functionalities of the mesh motion algorithm, there could be inaccuracies with the interaction of these functionalities. Finally, in some computational experiments have shown that the Argon content in the boundary layer is significantly influential in the construction of  $B'$  tables and subsequently the energy exchange at the surface. Despite these remarks, the material response module has been shown to accurately predict surface temperature and recession, within instrument uncertainty, in a complex arc-jet environment, with a real and complex TPS material.

# Chapter 6: Gas Transport in Porous Media

## 6.1 Motivation

The question of how best to model pyrolysis gas transport has been a long-standing question in the ablation community. Heritage codes such as CMA and FIAT do not solve the gas continuity equation, instead the mass flux through the surface is computed as a function of the decomposition rate of the solid species into gas. This way, the gas is produced and “instantaneously” transported to the surface to contribute to the overall surface energy and mass balance. The solid density at any given point in the domain is modeled as a function of the mixture of the two main components present in the organic resin, and the reinforcing material, by

$$\rho_s = (1 - \phi) [\Gamma(\rho_A + \rho_B) + (1 - \Gamma)\rho_C] \quad (6.1)$$

where  $A$ ,  $B$ , and  $C$  are the two organic resin components and the reinforcing material, respectively. The rate of change of solid density, in other words, the rate of decomposition, is given by the Arrhenius rate of reaction:

$$\frac{\partial}{\partial t} \left( \frac{\rho_i - \rho_{ci}}{\rho_{vi}} \right) = -A_i \left( \frac{\rho_i - \rho_{ci}}{\rho_{vi}} \right)^{\Phi_i} \exp(-E_i/RT) \quad (6.2)$$

here  $i$ ,  $vi$ , and  $ci$ , are the component and that component’s respective virgin and char states. Finally, the pyrolysis gas flux is given by

$$\dot{m}_g = \int_{\eta_0}^{\eta} \left( \frac{\partial \rho_s}{\partial t} \right) d\eta \quad (6.3)$$

which is then fed into the surface energy balance.

More recent codes such as CHAR and PATO employ Darcy’s Law to solve for the gas velocity in the gas continuity equation [74]. In this way, the gas transport is

only a function of the gas properties and the pressure gradient across the material. Neglecting the flux contributions from the grid convection, the gas continuity equation solved is

$$\frac{\partial(\phi\rho_g)}{\partial t} + \nabla \cdot (\phi\rho_g\mathbf{u}_g) = \dot{\omega} \quad (6.4)$$

where

$$\mathbf{u}_g = -\frac{K}{\mu\phi}\nabla P. \quad (6.5)$$

PATO adds one layer of complexity to this model by accounting for inertial effects of the gas through the addition of a Forchheimer term [75]. This is only expected to be of significance at gas velocities above 50 m/s.

In contrast, KATS-MR solves the conservation of momentum equations to obtain an unsteady form of Darcy’s law,

$$\frac{\partial(\phi\rho_g\mathbf{u}_g)}{\partial t} + \nabla \cdot \left( \frac{\rho_g\mathbf{u}_g\mathbf{u}_g^T}{\phi^2} + P\mathbf{I} \right) - \nabla \cdot \boldsymbol{\tau} = -\frac{\mu}{K}\mathbf{u}_g. \quad (6.6)$$

These equations involve fewer assumptions about the flow and are, most likely, more accurate than Darcy’s Law. However, their implementation is more complex and solving them requires more computational time. The objective of this work was to expand the capability of the KATS-MR code to offer either option to use Darcy’s Law or the momentum equations for resolving the porous flow.

## 6.2 Implementation

### 6.2.1 Governing equations

The Darcy’s Law model required several alterations to the main code. Recall the KATS-MR governing equations from Chapter 2, the equations highlighted in red are

aspects of the code that were removed, i.e. terms related to the momentum equations and terms in green are replaced with Darcy's Law:

$$\mathcal{F}_a = \begin{pmatrix} \phi\rho_g u & \phi\rho_g v & \phi\rho_g w \\ \mathbf{0} \\ \phi\rho_g u^2 + p & \phi\rho_g uv & \phi\rho_g uw \\ \phi\rho_g vu & \phi\rho_g v^2 + p & \phi\rho_g vw \\ \phi\rho_g wu & \phi\rho_g wv & \phi\rho_g w^2 + p \\ \phi\rho_g u h_g & \phi\rho_g v h_g & \phi\rho_g w h_g \end{pmatrix} \quad (6.7)$$

$$\mathcal{F}_d = \begin{pmatrix} \mathbf{0} \\ k \frac{\partial T}{\partial x} & k \frac{\partial T}{\partial y} & k \frac{\partial T}{\partial z} \end{pmatrix} \quad (6.8)$$

$$\mathbf{Q} = \begin{pmatrix} \phi\rho_g \\ \rho_{s1} \\ \dots \\ \rho_{nss} \\ \phi\rho_g u \\ \phi\rho_g v \\ \phi\rho_g w \\ \phi E_g + E_s \end{pmatrix} \quad \mathbf{P} = \begin{pmatrix} p \\ \rho_{s1} \\ \dots \\ \rho_{nss} \\ u \\ v \\ w \\ T \end{pmatrix} \quad \mathbf{S} = \begin{pmatrix} \dot{\omega}_g \\ \dot{\omega}_{s1} \\ \dots \\ \dot{\omega}_{nss} \\ -\phi \frac{\mu}{K} u \\ -\phi \frac{\mu}{K} v \\ -\phi \frac{\mu}{K} w \\ \phi \frac{\mu}{K} (u^2 + v^2 + w^2) \end{pmatrix}$$

Furthermore, the analytical Jacobian matrix,  $\frac{\partial \mathbf{Q}}{\partial \mathbf{P}}$ , requires some alteration. The  $8 \times 8$  sized matrix becomes  $5 \times 5$ , since there are three momentum equations among eight total equations.

### 6.2.2 Time-step stability

In this implementation, the Darcy equation was relatively unstable at large time steps in the beginning of simulations. To prevent numerical difficulties at the beginning of simulations, a Courant-Friedrichs-Lewy (CFL) [76] conditioning function was implemented. The most generic form of this condition, for  $n$ -dimensions, is defined as

$$CFL = \Delta t \frac{u_{x_i}}{\Delta x_i} \leq CFL_{max}. \quad (6.9)$$

In traditional hypersonics problems, the CFL condition acts to prevent the physical speed of the system from surpassing the speed at which information travels inside the system i.e. the speed of sound. Thus, the time-step, based on the CFL condition, is often formulated as

$$\Delta t = CFL_{max} \frac{\Delta x_i}{|u_{x_i} - a|}. \quad (6.10)$$

There is no strict derivation for a CFL condition for Darcy's Law. Thus, for this problem, the condition for stability was formulated as a function of the gas properties,

$$\Delta t = CFL_{max} \frac{\Delta x_i^2}{S_c} \quad (6.11)$$

where the diffusion speed  $S_c$  is defined as a function of the gas properties

$$S_c = \frac{\alpha^2 \rho_g K}{\gamma \phi \mu}, \quad (6.12)$$

note that  $S_c$  is not a speed but is analogous to thermal diffusivity for the heat equation, where the latter represents how fast heat can propagate through a material.

### 6.2.3 First-Order Upwind Scheme

In order to prevent influx of gases i.e. gas from traveling in the wrong direction, a first-order upwinding scheme is implemented [77]. For the momentum equations, the Advection Upstream Splitting Method (AUSM+up) [78] scheme is used, however, a

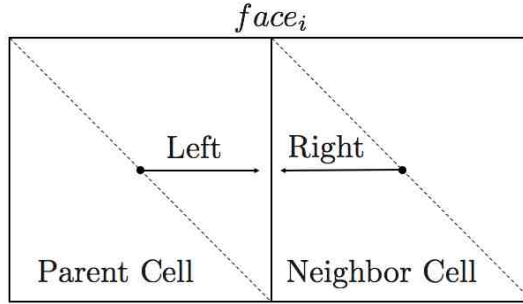


Figure 6.1: Face estimation values with finite-differencing schemes.

simpler model is implemented for the Darcy Flow. This scheme simply guarantees that the discretization of the differencing scheme is determined by the direction in which the information travels, in this case, the direction of the gas velocity. Thus, upon the calculation of the fluxes through each face, the direction of the velocity is first determined. If the direction is positive, the properties used for flux calculation are from the left of the face, if the opposite is true, properties from the right of the face. Here, the left and right are gradient projections of the face values derived from the parent cell or neighbor cell respectively. Thus, for any property  $c$  at face  $i$ ,

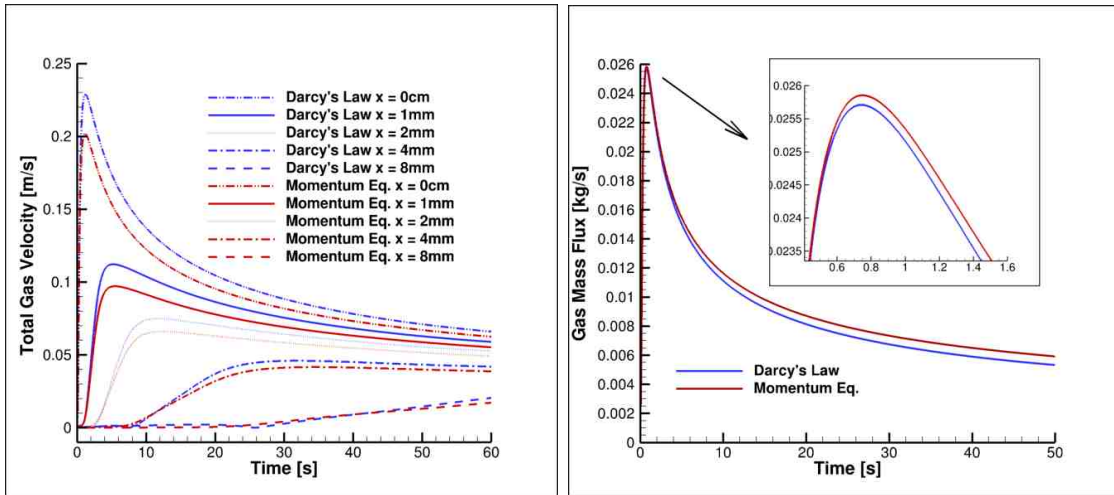
$$c_i = \begin{cases} c_{\text{left},i} & \text{if } (c_{\text{right},i} - c_{\text{left},i}) > 0 \\ c_{\text{right},i} & \text{if } (c_{\text{right},i} - c_{\text{left},i}) < 0 \end{cases} \quad (6.13)$$

### 6.3 Preliminary results

It is of interest to understand how the Darcy model compares with using the momentum equations for studying pyrolysis gas flow. In Section 3, the implementation of Darcy's Law was verified against the analytical solution. In this section, results from the two methods will be presented for a 1-dimensional test case in which a sample of the open-source material TACOT is exposed to an aeroheating environment.

The properties in-depth are compared as a function of time.

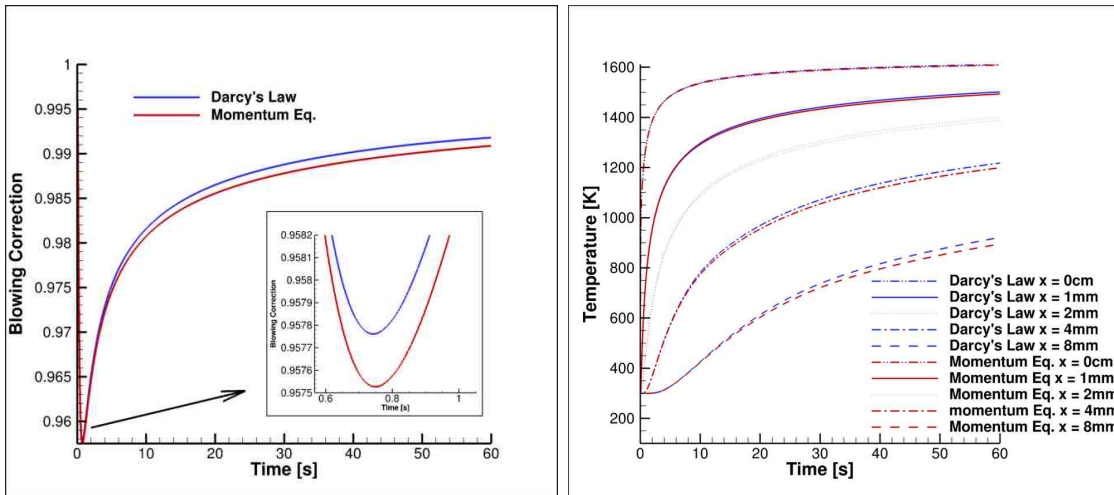
Observing the trends shown, one can conclude that the models differ most signif-



(a) In-depth gas velocity.

(b) Gas mass flux at the surface  $\dot{m}_g$ .

Figure 6.2: Gas flow properties comparison with two porous models.



(a) Blowing correction

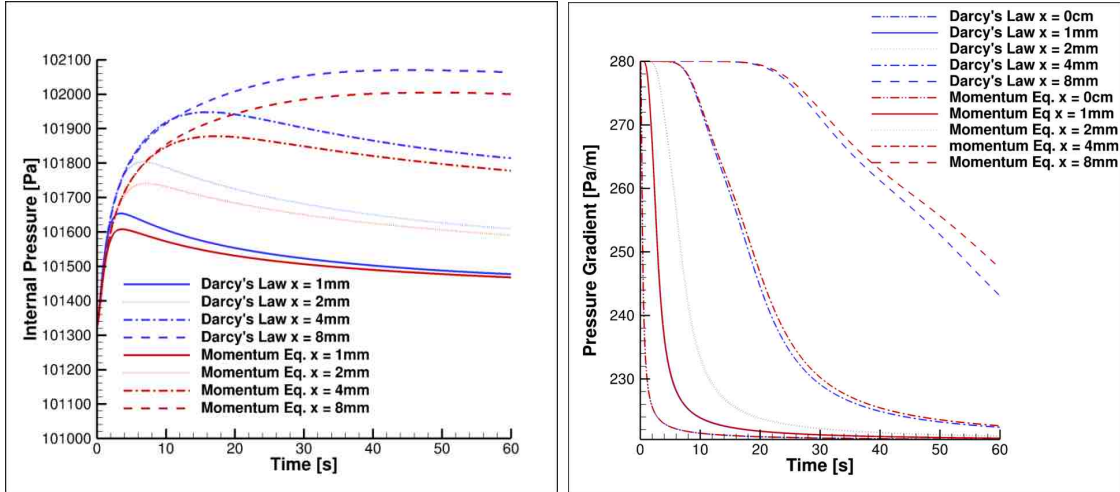
(b) In-depth Temperature

Figure 6.3: Thermal behavior comparison with two porous models.

icantly:

1. in the beginning stage of the simulation, at the surface;
2. after prolonged time, in-depth.

Looking first to Fig. 6.2a, it is shown that in the first 20 seconds of simulation, the surface gas velocity is highest and varies most between models. As time progresses, the two models tend to approach the same velocity. There is little variability between



(a) In-depth pressure.

(b) In-depth pressure gradient.

Figure 6.4: Pressure and pressure gradient comparison with two porous models.

the gas velocity calculated in-depth. It is also shown that Darcy's Law predicts higher gas velocity throughout the entire simulation, both at the surface and in-depth. However, the mass flux through the surface is lower with Darcy's Law. This means that the change due to the gas density or the porosity is more significant than the change in velocity. Further investigation leads to the conclusion that the porosity is changing significantly. This means that the decomposition is being affected significantly by the porous model. This is a non-intuitive idea which should be investigated further. Following the trend of lower gas mass flux from the surface, the blowing correction is higher with Darcy's Law. This means that the heating to the surface will be lowered. This may explain partially why temperature is higher in-depth with Darcy's Law. In Figs. 6.4a and 6.4b it is shown that the highest difference between the models is at  $x = 8$  mm. This correlates to where the pressure gradient is highest for the longest amount of time. As the pyrolysis gas front moves backward the pressure gradient decreases, decreasing the gas velocity as well. The internal pressure follows the same trend. As time evolves the in-depth pressure varies more significantly between the models. Finally, following the previous trends, Fig. 6.3b shows the internal temperature varying most significantly between the models, towards the end of the simulation.



Finally, it should be noted that these conditions are somewhat moderate. The pressure gradients are not very high, which is an indication that this problem may not be pushing the boundaries of either of these models. A test case with more extreme conditions is recommended for future work. Furthermore, it is expected that these observations not be relevant in multi-dimensions. It is also expected that the most significant effect of which porous model is used is most significant in 3-dimensions. Thus, it is recommended that a 3-dimensional comparative case be investigated.

# Chapter 7: Conclusion

## 7.1 Summary

The KATS code, developed at the University of Kentucky, is a high-fidelity modeling family of codes used for simulating various aspects of atmospheric entry problems. Although the code is used extensively for research applications, in order for these to have a significant impact on the community, it must be well verified and validated. This body of work shows the performance of KATS comparatively to analytical solutions, benchmark codes, and experimental data obtained from published literature on arc-jet tests, and highlights the effects of the distinct porous flow models used in KATS comparatively with other codes.

In order to aid developers in their efforts to verify their new implementations, an automated testing tools is developed. This tool is designed for flexibility of use, in that the addition of new tests is made simple. Currently, the testing program contains a variety of analytical solutions described in detail in Chapter 3. The program also includes the option to perform grid convergence tests for each of the analytical problems.

It is shown that KATS-MR is in excellent agreement with all of the analytical solutions designed for testing specific components of the code. These components are each necessary in different scenarios of ablation problems. It is also shown that KATS-MR is second-order accurate in each of the problems.

Once the material response tool is verified, the focus is shifted toward the fluid dynamics module. In order to perform end-to-end simulations of arc-jet facilities, the flow solver must be verified as well. This work describes two main exercises performed with KATS-FD. The first is a verification against a legacy aerothermodynamics code,

DPLR. The AHF, TP3 facility with a 7.5in nozzle is simulated. The nozzle center-line properties are compared with DPLR. These results are in good agreement, which suggests that the method which is used in KATS for simulating high-enthalpy flow facilities is optimal. The properties in the post shock region are also compared, however, there are some differences in the boundary conditions used by DPLR versus KATS. The first is that DPLR uses a super-catalytic boundary condition at the sample wall; this greatly affects the surface heat flux and the species concentration in the boundary layer. The second discrepancy is that the chamber pressure is unknown in the KATS simulation which is shown to have a non-negligible effect by Gokcen et al. [79]. This is suggested to be the reason why the surface pressure does not match between the codes. The second part of the flowfield studies focuses on a comparative study of the Mach 5 nozzle at the HYMETS facility between experimental measurements obtained from the literature and KATS simulations. Axial velocity measurements of the flow discharge from the nozzle were taken using PLIF and compared with those obtained with KATS. It is shown that the solutions from the KATS simulations agree well with the experimental data within the bounds of experimental uncertainty. Some of the unmeasured parameters are highlighted as an example of how simulation tools can be leveraged to help characterize facilities and make predictions of parameters that would otherwise be unknown.

Having the material response as well as the fluid dynamics module of KATS verified provides confidence in the implementation of the models and schemes employed by the codes. The remaining effort is to validate the material response module against experimental data obtained from an arc-jet testing campaign conducted at NASA ARC and JSC. The KATS-MR module is used for simulating one-dimensional samples of PICA, exposed to an arc-jet environment. The amount of surface recession and the surface temperature of the samples is compared with experimental data. These results were positive in that the simulations correctly predicted these parameters within

the bounds of experimental uncertainty. However, it is noted that the code tends to under-predict the surface temperature at low enthalpy conditions and over-predict it at high enthalpies. It is unclear whether this trend is related to the material model or if multi-dimensional effects are too important to be neglected for these types of studies.

In the final chapter of this work, the relevant models for pyrolysis gas transport are explored. An explanation of how Darcy's Law is implemented in the KATS-MR code is presented. The necessary steps to insure stability with this function are demonstrated. Finally, a comparative study is performed where KATS-MR simulates a one-dimensional, fictitious material under an imposed aerodynamic heating environment using the unsteady Darcy equations versus Darcy's Law for gas transport.

## **7.2 Original contributions**

This work overviews the following contributions to the research group and ablation community:

- 1. An automated testing tool is developed for the KATS framework**

It is often difficult for code developers to know if their modifications to the code have caused unwanted problems. A testing tool is designed for ease of use and flexibility to maximize testing efficiency during the development phase. The code can be used for grid-convergence tests and qualitative comparisons. Best-coding practices are utilized and a standard format is employed to enable developers to add their own tests as they implement new models.

- 2. An extensive suite of tests for heat conduction and porous flow problems is prepared**

In addition to the testing tool, a wide range of tests with analytical solutions are set-up. These are ready for use for developers, and range over multiple boundary condition types, models, and features.

**Suggested Future Work:** Although a wide range of tests have been implemented, this is a continuously evolving project which will require updates as the code formatting changes and as the types of problem being solved become more complex in nature.

### 3. **The fluid dynamics module of KATS is verified against a heritage code DPLR**

A 7.5 in nozzle from the TP3 facility at NASA ARC is simulated. The temperature of the flow, as the species concentration through the nozzle is compared with DPLR, and good agreement is achieved.

**Suggested Future Work:** Although the results from these comparisons are positive, there are some aspects in which the code could be improved in order to perform one-to-one comparisons: the implementation of a super-catalytic boundary condition and the implementation of a spatially-varying boundary condition for the inlet properties. These two aspects may have contributed to the discrepancies between the two codes and are used extensively in computational studies of arc-jet environments.

### 4. **The KATS fluid dynamics module is assessed against experimental data from the HYMETs facility**

The Mach 5 nozzle from the HYMETs facility at LaRC is simulated. The parameters are leveraged from an experimental campaign published in Ref. [8]. Flow profile parameters are compared such as axial velocity at different locations downstream of the nozzle exit. Surface properties are computed and shown.

Good agreement with experimental data is achieved and the flow is shown to reach the projected Mach number.

#### 5. **The material response module is validated**

A material model for a common TPS material, PICA, is implemented in the KATS framework. This development allows users to develop surface chemistry databases with their own boundary layer mixture. This is advantageous for any future parametric studies.

Seven test cases are leveraged from the literature, Ref. [71], ranging over various enthalpies and pressures, and these are simulated with KATS. This tests the code's ability to simulate real world materials in a complex aerothermal environment.

**Suggested Future Work:** The framework is established for parametric studies in arc-jet environments. However, it is of interest to understand which models or parameters are most significant from a modeler's perspective. It is recommended that one of these cases be used as a baseline for a parametric study. The effect of the chemistry database used for generating  $B'$  tables is known to be significant to the tables themselves, but following through until the end of the simulation to understand the impact on total recession and temperature would be valuable. Furthermore, a comparative study with three porous models i.e. instantaneous gas ejection from the surface, Darcy's Law, and unsteady-Darcy equations, would be highly interesting. Particularly if these tests are extended to multiple dimensions.

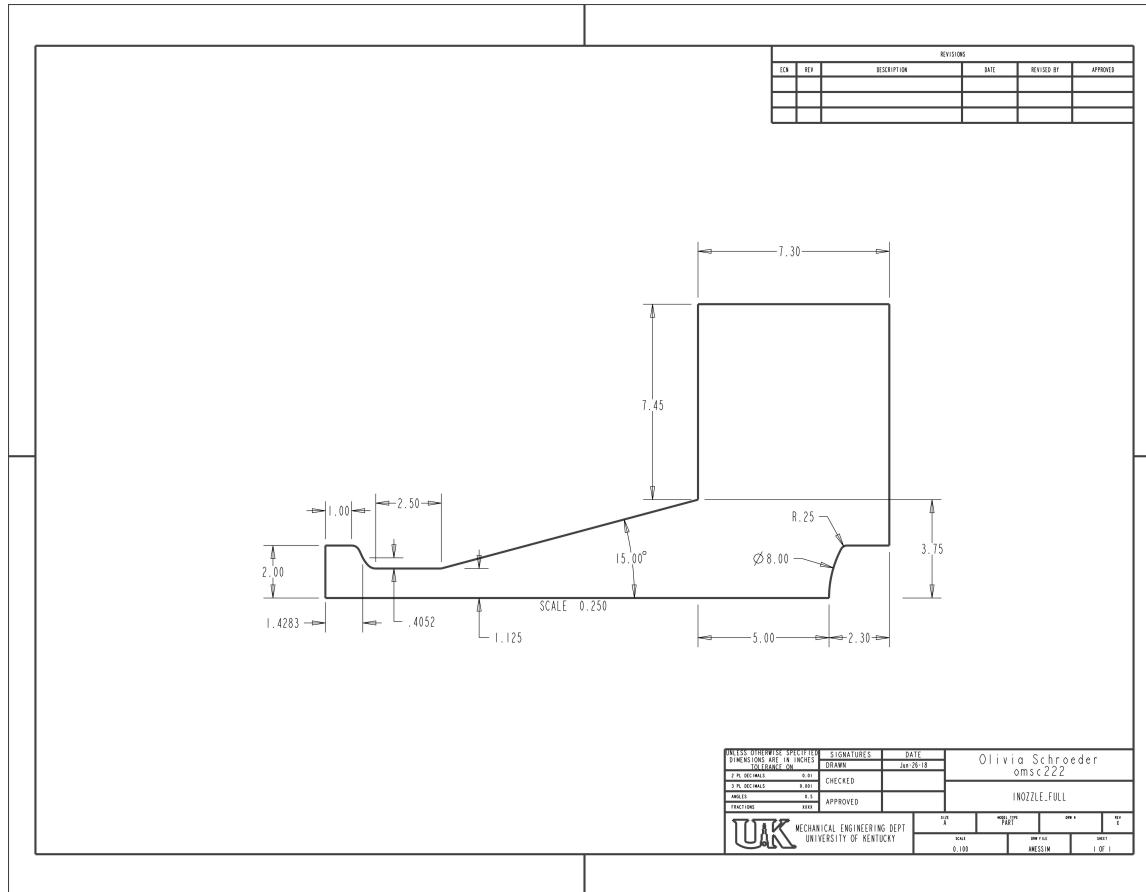
#### 6. **A porous model used in heritage codes is implemented in KATS**

A porous model based on Darcy's Law is implemented in the KATS framework. The implementation is verified and added to the testing suite described

in Chapter 3. A timing study are conducted to show gain in computational efficiency. A 1-D study is conducted comparing the unsteady Darcy's equations with Darcy's law. The apparent differences are discussed.

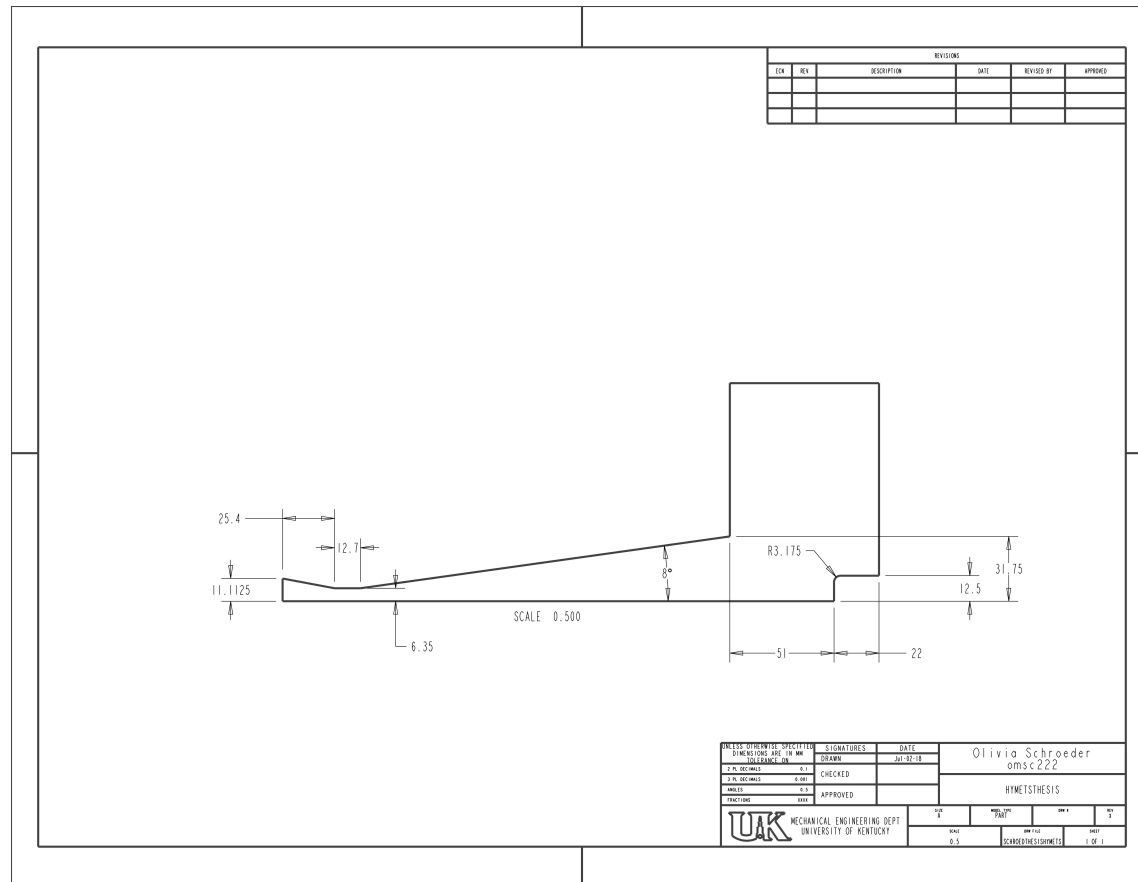
**Suggested Future Work:** More extensive testing is recommended for Darcy's Law porous model, particularly in what concerns decomposing materials. Furthermore, it is expected that the unsteady-Darcy porous model is most important in multi-dimensional problems, therefore it is also recommended that a parametric study on a 3-dimensional grid be conducted. Finally, the test exemplified in this work is at relatively low heating and pressure conditions. A more comprehensive study on the behavior of the gas as conditions become more extreme is also recommended.

# Appendix 1





# Appendix 2



## Bibliography

- [1] J. Stoll, Orion: Trial by fire, <https://archive.org/details/OrionTrialbyFire>.
- [2] The great images in nasa, <https://grin.hq.nasa.gov/> (2016).
- [3] Vostok 1's reentry capsule after landing, [www.esa.int/spaceinimages/Images/2011/03](http://www.esa.int/spaceinimages/Images/2011/03) (2007).
- [4] Smithsonian National Air and Space Museum, Mercury Friendship 7, <https://airandspace.si.edu/collection-objects/capsule-mercury-ma-6>.
- [5] N. A. R. Center, Hyperseed mac news, <https://reentry.arc.nasa.gov/>.
- [6] J. W. Lawson, M. M. Stackpoole, V. Shklover, Examination of scanning electron microscope and computed tomography images of pica (2011).
- [7] E. Stern, I. Nompelis, T. E. Schwartzentruber, G. V. Candler, Microscale simulations of porous tps materials: Ablating microstructures and micro-tomography, in: 53rd AIAA Aerospace Sciences Meeting, AIAA Paper 2015-1450, 2015. doi:10.2514/6.2015-1450.
- [8] J. A. Inman, B. F. Bathel, C. T. Johansen, P. M. Danehy, S. B. Jones, J. G. Gragg, S. C. Splinter, Nitric-oxide planar laser-induced fluorescence measurements in the hypersonic materials environmental test system, AIAA Journal 51 (10) (2013) 2365–2379. doi:10.2514/1.J052246.
- [9] M. J. Wright, M. Hughes, A. Calomino, M. D. Barnhardt, An overview of technology investments in the NASA entry systems modeling project, in: 53rd AIAA Aerospace Sciences Meeting, AIAA Paper 2015-1892, Kissimmee, Florida, 2015. doi:10.2514/6.2015-1892.
- [10] M. J. Wright, Aerothermodynamics, Hypersonic Educational Initiative, Reacting Flow Environments Branch, NASA Ames Research Center.
- [11] M. J. Wright, Thermal protection systems, Hypersonic Educational Initiative, Reacting Flow Environments Branch, NASA Ames Research Center.
- [12] R. D. Braun, Importance of simulation, Hypersonic Educational Initiative, Georgia Institute of Technology.

- [13] U. Duzel, Validation of gas/surface interaction modeling in plasmatron facility for in-flight experiment development, Master's thesis, von Karman Institute for Fluid Dynamics, Chaussée de Waterloo, 72 B - 1640 Rhode Saint Genèse - Belgium (June 2015).
- [14] R. Houtz, "orlon" acrylic fiber: Chemistry and properties, *Textile Research Journal* 20 (10) (1950) 786–801. doi:10.1177/004051755002001107.
- [15] H. J. Allen, The aerodynamic heating of atmosphere entry vehicles, Tech. rep., NASA, Buffalo, NY (June 25-26 1964).
- [16] R. D. Launius, D. R. Jenkins, *Coming Home: Reentry and Recovery from Space*, NASA Aeronautics Book Series, 2011.
- [17] T. Paone, A closer look at the friendship 7 spacecraft, Smithsonian National Air and Space Museum (February, 10 2017).
- [18] Mark 4 operational re-entry vehicle titan/atlas quarterly program progress report, Tech. Rep. Report 21-138.1, Avco Corporation, Operational Missiles Subdivision (May 10 1961).
- [19] T. Cichan, S. D. Norris, P. Marshall, Orion: EFT-1 flight test results and em-1/2 status, in: *AIAA SPACE 2014 Conference and Exposition*, AIAA Paper 2015-4415, 2015. doi:10.2514/6.2015-4414.
- [20] D. A. Kontinos, M. Stackpoole, Post-flight analysis of the stardust sample return capsule earth entry, in: *46th AIAA Aerospace Sciences Meeting and Exhibit*, AIAA Paper 2008-1197, Reno, Nevada, 2008. doi:10.2514/6.2008-1197.
- [21] B. K. Bessire, T. K. Minton, Decomposition of phenolic impregnated carbon ablator (pica) as a function of temperature and heating rate, *ACS Applied Materials & Interfaces* 9 (25) (2017) 21422–21437. doi:10.1021/acsami.7b03919.
- [22] A. Omidy, A. Martin, H. Weng, J. Grana, Modeling gasification of carbon fiber preform in oxygen rich environments, in: *47th AIAA Thermophysics Conference*, AIAA 2017-3686, Denver, CO, 2017. doi:10.2514/6.2017-3686.
- [23] F. Panerai, A. Martin, N. N. Mansour, S. A. Sepka, J. Lachaud, Flow-tube oxidation experiments on the carbon preform of a phenolic-impregnated carbon ablator, *Journal of Thermophysics and Heat Transfer* 28 (2) (2014) 181–190. doi:10.2514/1.T4265.

- [24] S. Poovathingal, T. E. Schwartzentruber, S. G. Srinivasan, A. C. T. van Duin, Large scale computational chemistry modeling of the oxidation of highly oriented pyrolytic graphite, *Journal of Physical Chemistry* 117 (2013) 2692–2703. doi:10.1021/jp3125999.
- [25] J. Lachaud, I. Cozmuta, N. N. Mansour, Multiscale approach to ablation modeling of phenolic impregnated carbon ablators, *Journal of Spacecraft and Rockets* 47 (6) (2010) 910–921. doi:10.2514/1.42681.
- [26] M. Miller-Oana, Oxidation behavior of carbon and ultra-high temperature ceramics, Ph.D. thesis, University of Arizona, Tucson, AZ (December 2016).
- [27] S. Poovathingal, T. E. Schwartzentruber, V. J. Murray, T. K. Minton, Molecular simulation of carbon ablation using beam experiments and resolved microstructure, *AIAA Journal* 54 (3) (2016) 999–1010. doi:10.2514/1.J054562.
- [28] R. S. C. Davuluri, H. Zhang, A. Martin, Numerical study of spallation phenomenon in an arc-jet environment, *Journal of Thermophysics and Heat Transfer* 30 (1) (2015) 32–41. doi:10.2514/1.T4586.
- [29] A. Martin, S. C. C. Bailey, F. Panerai, R. S. C. Davuluri, H. Zhang, A. R. Vazsonyi, Z. S. Lippay, N. N. Mansour, J. A. Inman, B. F. Bathel, S. C. Splinter, P. M. Danehy, Numerical and experimental analysis of spallation phenomena, *CEAS Space Journal* 8 (229). doi:10.1007/s12567-016-0118-4.
- [30] E. Bartlett, W. Nicolet, L. Anderson, R. Kendall, Further studies of the coupled chemically reacting boundary layer and charring ablator, part i, summary report, Tech. rep., NASA (June 1968).
- [31] C. B. Moyer, R. A. Rindal, An analysis of the coupled chemically reacting boundary layer and charring ablator. part ii-finite-difference solution for the in-depth response of charring materials considering surface chemical and energy balances, Tech. rep., NASA (1968).
- [32] Y.-K. Chen, F. S. Milos, Ablation and thermal response program for spacecraft heatshield analysis, *Journal of Spacecraft and Rockets* 36 (3) (1999) 475–483. doi:10.2514/2.3469.
- [33] A. J. Amar, N. D. Calvert, B. S. Kirk, Development and verification of the charring ablating thermal protection implicit system solver, in: 49th AIAA Aerospace

- Sciences Meeting including the New Horizons Forum and Aerospace Exposition, AIAA Paper 2011-144, Orlando, FL, 2011. doi:10.2514/6.2011-144.
- [34] A. J. Amar, A. B. Oliver, B. S. Kirk, G. Salazar, Overview of the charring ablator response (char) code, in: 46th AIAA Thermophysics Conference, AIAA Paper 2016-3385, Washington, D.C., 2016. doi:10.2514/6.2016-3385.
- [35] J. C. Schulz, E. Stern, S. Muppidi, G. Palmer, O. Schroeder, A. Martin, Development of a three-dimensional, unstructured material response design tool, in: 55th AIAA Aerospace Sciences Meeting, AIAA Paper 2017-0667, American Institute of Aeronautics and Astronautics, 2017. doi:10.2514/6.2017-0667.
- [36] H. Zhang, High temperature flow solver for aerothermodynamics problems, Ph.d. thesis, University of Kentucky, Lexington, KY (August 2015). doi:10.13140/RG.2.1.2415.1761.
- [37] H. Weng, A. Martin, Multidimensional modeling of pyrolysis gas transport inside charring ablative materials, *Journal of Thermophysics and Heat Transfer* 28 (4) (2014) 583–597. doi:10.2514/1.T4434.
- [38] R. Fu, H. Weng, J. F. Wenk, A. Martin, Thermomechanical coupling for charring ablaters, *Journal of Thermophysics and Heat Transfer* 32 (2) (2017) 369–379. doi:10.2514/1.T5194.
- [39] N. Nouri, A. Martin, Three dimensional radiative heat transfer model for the evaluation of the anisotropic effective conductivity of fibrous materials, *International Journal of Heat and Mass Transfer* 83 (2015) 629 – 635. doi:10.1016/j.ijheatmasstransfer.2014.12.041.
- [40] R. S. C. Davuluri, Modeling of spallation phenomenon in an arc-jet environment, Master’s thesis, University of Kentucky, Lexington, KY (2015).  
URL [https://uknowledge.uky.edu/me\\_etds/63/](https://uknowledge.uky.edu/me_etds/63/)
- [41] J. Lachaud, N. N. Mansour, Porous-material analysis toolbox based on OpenFOAM and applications, *Journal of Thermophysics and Heat Transfer* 28 (2) (2014) 191–202. doi:10.2514/1.T4262.
- [42] J. C. Ferguson, F. Panerai, J. Lachaud, A. Martin, S. C. C. Bailey, N. N. Mansour, Modeling the oxidation of low-density carbon fiber material based on microtomography, *Carbon* 96 (2016) 57–65. doi:10.1016/j.carbon.2015.08.113.

- [43] A. Borner, F. Panerai, N. N. Mansour, High temperature permeability of fibrous materials using direct simulation monte carlo, *International Journal of Heat and Mass Transfer* 106 (2017) 1318–1326. doi:10.1016/j.ijheatmasstransfer.2016.10.113.
- [44] H. Weng, A. Martin, Development of a universal solver and its application to ablation problems, in: 47th AIAA Thermophysics Conference, AIAA Paper 2017-3355, Denver, CO, 2017. doi:10.2514/6.2017-3355.
- [45] J. M. Cooper, O. M. Schroeder, H. Weng, A. Martin, Implementation and verification of a surface recession module in a finite volume ablation solver, in: 2018 Joint Thermophysics and Heat Transfer Conference, AIAA Paper 2018-3272, 2018. doi:10.2514/6.2018-3272.
- [46] H. Weng, S. C. Bailey, A. Martin, Numerical study of iso-q sample geometric effects on charring ablative materials, *International Journal of Heat and Mass Transfer* 80 (2015) 570 – 596. doi:10.1016/j.ijheatmasstransfer.2014.09.040.
- [47] H. Weng, A. Martin, Numerical investigation of thermal response using orthotropic charring ablative material, *Journal of Thermophysics and Heat Transfer* 29 (3) (2015) 429–438. doi:10.2514/1.T4576.
- [48] R. B. Bird, W. E. Stewart, E. N. Lightfoot, *Transport Phenomena*, Second Edition, Wiley, 2014.
- [49] V. S. Arpaci, *Conduction Heat Transfer*, Addison-Wesley, Reading, MA, 1966.
- [50] V. J. Beck, B. F. Blackwell, C. R. S. Clair, *Inverse Heat Conduction Problems*, Wiley-Interscience, New York, NY, 1985.
- [51] A. J. Amar, B. S. Kirk, A. B. Oliver, G. Salazar, J. C. Droba, Development and Verification of the CHarring Ablator Response (CHAR) Code, NASA Lyndon B. Johnson Space Center, Houston, Texas (February 2013).
- [52] A. Anna, I. D. Boyd, Numerical analysis of surface chemistry in high-enthalpy flows, *Journal of Thermophysics and Heat Transfer* 29 (4) (2015) 653–670. doi:10.2514/1.T4530.
- [53] J. L. Steger, R. Warming, Flux vector splitting for the inviscid gasdynamic equations with applications to finite difference methods, *Journal of Computational Physics* 40 (2) (1981) 263–293. doi:10.1016/0021-9991(81)90210-2.

- [54] C. Park, Nonequilibrium Hypersonic Aerothermodynamics, Wiley-Interscience, 1990, ISBN 978-0471510932.
- [55] W. G. Vincenti, C. H. Kruger, Introduction to physical gas dynamics, New York: Wiley, 1965.
- [56] R. C. Millikan, D. R. White, Systematics of vibrational relaxation, The Journal of Chemical Physics 39 (1963) 3209–3213. doi:10.1063/1.1734182.
- [57] F. G. Blottner, M. Johnson, M. Ellis, Chemically reacting viscous flow program for multi-component gas mixtures, Tech. Rep. SC-RR-70-754, Sandia Labs (January 1971). doi:10.2172/4658539.
- [58] C. Wilke, A viscosity equation for gas mixtures, The Journal of Chemical Physics 18 (4) (1950) 517–519. doi:10.1063/1.1747673.
- [59] R. N. Gupta, J. M. Yos, R. A. Thompson, K.-P. Lee, A review of reaction rates and thermodynamic and transport properties for an 11-species air model for chemical and thermal nonequilibrium calculations to 30000 K, Tech. Rep. 19900017748, NASA (1990).
- [60] M. J. Wright, G. V. Candler, D. Bose, Data-parallel line relaxation method for the navier- stokes equations, AIAA Journal 36 (9) (1998) 1603–1609. doi:10.2514/2.586.
- [61] T. Gokcen, J. Balboni, A. I. Alunni, Computational simulations of the 10-MW TP3 arc-jet facility flow, in: 45th AIAA Thermophysics Conference, AIAA Paper 2015-3103, 2015. doi:10.2514/6.2015-3103.
- [62] PTC, Creo parametric, <https://www.ptc.com/en/products/cad>, version 3.0 Student Edition.
- [63] Pointwise, <https://www.pointwise.com/>, version 17.1R4.
- [64] A. Viladegut, Ü. Düzel, O. Chazot, Diffusion effects on the determination of surface catalysis in inductively coupled plasma facility, Chemical Physics 485-486 (2017) 88 – 97. doi:10.1016/j.chemphys.2017.02.002.
- [65] U. Duzel, O. Schroeder, A. Martin, Computational prediction of NASA langley HYMETs arc jet flow with KATS, in: 2018 AIAA Aerospace Sciences Meeting, AIAA Paper 2018-1719, Kissimmee, FL, 2018. doi:10.2514/6.2018-1719.

- [66] D. G. Goodwin, H. K. Moffat, R. L. Speth, Cantera: An object-oriented software toolkit for chemical kinetics, thermodynamics, and transport processes, version 2.3.0 (2017). doi:10.5281/zenodo.170284.
- [67] H. K. Tran, C. E. Johnson, D. J. Rasky, F. C. L. Hui, M.-T. Hsu, T. Chen, Y. K. Chen, D. Paragas, L. Kobayashi, Phenolic impregnated carbon ablators (pica) as thermal protection systems for deep space missions, Tech. rep., NASA (1997).
- [68] J. B. Scoggins, T. E. Magin, Development of mutation++: Multicomponent thermodynamic and transport properties for ionized plasmas written in c++, in: 11th AIAA/ASME Joint Thermophysics and Heat Transfer Conference, AIAA Paper 2014-2966, Atlanta, GA, 2014. doi:10.2514/6.2014-2966.
- [69] F. Milos, Y.-K. Chen, Ablation predictions for carbonaceous materials using cea and jannaf-based species thermodynamics, in: 42nd AIAA Thermophysics Conference, AIAA Paper 2011-3123, Honolulu, Hawaii, 2011. doi:10.2514/6.2011-3123.
- [70] G. V. Candler, Nonequilibrium processes in hypervelocity flows: An analysis of carbon ablation models, in: 50th AIAA Aerospace Sciences Meeting including the New Horizons Forum and Aerospace Exposition, AIAA Paper 2012-0724, Nashville, TN, 2012. doi:10.2514/6.2012-724.
- [71] F. S. Milos, Y.-K. Chen, Ablation and thermal response property model validation for phenolic impregnated carbon ablator, *Journal of Spacecraft and Rockets* 47 (5). doi:10.2514/1.42949.
- [72] A. Martin, H. Zhang, K. A. Tagavi, An introduction to the derivation of surface balance equations without the excruciating pain, *International Journal of Heat and Mass Transfer* 115, Part A (2017) 992–999. doi:10.1016/j.ijheatmasstransfer.2017.07.078.
- [73] W. Kays, M. Crawford, B. Weigand, *Convective Heat and Mass Transfer*, 4th Edition, McGraw-Hill, 2005.
- [74] J. Lachaud, T. E. Magin, I. Cozmuta, N. N. Mansour, A short review of ablative-material response models and simulation tools, in: 7th Aerothermodynamics Symposium, Brugge, Belgium, 2011.
- [75] P. Forchheimer, Wasserbewegung durch boden, *Zeitschrift des Vereines deutscher Ingenieure* 45 (50) (1901) 1781–1788.



- [76] E. W. Weisstein, Courant-friedrichs-lewy condition, MathWorld.
- [77] S. V. Patankar, Numerical Heat Transfer and Fluid Flow, Taylor and Francis, 1980.
- [78] M.-S. Liou, A sequel to AUSM, part II: AUSM+ -up for all speeds, Journal of Computational Physics 214 (1) (2006) 137 – 170. doi:10.1016/j.jcp.2005.09.020.
- [79] T. Gökçen, Effects of test box pressure on arc-jet flowfields and implications for testing, in: Joint Thermophysics and Heat Transfer Conference, AIAA Paper 2018-3771, Atlanta, GA, 2018. doi:10.2514/6.2018-3771.

## Vita

### Olivia Schroeder

<https://orcid.org/0000-0003-0487-2992>

#### Education

- University of Kentucky, Lexington, KY  
Bachelor of Science in Mechanical Engineering

#### Professional positions held

- Graduate Research Assistant for Dr. Alexandre Martin, UK Dept. of Mechanical Engineering, Gas Surface Interactions Lab, June 2015 - Present
- Aerothermodynamics and Material Response Engineer, NASA ARC - AMA Inc. - TSM, June - August 2017
- Aerothermodynamics and Material Response Engineer, NASA ARC - AMA Inc. - TSM, June - August 2016
- High End Fuser Technology Engineering Intern, Lexmark International, Inc., May - September 2015

#### Scholastic and professional honors

- College of Engineering Dean's Award for Outstanding Master's Student, *University of Kentucky*, 2017
- 2016 NASA Kentucky Space Grant Research Project (graduate fellowship)
- University Scholars Program
- 2015 NASA Kentucky Space Grant Undergraduate Fellowship
- Dean's List from Spring-2014 to Fall-2017

#### Publications

- F. Panerai, J. D. White, T. J. Cochell, O. M. Schroeder, N. N. Mansour, M. J. Wright, and A. Martin. Experimental measurements of the permeability of fibrous carbon at high-temperature. *International Journal of Heat and Mass Transfer*, 101(10.1016):267-273, October 2016.  
<http://dx.doi.org/10.1016/j.ijheatmasstransfer.2016.05.016>.

- J. M. Cooper, O. M. Schroeder, H. Weng, A. Martin, Implementation and verification of a surface recession module in a finite volume ablation solver, in: 2018 Joint Thermophysics and Heat Transfer Conference, AIAA Paper 2018-3272, 2018. doi:10.2514/6.2018-3272.
- U. Duzel, O. Schroeder, A. Martin, Computational prediction of NASA Langley HYMETs arc jet flow with KATS, in: 2018 AIAA Aerospace Sciences Meeting, AIAA Paper 2018-1719, Kissimmee, FL, 2018. doi:10.2514/6.2018-1719.
- Schulz, J. C., Stern, E., Muppidi, S., Palmer, G., Schroeder, O., Martin, A., “Development of a three-dimensional, unstructured material response design tool”, 55th AIAA Aerospace Sciences Meeting, AIAA SciTech Forum, (AIAA 2017-0667)  
<http://dx.doi.org/10.2514/6.2017-0667>
- Schroeder, O., Cooper, J. M., Weng, H., Martin, A., “Validation of the KATS Material Response Solver with Arc-Jet Experiments,” 42nd Dayton-Cincinnati Aerospace Sciences Symposium, No.42DCASS-083, Dayton, OH, March 2017
- Cooper, J.M., O. M., Schroeder, Weng, H., and Martin, A., “Multi-Dimensional Surface Chemistry Comparison of Iso-Q Arc-Jet Cases,” 36th Dayton-Cincinnati Aerospace Sciences Symposium, No. 42DCASS-055, Dayton, OH, March 2017.